Martian near-surface materials in shergottite meteorites: Searching for evidence from Tissint shock-melt pockets

by

Cody Robert Kuchka

A thesis submitted in partial fulfillment of the requirements for the degree of

Master of Science

Department of Earth and Atmospheric Sciences

Abstract

Three thin sections of the Tissint Martian meteorite were examined by an array of *in situ* techniques in order to assess the possibility that a geochemical signature characteristic of the Martian near-surface has been preserved within the meteorite. Tissint is a recent basaltic Martian fall that contains an abundance of shock-generated melt glass that formed by a variety of mechanisms including grain-boundary frictional melting, concentration of shockwaves along boundaries of minerals with contrasting shock-impedance, and void collapse. Tissint is special amongst the suite of Martian meteorites in that it is only the fifth witnessed Martian fall, and its short residence time in a hot desert precluded significant terrestrial weathering.

Shock melt pockets form *in situ* by local melting of igneous phases. Major element compositions and rare earth element patterns do not suggest a contribution from Martian soil or minerals derived from the Martian surface (e.g. jarosite) to the shock melt. Shock-metamorphic sulfides (iron-sulfide spherules within shock melt pockets) exhibit elevated Fe/S ratios compared to groundmass sulfides that were not incorporated into shock melt pockets or veins. Additionally, Raman spectra collected for shock-metamorphic sulfides exhibit Raman peaks characteristic of hematite. These Raman peaks are not present for groundmass sulfides; sulfides were altered (oxidized) as a consequence of the shock event. Thermal modelling results show that cooling times for individual regions of shock melt are controlled by their size, geometry, proximity to other regions of shock melt, and the presence or absence of vesicles.

Volatile abundances determined by SIMS revealed that H_2O and Cl concentrations are correlated in shock melt glass. Water, chlorine, and fluorine concentrations are not correlated with phosphorus; water in Tissint shock melt glass cannot be attributed to igneous apatite. Hydrogen isotopes demonstrate that the water within Tissint shock melt glass has experienced mixing

between two reservoirs: the Martian mantle and the Martian near-surface. For shock melt glass containing vesicles, the shock melt may partially devolatilize to the vesicle before quenching was complete.

A geochemical signature derived from the Martian near-surface is preserved in Tissint shock melt pockets, observed primarily in H_2O and Cl concentrations and hydrogen isotopes. This signature is very minor and is only detectable by sensitive techniques. Shock melt pockets with the greatest potential to preserve such a signature are isolated from other regions of shock melt, vesicle-free, and glassy.

Acknowledgments

First, I would like to extend my sincerest thanks to my supervisors, Dr. Christopher Herd and Dr. Erin Walton. Thank you for all of your invaluable feedback, guidance, and patience throughout my thesis. Under your tutelage, I have become a much better researcher and writer, and for that I will always be grateful.

I would like to thank Andrew Locock (EPMA lab), Andy DuFrane (ICP-MS lab), and Nathan Gerein (SEM lab), of the Department of Earth and Atmospheric Sciences, analytical assistance. I also thank Yunbin Guan (Center for Microanalysis, Caltech) for his help getting me set up on the ion probe, and to Yang Chen (Division of Geological and Planetary Sciences, Caltech) for sticking with me for long hours in the SIMS lab. I'd like to extend a special thank you to Yang Liu, who provided funding for two days of analysis time on the ion probe, which was instrumental to my project. I also extend thanks to my committee chair, Dr. Sarah Gleeson, and my external examiner, Dr. Long Li.

I am thankful to my parents, who have supported me throughout my education and have always done everything they could do to help me be successful. Special thanks to my sister Bailey, who continues to push me forwards. Sibling rivalry lives still.

Finally, I would like to extend a warm thank you to Jenna Grant and Steve Eperjesy for all of their support.

Table of contents

List of tables

List of figures

1. Introduction

1.1 The Tissint meteorite

Tissint is a Martian meteorite that fell in the Moroccan desert on July 18th, 2011 (Irving et al., 2012; Chennaoui Aoudjehane et al., 2012). Tissint represents one of over 100 separate Martian meteorites recovered to date, and is only the 5th Martian fall (a meteorite that was observed falling to the Earth), seen as a bright streak across the sky at about 2 a.m. local time. The first pieces of the meteorite were recovered in October 2011, ~64 km outside of the town of Tissint. To date, a total of over 17 kg have been recovered (Irving et al., 2012; Barrat et al., 2014). A fresh, black fusion crust enveloping a grey olivine-phyric basaltic texture characterizes the stone. Pods of black glassy enclaves visible on cut surfaces are pervasive in the meteorite, observed as veins and pockets on the scale of 0.1 mm to several mm. The presence of black glass is typical of meteorites that have been subjected to transient high-pressure conditions, a consequence of shock-metamorphism that is likely linked to hypervelocity impact events that ejected material from meteorite parent bodies into space (Walton et al., 2011).

The purpose of this thesis was to perform an in-depth study of the Tissint meteorite to determine if it is possible that a near-surface component is preserved within shock melt glass. The subject of surface components in shergottites is topical in planetary science, and the results of this thesis will improve the current understanding of the effects of shock-metamorphism in shergottites, mechanisms for implanting externally-sourced (secondary) materials into meteorites, chemical heterogeneity of shock-generated melt glass, and how Martian surface-derived materials may affect the chemistry of shergottite meteorites.

1.2 A Martian origin for Tissint

Analyses of the shock-produced glass in Tissint reveals a relative noble gas abundance identical to that of the Martian atmosphere, measured *in situ* by *Viking* in 1976 (Chennaoui Aoudjehane et al., 2012), in a similar way the SNC meteorites were recognized as being derived from Mars (Treiman et al., 2000). The atmosphere of Mars is thought to have a unique composition in our Solar System that has not significantly changed over geologic time (Treiman et al., 2000).

Similar to Earth, oxygen isotopes in Martian rocks exhibit a mass-dependent fractionation trend that define the Martian Fractionation Line (MFL), analogous to the Terrestrial Fractionation Line (TFL), but offset ($\Delta^{17}O$) from TFL by +0.321‰ (Franchi et al., 1999). Evidence from three-oxygen isotopes reveals that Tissint exhibits an offset from TFL characteristic of Martian rocks ($\Delta^{17}O$ = 0.301‰, Chennaoui Aoudjehane et al., 2012). Tissint is classified as a depleted picritic olivine-phyric shergottite, based on bulk trace element composition (especially REEs; Irving et al. 2012) and texture. Its texture consists of olivine phenocrysts set in a groundmass of pyroxene, plagioclase, accessory oxides and phosphate minerals. The crystallization age of Tissint is 574 ± 20 Ma (Brennecka et al., 2014).

1.3 Shock metamorphism in meteorites

Impact events are common in the solar system, as meteoroids and asteroids collide with each other and with planetary bodies at velocities on the order of km/s (Bischoff and Stoffler, 1992; Sharp and DeCarli, 1996). Via these hypervelocity impacts, materials are ejected from their parent bodies into space, allowing for the exchange of materials from one planetary body to another (Treiman et al., 2000; Sharp and DeCarli, 2006). This method is the most viable mechanism for delivering Martian meteorites to Earth is ejection via asteroid impact on Mars: hypervelocity

impact events eject material from the surface at speeds exceeding the Martian escape velocity of 5 km/s (Melosh, 1985; Treiman et al., 2000; Fritz et al., 2005). Subsequently, these meteoroids enter into an Earth-crossing trajectory and fall to Earth as meteorites. It follows, therefore, that all Martian meteorites have experienced some degree of shock metamorphism (Nyquist et al., 2001; Fritz et al., 2005; Sharp and DeCarli, 2006). During this impact event, the shockwave will propagate through the rock. As rocks are naturally inhomogeneous media, propagation of this shockwave will be affected by the size, geometry, and density of individual mineral grains. Shock is concentrated into pre-existing voids and along boundaries of minerals with contrasting shock impedances, defined as shock wave velocity × mineral density (Stöffler et al., 1991). Shock-melt may be generated by a number of mechanisms including void collapse and grain boundary friction-induced melting, a phenomenon analogous to the formation of pseudotachylites at terrestrial impact structures (Sharp and DeCarli, 2006). Energy released during void collapse and grain boundary friction generates local "hot-spots" of extreme pressure and temperature that raises local temperatures above the solidus, generating a shock-melt pocket or shock vein. Heating to extreme temperatures (and subsequent melting) occurs nearly instantaneously (Stöffler et al., 1991; Sharp and DeCarli, 2006). These hot-spots are then cooled on the order of milliseconds to seconds (or, in cases with very large volumes of melt, minutes) as heat is lost by conduction to the colder country rock (Sharp and DeCarli, 2006; Walton and Herd, 2007; Shaw and Walton, 2013). For an in-depth review of how shockwaves interact with media from a geologic perspective, the reader is referred to Sharp and DeCarli (2006).

It is well understood that shock metamorphism is a viable mechanism for implanting gases into meteorites (e.g., Treiman et al., 2000), and it has been demonstrated that the quenched or quench-crystallized shock-melt glass in SNC meteorites is the specific host of the Martian

atmosphere component (Walton et al., 2007). While on Mars, Martian atmosphere was extant within pre-existing cracks and fractures in the rocks prior to the impact event that ejected them into space. Upon impact, the propagating shock wave caused these voids to collapse and generated pockets of melt that subsequently quenched, trapping Martian atmosphere into the meteorite. The possibility that Martian near-surface components may also be incorporated into meteorites is currently debated. A possible mechanism for incorporating these materials is similar to that for gas implantation: regolith, secondary alteration minerals, or another near-surface component is deposited within pre-existing voids in a rock. An impact event causes a shock wave to propagate through that rock. Shock causes void collapse and melting, and quenching traps this material in the meteorite. If any Martian near-surface materials are extant within these meteorites, they will likely be associated with shock-generated melt glass. Given the pristine nature of samples, Tissint is currently the best candidate to search for these near-surface components.

1.4 A fresh look at Mars

Tissint is the first Martian meteorite observed to fall since Zagami, which fell in Nigeria in 1962 (Irving et al., 2012). Owing to Tissint's short residence time (approximately three months) in a hot desert, any secondary weathering products present in the meteorite are likely Martian, not terrestrial. Given the near-pristine condition of recovered stones, Tissint provides a unique opportunity to study a fresh piece of Mars, and to examine subtle geochemical signatures characteristic of Martian secondary processes that would otherwise be modified, overprinted, or erased by terrestrial aqueous alteration during an extended residence on Earth.

When examining extraterrestrial materials, minimizing terrestrial contamination is important. Even with favorable fall and collection conditions, including a short pre-collection

residence in a hot desert (several months to a few years), meteorites may be susceptible to significant chemical alteration by terrestrial processes. It has been demonstrated that the chemical compositions of meteorites may be significantly altered in terrestrial deserts in a relatively short time, for example by formation of dewdrops that deposit material into fractures within the rock (Crozaz and Wadhwa, 2001; Crozaz et al., 2003). Such is the case for the Tatahouine meteorite: for two samples of the same meteorite collected from the Tunisian desert 63 years apart, the rock with the longer terrestrial residence time exhibited significant secondary weathering (Barrat et al., 1999). It is worth noting that 63 years is much longer than the residence time for Tissint samples that experienced residence times on the order of months rather than decades. Although meteorites may be weathered to a significant degree in a hot desert environment in a short period of time, weathering in Tissint is estimated to be minimal. The sections examined here were sampled from the interior of a large, fusion crust-enveloped stone, rather than sampled from rock chips, which may be more susceptible to terrestrial alteration, as cautioned by Barrat et al. (2014).

1.5 Recent studies of shergottite glass

While there have been numerous studies investigating the possibility that a Martian near-surface component may be trapped in shergottites, few studies have produced evidence for the presence of such components. Walton et al. (2010) investigated Elephant Moraine (EETA) 79001, a meteorite petrologically similar to Tissint. These authors investigated major and minor elements of Lithology C of EETA79001 using electron microprobe and LA-ICP-MS techniques. Lithology C is shock-generated melt glass chemically similar to Tissint glass. This study demonstrated that the variation in distribution of minor elements in glass when compared to the bulk rock, particularly distributions of sulfur, which has been hypothesized as being partially sourced from a

regolith component, may be explained by melting of minor igneous phases within the rock such as sulfides. The authors concluded that there is no Martian regolith component in EETA79001 (Walton et al., 2010).

Several recent studies targeting shock-generated melt glass in Tissint have yielded contradictory results. A study published by Chennaoui Aoudjehane et al. (2012) characterized Tissint's geochemistry: their results provided evidence that there is a surface-derived component present within the matrix and shock-generated melt features within the meteorite, sourced from *in situ* weathering while still on Mars. While the bulk composition of Tissint is similar to other depleted shergottites (particularly EETA79001), it is relatively enriched in sulfur and fluorine. Analysis of trace elements demonstrated that bulk Tissint has a rare earth element (REE) trend that, comparable to other depleted shergottites, is depleted in light rare earth elements (LREE) (Figure 1). In contrast, shock melt glass analyses yield a relatively flat pattern that is enriched in LREE with a positive cerium anomaly that may be explained by oxidation to Ce^{4+} during weathering in an oxidizing environment in the near-surface of Mars (Figure 1). Chennaoui Aoudjehane et al. (2012) proposed a scenario in which the Tissint host rock was emplaced in a near-surface environment, elements leached within the Martian near-surface were delivered to the rock by fluids, and near-surface-derived weathering materials (particularly phosphates, carriers for REE) were deposited into cracks and fractures. During the impact event that ejected the rock into space, there was preferential melting along fissures and voids, where these weathering products were concentrated. These hot-spots subsequently quenched, locking a near-surface component into the rock to be delivered to Earth in the meteorite.

Following the reporting of a Martian surface component in Tissint, several studies began to search for regolith or near-surface material in shergottites with contradictory results. Barrat et

al. (2014), using similar samples and methods, concluded that there are no surface-derived components in shergottites, in direct contrast to Chennaoui Aoudjehane et al. (2012). They also characterized the bulk Tissint and melt glass for major, minor, and trace elements, and found no LREE enrichment or positive cerium anomaly (Figure 1). Similar investigation of other shergottites, Dar al Gani (DaG) 670 and EETA 79001, provided no evidence for a surface-derived component (Barrat et al., 2014). To explain their contradictory findings, Barrat et al. (2014) suggested that the Tissint samples studied by Chennaoui Aoudjehane et al. (2012) may have experienced minor terrestrial weathering and thus the glass has been contaminated by terrestrial material.

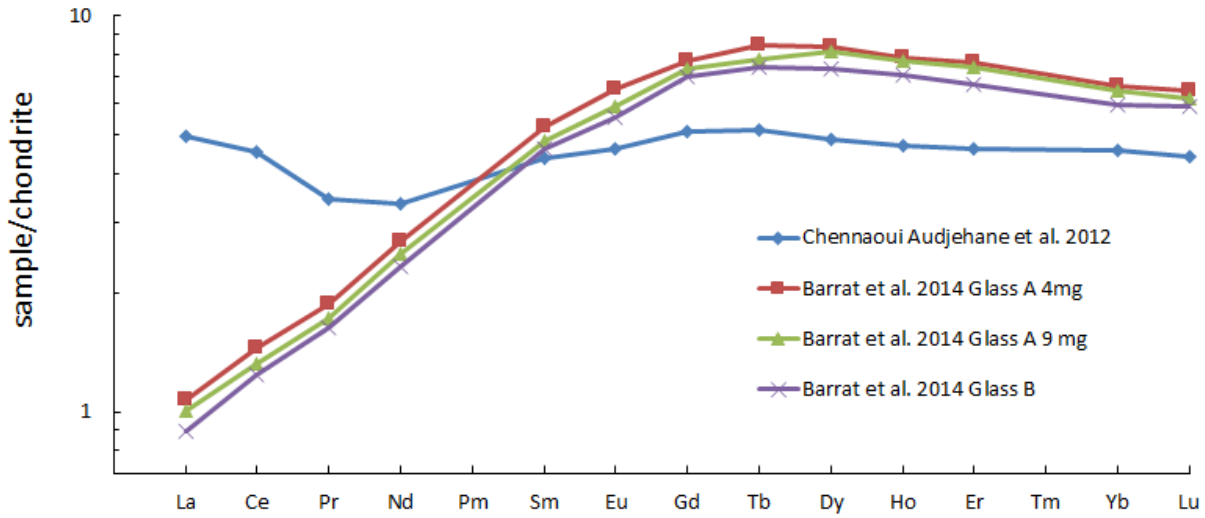

Figure 1: REE patterns for Tissint glass. Chennaoui Aoudjehane et al. (2012) observed that Tissint glass exhibits a relative enrichment in LREE elements, contrary to the REE pattern for bulk Tissint, which is depleted in LREE, similar to other depleted shergottites. Barrat et al. (2014) analyzed trace elements in two samples of Tissint glass, and observed no enrichment in LREE.

A possible explanation for disparity between studies may be due to a high degree of heterogeneity within the meteorite. Shergottites are heterogeneous by nature; the composition for a population of shock-melt glasses may be vastly heterogeneous even within the same meteorite. Some mechanisms of shock melt generation are more likely than others to preserve a geochemical

signature of surface-derived materials. For example, a melt pocket that formed by void collapse might capture material that was deposited within the void, such as Martian secondary alteration products. In contrast, no such signature would be expected within a shock melt that formed from friction-induced melting along the boundaries of igneous phases, distal to any open cracks or fractures containing surface-derived components. It is difficult to determine the mechanisms responsible for generating any individual shock melt feature. As such, it is difficult to identify *a priori* which shock melt features may or may not exhibit a geochemical signature characteristic of a Martian near-surface environment.

It is possible that alteration products are heterogeneously trapped within the meteorite, and this heterogeneity is responsible for the contradictory observations made by Chennaoui Aoudjehane et al. (2012) and Barrat et al. (2014). Alternatively, local-scale variations in shock melt composition resulting from variations in the conditions of formation may be the cause. In this study, the volatile contents of Tissint shock melt pockets were examined in order to explore these variables and shed light on the preservation potential for a geochemical signature characteristic of the Martian near-surface.

Tissint contains many high-pressure phases including as maskelynite (shock-vitrified plagioclase ($(Na,Ca)Al_{1-2}Si_{2-3}O_8$), ringwoodite ($\gamma$-$Mg_2SiO_4$), and stishovite (tetragonal SiO_2), as well as ahrensite (γ-Fe_2SiO_4) and tissintite ($(Ca,Na,\square)AlSi_2O_6$), both of which were discovered in this meteorite (Ma et al., 2014, 2015). Maskelynite is shock-amorphized plagioclase which retains igneous grain boundaries and zoning, and exhibits no evidence of melting, such as flow banding, schlieren, or vesiculation. Maskelynite forms by diaplectic, solid-state transformation from feldspar during shock compression, or by melting and quenching at high pressure (Chen et al., 2000; Fritz et al., 2005). Maskelynite is common in highly-shocked meteorites, and its occurrence

has been used to classify the shock stage of chondrite meteorites as stage S5 "strongly shocked," experiencing a peak shock pressure of 45-55 GPa, calibrated from shock recovery experiments (Stöffler et al., 1991). Ahrensite is the Fe-analogue of ringwoodite and a polymorph of fayalite with a cubic spinel structure. Tissintite is a Ca-Al pyroxene, analogous to a pyroxene of plagioclase composition with abundant structural vacancies. This study seeks to find and characterize high-pressure polymorphs in Tissint shock-melt pockets and veins, in order to gain insights into their pressure-temperature-time variability, and determine the role of such variability in the preservation of near-surface alteration products.

2. Materials and Methods

2.1 Tissint thin sections

Three thin sections of Tissint from the University of Alberta Meteorite Collection were examined for this thesis: MET11640/2-2-1/TEP, MET11640/2-3-2/TEP and MET11640/2-3-4/TEP. All the sections were cut from sample MET11640, a 58.2 g stone which was one of the first samples to be recovered in October 2011. The stone is characterized by a thin, glossy black fusion crust with no obvious weathering on its surface. A low-speed saw was used to cut the stone into smaller portions; all cutting was done dry, without the use of solvents or lubricants. From these subsamples, polished thin sections were prepared by the University of Alberta Thin Section Laboratory.

Shock melt is widespread in Tissint: shock veins permeate much of the rock and are typically encountered along grain boundaries. Shock melt pockets vary in size, morphology, and crystallinity: while some melt pockets are glassy, others are primarily crystalline. Oxide crystals and spherules of iron sulfide are also common within shock melt pockets and veins in varying

abundance (Figure 2). The distribution of shock-melted material in Tissint is extremely heterogeneous (Figure 3). In transmitted light, shock melt features appear as pods or veins that vary in color from a deep yellowish brown to opaque black. While opaque shock-melt may be difficult to discern from other opaque phases such as sulfides and oxides in transmitted light, the distinction is simple in reflected light: glass pods and veins have a similar reflectance to pyroxene or olivine, as opposed to the relatively high reflectance of the oxides and sulfides present (Figure 2).

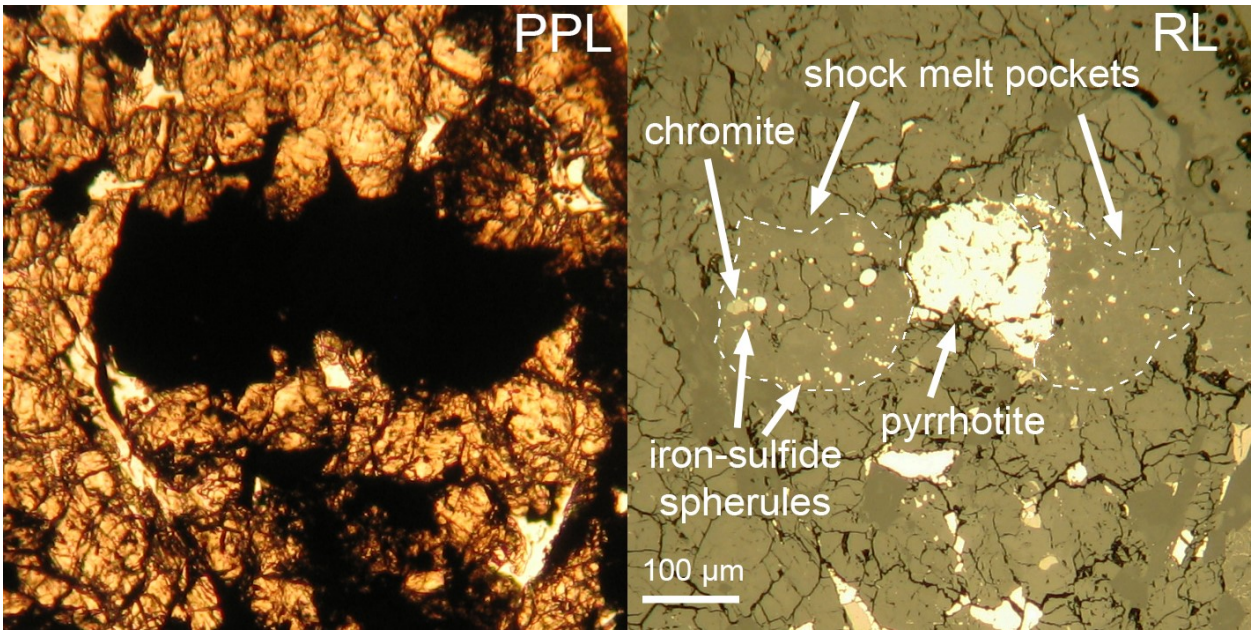

Figure 2. Plane-polarized light (PPL) and reflected light (RL) images of an opaque region in thin section MET11640/2-3-4/TEP. In PPL (left), maskelynite is colorless, pyroxene is brown, and oxides, sulfides, and the shock melt pocket are opaque; distinguishing shock melt features from opaque minerals is difficult. In RL (right), the shock melt pocket is readily delineated from opaque minerals.

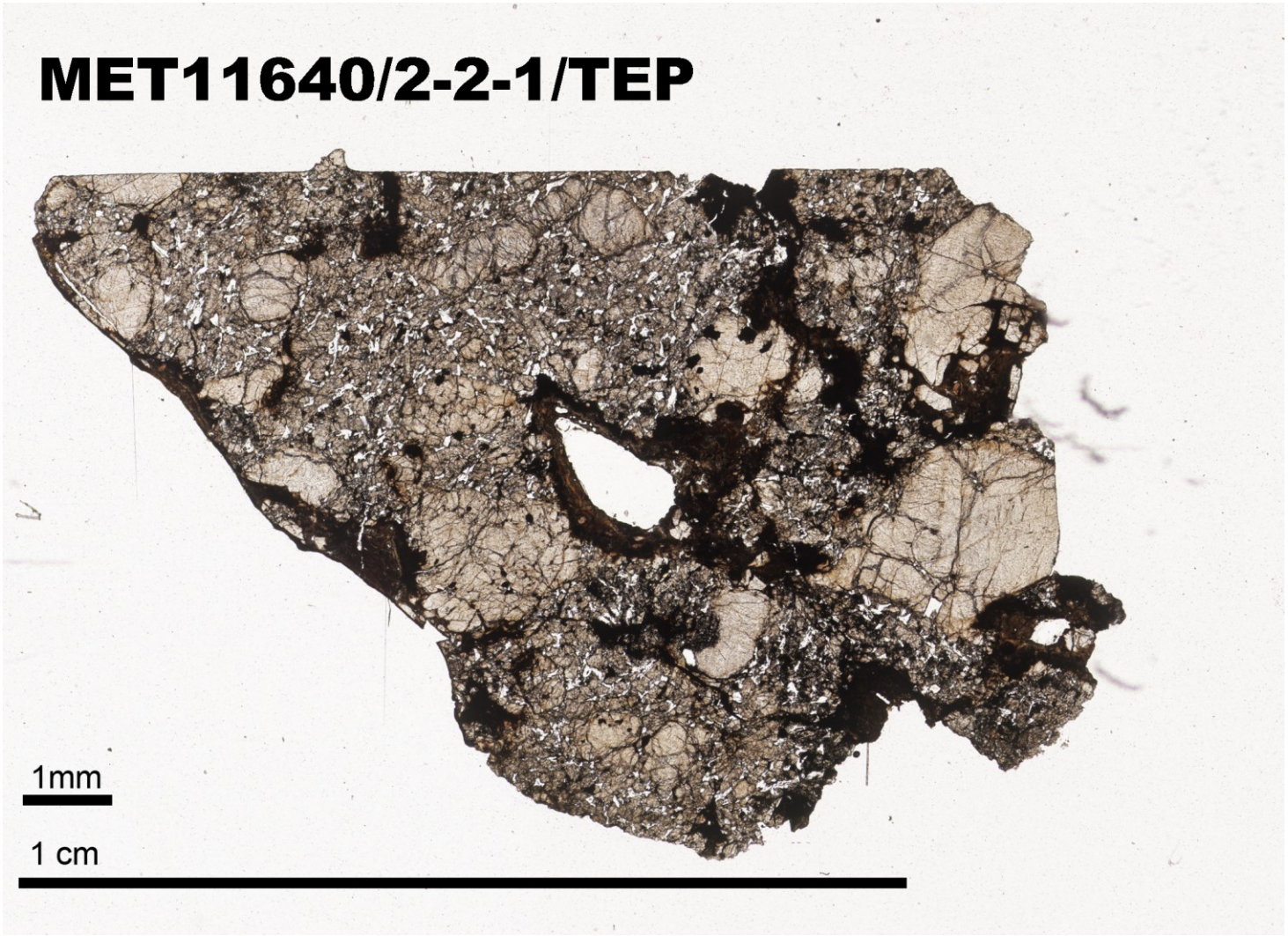

Figure 3a: Photomicrograph of thin section MET11640/2-2-1/TEP. The groundmass consists mostly of pyroxene (brown) and maskelynite (colorless). Black regions internal to the section are sulfides, oxides, and shock melt. In transmitted light, shock-melted areas are seen as opaque black to isotropic semi-opaque dark brown pockets and veins. The hole in the center of the section is a vesicle within a shock melt pocket.

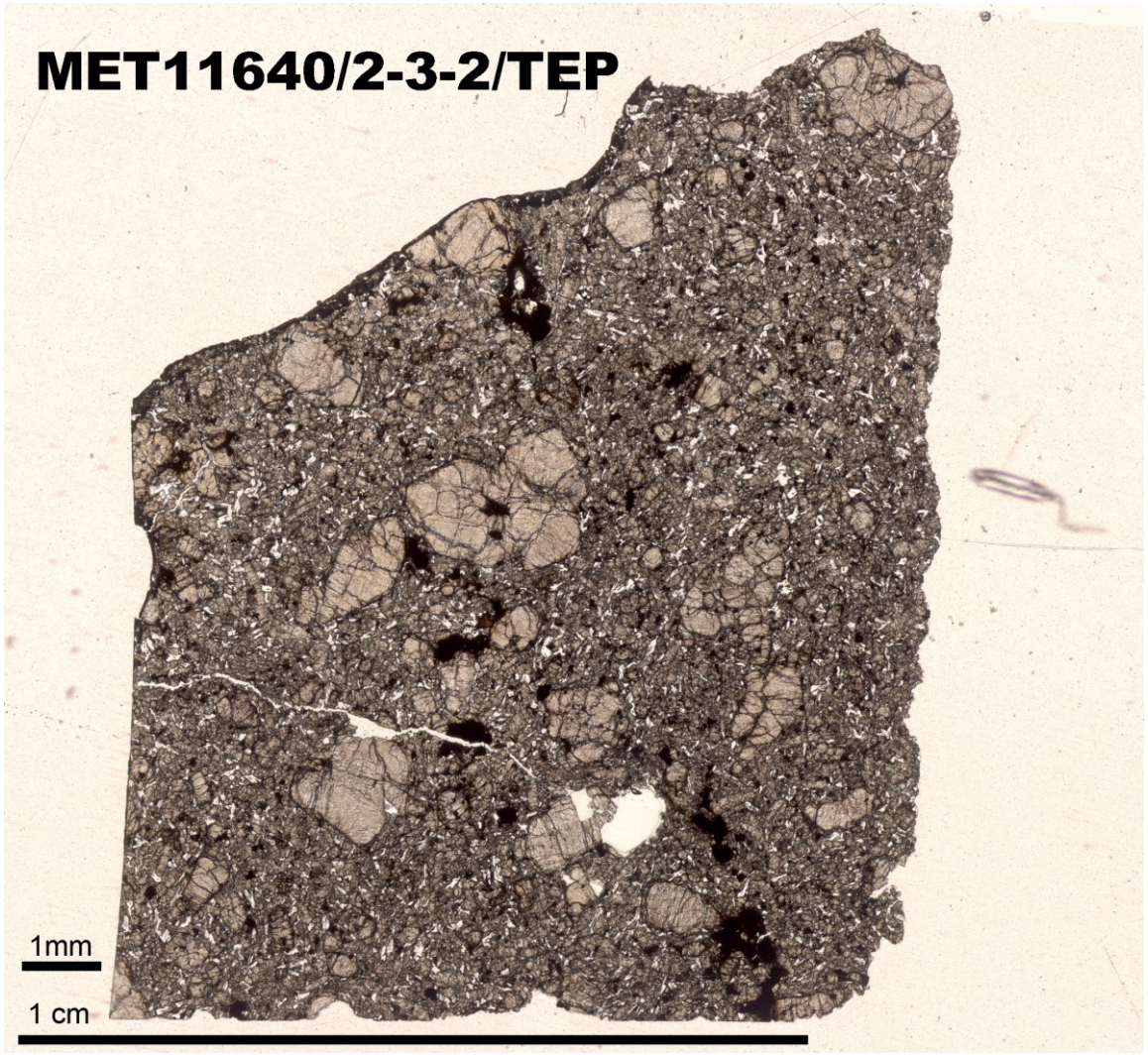

Figure 3b: Photomicrograph of thin section MET11640/2-3-2/TEP. Euhedral olivine macrocrysts are visible in this sample.

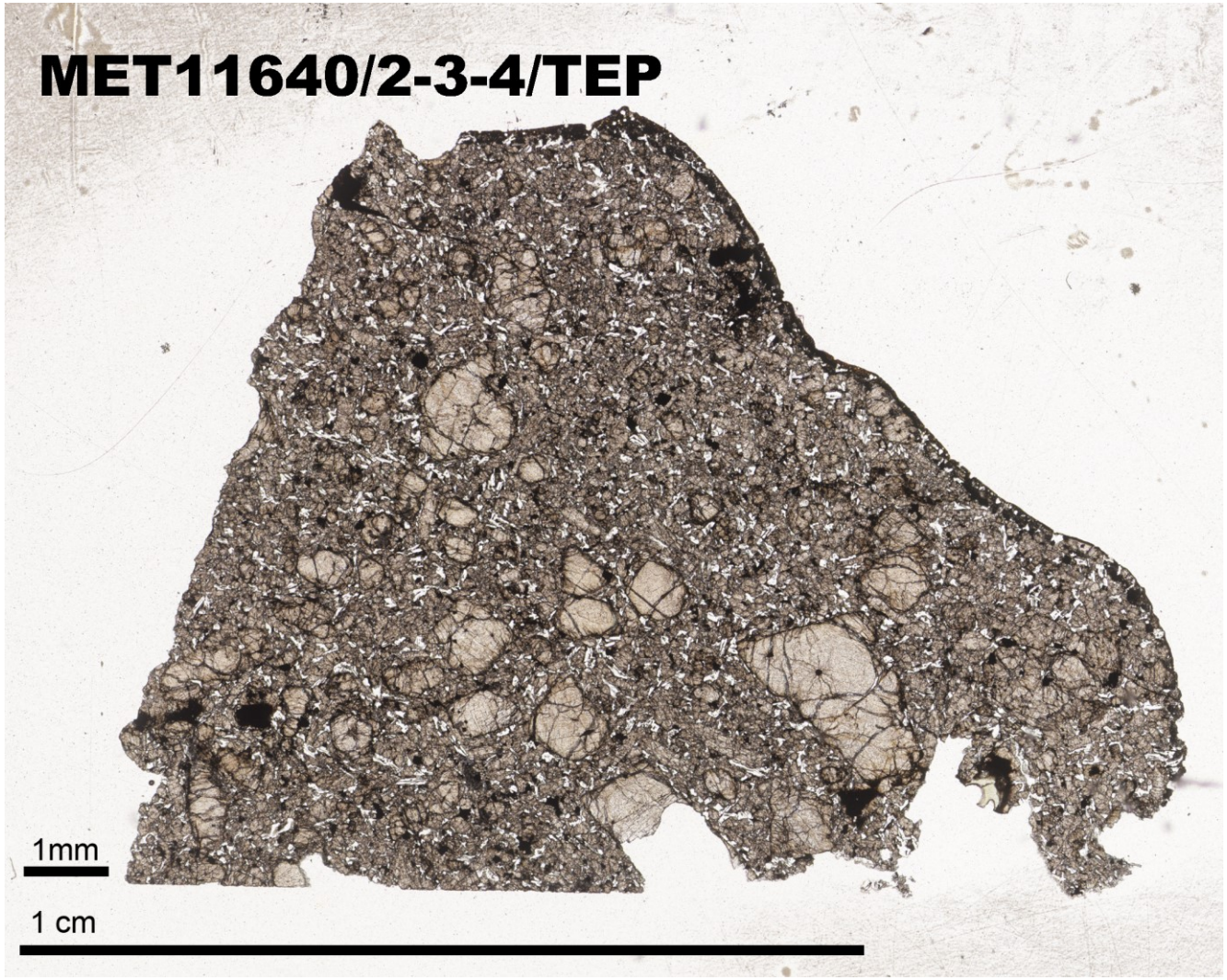

Figure 3c: Photomicrograph of thin section MET11640/2-3-4/TEP. The distribution of shock melt pockets and veins in Tissint is heterogeneous: compare the relative abundance of shock melt in each sample.

2.2 Scanning electron microscopy

Sections were mapped in transmitted and reflected light to identify areas of interest, namely opaque to semi-opaque shock melts pockets and veins. Sections were then mapped using a Zeiss Evo MA LaB_6 scanning electron microscope (SEM) equipped with an energy-dispersive X-ray spectrometer (EDS). SEM analysis was performed at the University of Alberta, in the Scanning Electron Microscope Laboratory of the Department of Earth and Atmospheric Sciences. Shock melt pockets and veins were characterized for texture, size, morphology, distribution, and mineralogy by back-scattered electron (BSE) imagery and EDS.

2.3 Raman spectroscopy

Analyses by Raman spectroscopy were performed using a Bruker SENTERRA Raman spectrometer at MacEwan University (Department of Physical Sciences). Prior to Raman analysis, sections were lightly polished to remove any carbon coating which had been applied for other microbeam methods. The excitation laser (532 nm line of an Ar+ laser) was focused through a 50×1000 μm slit aperture using the 100× objective lens. The spot size for all analyses was ~1 μm. For silicates, analyses were acquired by 3 iterations of 2 s each with a laser power of 10 mW. For oxides and sulfides, Raman spectra were collected for 3 iterations of 2s each at a laser power of 2 mW. A lower-power laser was used for analyzing opaque minerals to minimize risk of damaging the sulfide phases in the sample. Raman spectra were processed using commercial spectroscopy software. To identify phases, Raman spectra and peak positions were compared to literature data and the RRUFF Project database of Raman spectra (Lafuente et al., 2015).

2.4 Electron probe microanalysis

Major and minor element chemistries were determined by a JEOL 8900R electron probe microanalyzer (EMPA) equipped with an energy-dispersive spectrometer (EDS) and five wavelength-dispersive spectrometers (WDS). EPMA analysis was performed at the Electron Microprobe Laboratory (Department of Earth and Atmospheric Sciences) at the University of Alberta. Shock melt pockets are notoriously heterogeneous, and determining the "true" composition for a volume of glass is problematic; the sampling volumes for the EPMA analyses are far smaller than a volume that may be considered as "representative" for a given melt pocket or vein. Indeed, the small sampling volume also causes individual spot analyses to be very sensitive to local small-scale heterogeneities in the glass. To mitigate this, several analyses on glass were performed for each shock melt region analyzed in order to create a population of analyses, from which an approximate average glass composition may be determined. WDS X-ray elemental maps were created for several shock melt pockets. WDS analysis of glass used a 15 nA beam with a 15 kV accelerating voltage and a 10 μm beam diameter. Count times were 30 s per peak with a 15 s background. Natural glasses, silicates, oxides, and sulfides were used as standards. 2σ uncertainties for major elements are about 0.7 wt% for SiO_2, 0.2 wt% for Al_2O_3, FeO, MgO, CaO, and Na_2O, 0.1 wt% for TiO_2, K_2O, P_2O_5, and SO_3, 0.05 wt% for Cr_2O_3, 0.04 wt% for MnO, and 0.02 wt% for Cl and NiO.

Areas within shock melt pockets are commonly composed principally of polycrystalline aggregates of microcrystals. For these regions, even a fully-focused electron beam is too large to analyze individual crystallites. As a compromise, a beam diameter of 15 μm was employed to determine an "average" composition for localized area. While this is not as ideal as analyzing individual phases, and each analysis area is sensitive to heterogeneities on the scale of a few microns, it is adequate for estimating the composition for an area of ~177 μm². As with glass, a

population of spots for each crystallite-rich area was analyzed to minimize the effect of local chemical variation.

Analysis of iron sulfide spherules within shock melt pockets was performed utilizing a 15 nA, fully-focused electron beam with an accelerating voltage of 15 kV. A population of larger spherules (several μm across, up to ~20 μm) were targeted by WDS. As the EPMA software reports chemistries in weight percent oxides, a sulfur-oxygen equivalency correction was performed following analysis.

2.5 Secondary ion mass spectrometry

Four glass-containing shock melt pockets in Tissint section MET11640/2-3-4/TEP were selected for secondary ion mass spectrometry (SIMS) analysis. SIMS was used to determine the abundance of volatiles within shock melt glass including chlorine, fluorine, sulfur, phosphorus, and water (as hydrogen), as well as to examine the hydrogen isotope composition of the glass. The glass was analyzed using a Cameca IMS 7f-GEO ion microprobe, located at the Caltech Microanalysis Center (Division of Geological and Planetary Sciences) at the California Institute of Technology. In order to fit into the instrument holder, the section was altered from a standard 1" × 2" slide to a 1" diameter round section, with double-thick glass. During the alteration process, the sample was damaged and was split into two halves. Although damaged, the two halves seated properly onto the slide to which they were mounted. The section was repolished, carbon-coated, then stored within the SIMS instrument to degas under high vacuum (1×10^{-8} torr) for three days prior to analysis. During analysis, vacuum pressures were ~$2\text{-}3\times10^{-10}$ torr.

A 5-6 nA, 10 μm diameter Cs^+ primary-ion beam was used for pre-sputtering. During analysis, the ion beam diameter was reduced to 2 μm. Each analysis spot was pre-sputtered for several minutes and was manually inspected by examining ion images of $^{16}O^1H^-$ in order to avoid cracks, holes,

and crystallites. Spots were pre-sputtered using a raster size of 25×25 μm. During analysis, this raster size was reduced to 10×10 μm. An electron gate limited the collection of ions from only the center 8×8 μm area. Ion species analyzed for concentration included $^{12}C^-$, $^{16}O^1H^-$, $^{18}O^-$, $^{19}F^-$, $^{30}Si^-$, $^{31}P^-$, $^{32}S^-$, and $^{35}Cl^-$. Natural and synthetic glasses were used as standards. For elemental concentrations, each analysis was run for 20 cycles, with a dwell time of 1 s per species. For hydrogen isotopes, each analysis was run for 100 cycles with a dwell time of 1 s for hydrogen and 15 s for deuterium. In order to directly compare water concentrations and δD, analysis spots for hydrogen isotopes were centered within pits excavated during analyses for volatile abundances.

Following SIMS analysis, pits excavated by the primary ion beam were inspected in transmitted and reflected light, as well as by SEM in backscattered and secondary electron mode; data from any spots that were found to have excavated microscopic cracks were discarded. Background levels for volatiles, estimated from repeat analyses of Tissint maskelynite in close proximity to shock melt pockets, are estimated to be about 50 ppm for water, 1 ppm for fluorine, 0.2 ppm for chlorine, and 0.2 ppm for sulfur, based on analyses performed by Chen et al. (2015) in the same laboratory, under similar analytical conditions, on the same meteorite.

2.6 Laser ablation inductively coupled plasma mass spectrometry

In order to investigate REE patterns, trace element abundances were determined using a New Wave UP213 laser ablation system and an iCapQ ICP mass spectrometer at ICPMS Laboratory of the Department of Earth and Atmospheric Sciences at the University of Alberta. For each sample, a population of shock melt pockets from were analyzed. 14 spots from four shock melt regions in MET11640/2-3-4/TEP, 11 spots from four melt regions in MET11640/2-3-2-TEP, and 12 spots from four shock melt regions in MET11640/2-2-1/TEP were analyzed. To compare shock melt pockets to the host rock, host rock phases in MET11640/2-3-4/TEP were analyzed in

a separate session with identical analytical conditions, including 13 analyses on olivine, 13 analyses on pyroxene, and 10 analyses on maskelynite. Due to the paucity and small size of merrillite in the sample, a single analysis was performed on merrillite, at a reduced spot size of ~25 μm. Glass standards from the National Institute of Standards and Technology (NIST612 and NIST614) were used as standards for trace elements. CaO concentration as determined by EPMA was used as an internal standard. Samples were ablated by a 10 Hz laser with a spot size of ~55 μm at ~9-10 J/cm^2. Each analysis was run for 60 seconds including a 25 second laser warm-up period, followed by a 20 second washout period. Dwell times for ion species were between 0.03 and 0.1 s.

2.7 HEAT thermal modelling

The HEAT program by Kenneth Wohletz (Wohletz et al., 1999), a freeware thermal modelling software, was used to better understand the post-shock cooling history of the shock melt. Following the method of Shaw and Walton (2013), the distribution of shock melt in Tissint was mapped in commercial image-processing software as a grid, with each spot in the grid assigned to one of groundmass rock, shock melt, or air (for vesicles). This map was then plotted onto a grid within the HEAT program. The distribution of shock melt was mapped on a 0.1 mm grid. Although a grid size of 0.1 mm is smaller than the minimum grid size of 0.01 m available in HEAT, the results may be scaled down to suit the scale of the meteorite by applying a scaling factor to the data output by the program (Shaw and Walton, 2013). For one shock melt pocket, the borders of the melt were extrapolated beyond the edge of the thin section, as the edge of the section cuts through the center of the pocket and disrupts two vesicles that are assumed to have been originally enclosed within glass. The dimensions of the melt pocket in this case were therefore extended such that the vesicles are symmetrical and enclosed by 0.2 mm of shock melt. Regions of shock melt

smaller than 0.1 mm^2 were ignored. For the model parameters, the bulk groundmass is assumed to have a density of 3000 kg/m^3, a thermal conductivity of 1.8 W/mK, and a heat capacity of 1000 $Jkg^{-1}K^{-1}$, appropriate for basalt. Shock melt is assumed to have a density of 2725 kg/m^3, a thermal conductivity of 2 W/mK, and a heat capacity of 1500 $Jkg^{-1}K^{-1}$. The initial temperatures were 2500 °C for shock melt and 500 °C for the groundmass. For the purposes of the model, vesicles are assumed to be filled with air, with a bulk density of 1.12 kg/m^3 and a heat capacity of 1004 $Jkg^{-1}K^{-1}$, with an initial temperature of 500 °C, the same as the groundmass temperature. Calculations were run until all melt had cooled to 900 °C, the approximate temperature of the basalt solidus (Shaw and Walton, 2013).

3. Results

3.1 Composition and mineralogy of shock melt pockets

Tissint is an olivine-phyric basalt, composed of olivine phenocrysts set in a groundmass of pyroxene and plagioclase (now maskelynite). Subhedral to euhedral olivine crystals are variable in size and range from microphenocrysts <1 mm to macrophenocrysts that are several mm across (Figure 3). Olivine is zoned from Mg-rich cores to Fe-rich rims. Micro-inclusions of Fe-Ti-Cr oxides are ubiquitous in olivine. All plagioclase has been converted by shock to maskelynite, and is now isotropic. Transformation of plagioclase to maskelynite is common in heavily-shocked meteorites, including the majority of Martian meteorites (Rubin, 2015). Other phases present include pyrrhotite ($Fe_{1-x}S$, x = 0 to 0.2), ilmenite ($FeTiO_3$), and merrillite ($Ca_9NaMg(PO_4)_7$). Apatite was not observed in any of the three sections studied here, but its presence has been documented in this meteorite in minor amounts (Chennaoui Aoudjehane et al., 2012).

Shock melt in Tissint is widespread (Figure 3). Shock veins permeate much of the rock and are typically found along grain boundaries. Shock melt pockets vary in size, morphology, and

crystallinity: while some melt pockets quenched to compositionally homogenous or schlieren-rich glass, others have quench-crystallized with equant euhedral to skeletal silicate microcrystals (Figures 4, 5, 6). Oxide crystals and spherules of iron sulfide are also common within shock melt pockets and veins in varying abundance. Sulfide spherules are round and are variable in size from <1 μm to ~20 μm at the largest.

Shock melt pockets all have a tendency to "coarsen" inwards: crystallinity and crystal size increase towards the center of the pocket or vein. A gradation is commonly seen from glass to crystallites to microscopic crystals ~2-10 μm in size. In the largest shock melt pocket in the center of Tissint section MET11640/2-2-1/TEP, dendritic crystals of pyroxene are up to 80 μm in length. The exception to this trend in crystal size is when vesicles are present: vesicles are enveloped by glass, and crystallinity increases away from the vesicle.

Ahrensite is observed within and adjacent to shock melt pockets and shock veins (Figure 4). This mineral does not occur within the interiors of larger melt pockets. Although the ahrensite observed here is too small (sub-micron crystals) to characterize by Raman spectroscopy, ahrensite was identified based on composition, texture, grain size, optical properties, and a similar petrologic setting to that reported by Ma et al. (2014): ahrensite appears as a "mottling" of microscopic (<<1 μm) grains in clasts of olivine within shock melt pockets. Tissintite was identified by textures in BSE images (crystalline textures associated with maskelynite, with a higher density than that of maskelynite), composition by EDS, and by Raman spectroscopy. Tissintite has two occurrences: as crystals within clasts of plagioclase glass within shock melt pockets, and as a "border" within maskelynite that is in direct contact with shock melt (Figure 4).

Ringwoodite is observed in olivine, but only in those grains associated with shock melt pockets and veins. Ringwoodite occurs as lamellae within larger olivine crystals; the lamellae are only present in olivine that is adjacent to a melt pocket or vein. This association between mineral

transformation and shock melt features has been reported from other meteorites, such as highly-shocked S6 chondrites: the heat leftover from the generation of the shock melt provides the energy required to overcome the phase transition boundary from olivine to ringwoodite at high pressures generated by the passing shockwave (Sharp and DeCarli, 2006; Chen et al., 2007; Miyahara et al., 2010; Greshake et al., 2013). Ringwoodite lamellae in Tissint are identified by their similar appearance to naturally-occurring ringwoodite in other highly-shocked meteorites, such as a brighter greyscale expected from denser phases with similar composition (Figure 5).

In olivine crystals that are within, or are in direct contact with shock melt veins or pockets, a microtexture of sub-micron granules is observed (Figure 5). This granular texture is attributed to the presence of amorphized silicate perovskite (bridgmanite, $(Mg,Fe)SiO_3$), and magnesiowüstite, formed by dissociation of olivine at high pressures and high temperatures, characterized by Miyahara et al. (2011), Hu et al. (2013), and Walton et al., (2014).

The composition of shock melt pockets is heterogeneous on a microscale (Figure 6). When comparing individual WDS analyses, chemical variation is observed mostly in Al, Ca, Fe, Mg, and Al. Aluminum and calcium abundances are correlated, and these elements are anti-correlated with magnesium and iron. High Al_2O_3 (>8 wt%) and high CaO (>10 wt%) correspond to schlieren or blebs within the glass that appears darker (lower density) than average glass in BSE images. EPMA analyses on crystallite-rich regions are in good agreement with those regions comprised entirely of homogeneous glass (Table 1). In those analyses where chlorine was detected, chlorine concentration was near the lower limit of detection (LOD) (0.02 to 0.04 wt%). For all analyses, chlorine concentration was below the limit of determination, equal to six standard deviations of the background above the mean background counts, or twice the lower limit of detection (Potts, 1992).

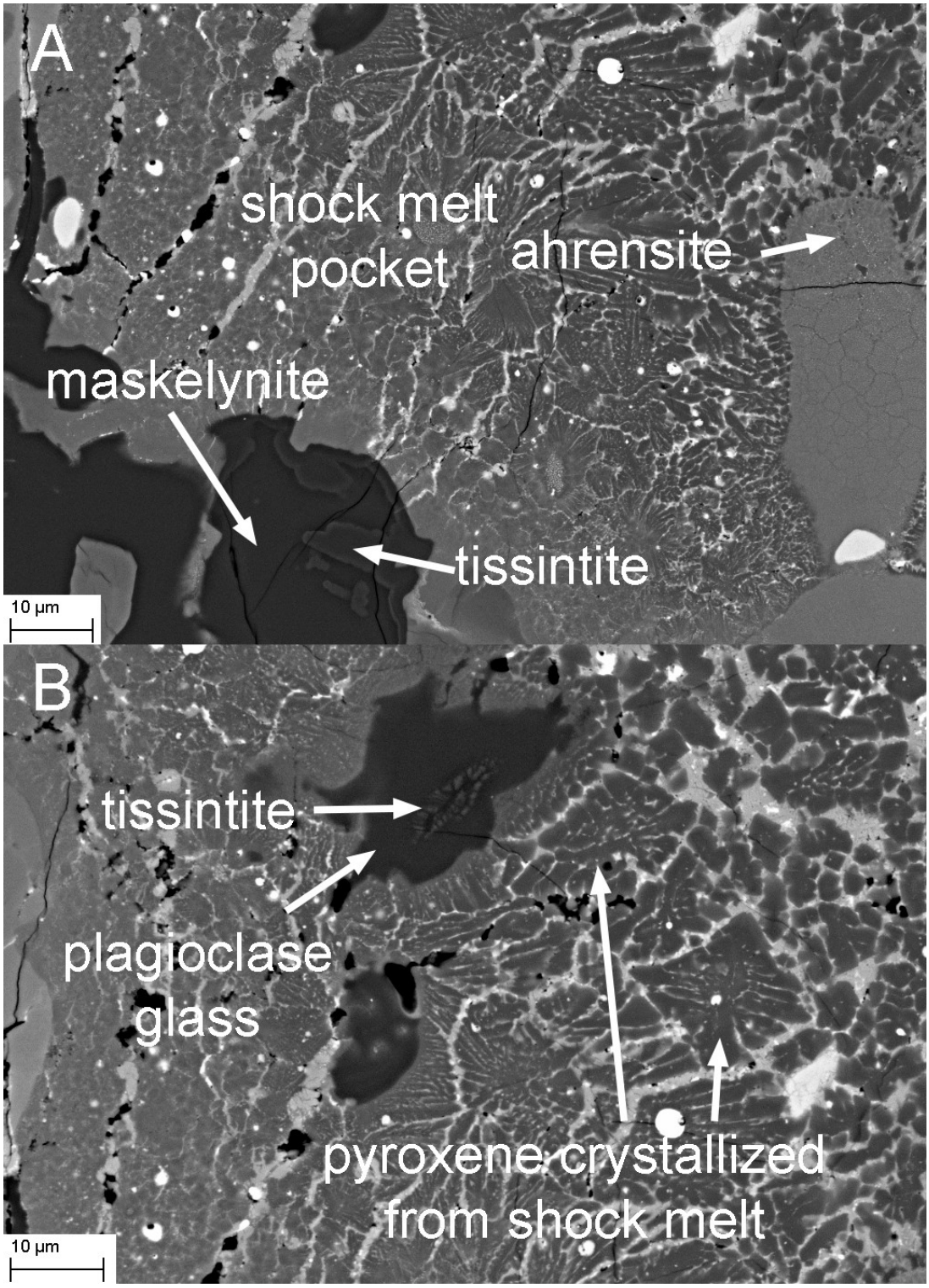

Figure 4. BSE images of high-pressure phases tissintite and ahrensite within shock melt pockets. A: Tissintite is present within maskelynite in contact with the shock melt pocket. Sub-micron scale ahrensite crystals formed from olivine at high pressure. B: Tissintite within a clast of plagioclase glass inside a shock melt pocket. Pyroxene has quench-crystallized from the shock melt as microcrystals.

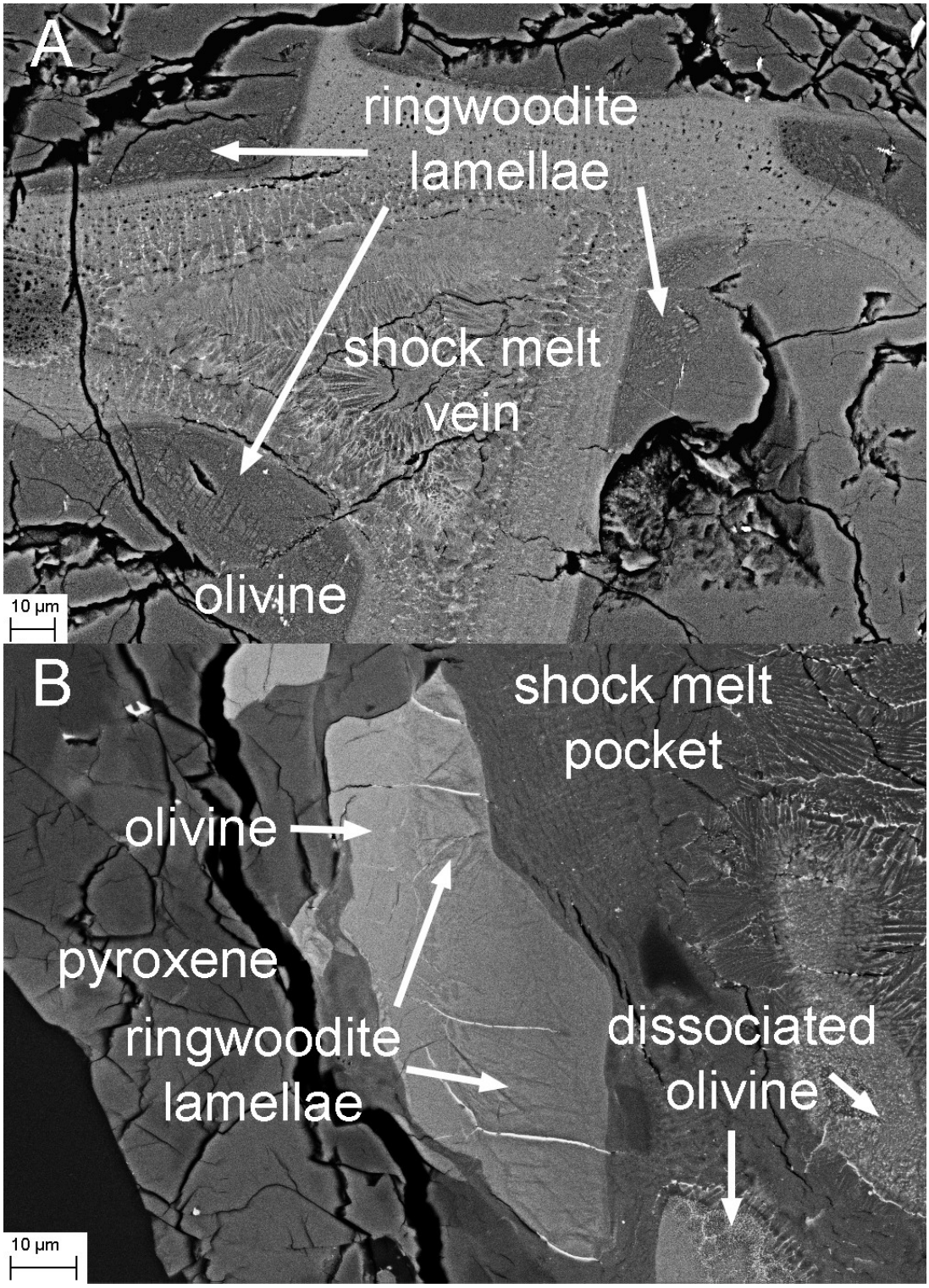

Figure 5. BSE images of high-pressure phases associated with olivine within and adjacent to shock melt pockets and veins. A: Ringwoodite lamellae in an olivine crystal in contact with a shock melt vein. Crystallinity within the shock melt vein increases towards the center. B: Ringwoodite lamellae in an olivine crystal in contact with shock melt. Olivine entrained as clasts within shock melt has dissociated to silicate perovskite (bridgmanite) and magnesiowüstite.

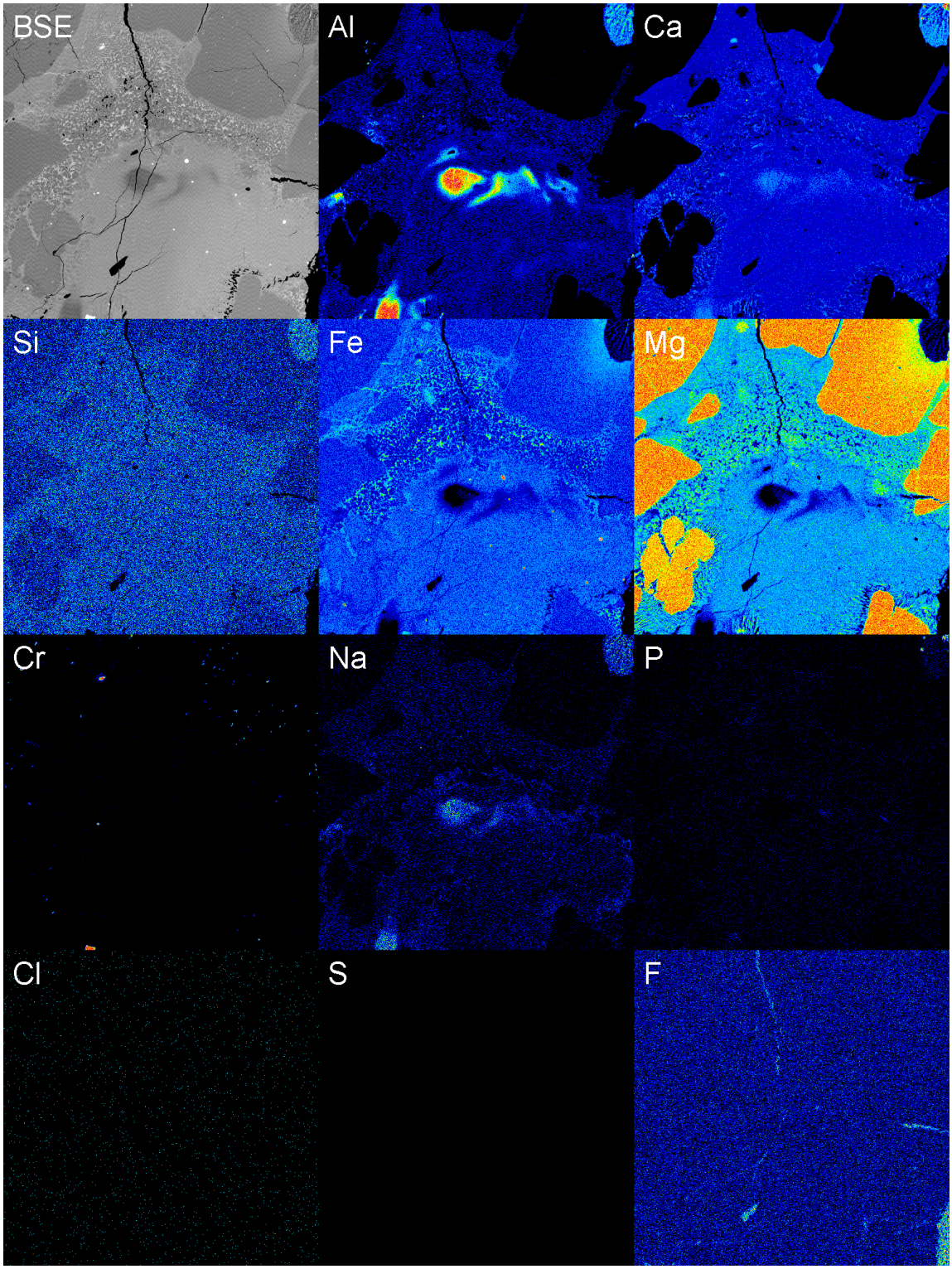

Figure 6: WDS X-ray elemental maps for a shock melt pocket within MET11640/2-2-1/TEP. Flow textures are visible in glass, most visible in the maps for Al, Ca, Fe, Mg, and Na. Fluorine "hot-spots" correspond to cracks and holes within the section; these hot-spots are attributed to epoxy. Field of view = 500 µm.

	MET11640/2-2-1/TEP				MET11640/2-3-2/TEP				MET11640/2-3-4/TEP	
	glass		crystallites		glass		crystallites		glass	
	average	σ	average	σ	average	σ	average	σ	average	σ
SiO_2	48.62	1.17	48.91	2.22	49.83	0.94	49.22	2.18	48.55	1.98
TiO_2	0.45	0.06	0.44	0.16	0.50	0.04	0.49	0.22		
Al_2O_3	4.91	3.66	3.29	1.07	4.55	1.09	3.26	1.20	3.77	2.61
Cr_2O_3	0.71	0.15	0.73	0.19	0.60	0.06	0.55	0.14	1.20	
FeO	19.30	2.34	19.18	1.96	18.34	1.07	19.62	2.66	19.25	2.46
MnO	0.55	0.07	0.56	0.04	0.54	0.04	0.58	0.05	0.57	0.05
MgO	17.27	2.40	18.80	2.96	15.50	0.82	17.06	1.78	17.45	2.46
CaO	7.58	0.83	7.31	1.81	8.35	0.71	7.85	1.45	8.28	1.64
Na_2O	0.47	0.41	0.36	0.15	0.66	0.20	0.43	0.18	0.47	0.33
K_2O	0.02	0.01	0.02	0.01	0.04	0.05	0.02	0.01		
P_2O_5	0.31	0.09	0.32	0.74	0.25	0.11	0.20	0.09	0.33	0.17
SO_3	0.30	0.11	0.41	0.40	0.47	0.20	0.83	0.73	1.36	0.67
Cl	0.02	0.00	0.02	0.01	-	-	-	-		
NiO	0.03	0.01	0.04	0.02	0.03	0.01	0.03	0.01	-	-
	100.48		100.32		99.62		100.01		98.86	

Table 1: Representative compositions of Tissint shock melt, determined by EPMA. Blank values indicate measurements below the lower limit of detection. Values demarcated by "-" indicate species that were not targeted for analysis in the sample.

X-ray elemental maps for melt pockets demonstrate that the shock melt pockets are compositionally heterogeneous and exhibit flow textures and schlieren (Figure 6). X-ray maps are also useful for identifying merrillite, which is present in relatively low abundance (< 1%), small (up to ~35 μm), and is similar in appearance to maskelynite in these samples in transmitted and reflected light, and BSE imagery. Merrillite was identified in X-ray maps by grains demonstrating a component of each of Ca, Na, Mg, and P; identification was confirmed by Raman spectroscopy.

X-ray elemental maps demonstrate that there are no significant excesses (or "hot spots") of chlorine, fluorine, phosphorus, or sulfur associated with the shock melt glass. Some fluorine is detectable by X-ray mapping within cracks and holes in the section; this excess fluorine is attributed to epoxy and is not native to the rock.

3.2 Shock metamorphic sulfides

WDS analyses of sulfides indicate that iron-sulfide spherules within shock melt pockets have different chemistries than the iron sulfides within the groundmass portion of the rock. Groundmass sulfides are pyrrhotite in composition, with an average composition of $Fe_{0.89}S$. In contrast, the iron sulfides that appear as spherules within the shock melt have elevated iron to sulfur ratios (Figure 7). For one shock melt pocket, the average composition of sulfide spherules is on average well above that of troilite (FeS).

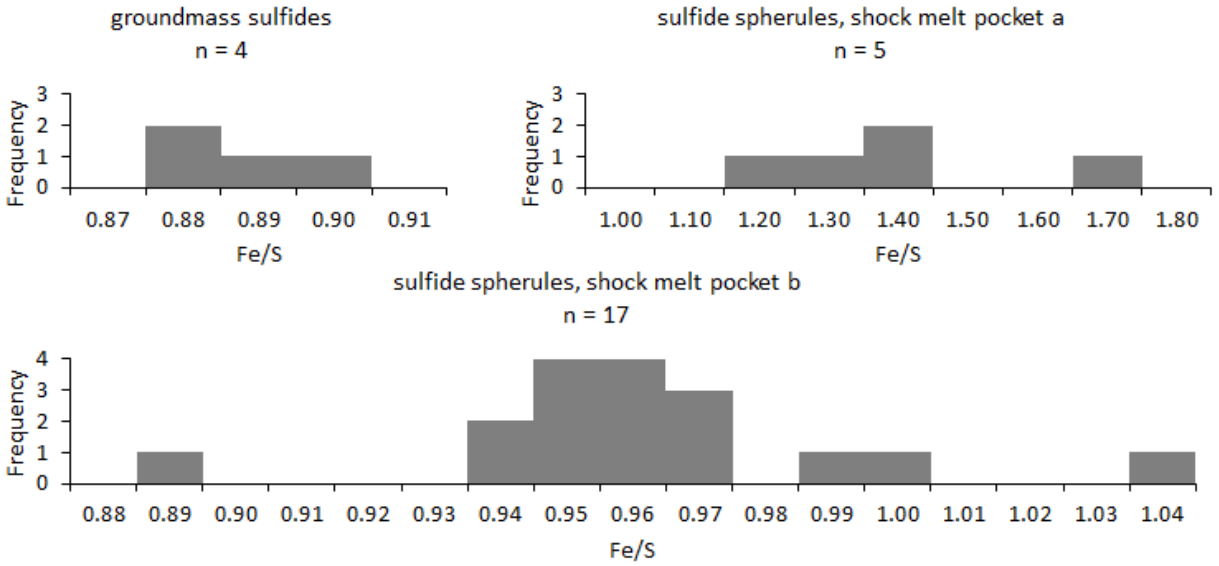

Figure 7: Fe:S histograms for sulfides in MET11640/2-3-4/TEP. Fe/S values for sulfide spherules within shock melt pockets are elevated relative to groundmass pyrrhotite.

3.3 Observations from Raman spectroscopy

Raman results are given in Figure 9 and Figure 10. Olivine, chromite, pyroxene, and apatite exhibit Raman spectra typical of crystalline rocks with high intensity, narrow peaks. The exception is maskelynite: while crystalline plagioclase will exhibit strong Raman peaks, the transition to maskelynite alters the Raman spectrum. As a result, the Raman spectra for feldspars are altered: the largest peak in the spectrum is moved to a lower Raman shift, and the effect is a shortening

and a broadening of the Raman peak, until it is a wide "hump" centered over ~499 cm^{-1}. For spectra collected from high-density lamellae within olivine crystals in contact with shock melt, Raman spectra contained strong peaks at ~820 and 845 cm^{-1}, characteristic of olivine. Raman spectra collected from the higher-density borders of maskelynite grains that are in contact with shock melt pockets and veins exhibited broad Raman peaks centered over ~380, 693, and 997 cm^{-1}, consistent with Raman peaks reported for tissintite by Ma et al. (2015).

Raman spectra for host rock pyrrhotite exhibit two strong peaks at 330 cm^{-1} and 380 cm^{-1}. Raman analysis was also performed for iron-sulfide spots within shock melt pockets. Spectra collected from these spherules occasionally those contain extra peaks that are not present within spectra collected from igneous pyrrhotite. These peaks at 218 and 282 cm^{-1} are characteristic of hematite. In these spots, sulfide spherules exhibit an elevated Fe:S, determined by EPMA. Within one shock melt pocket, a large clast of pyrrhotite is present adjacent to the shock melt (Figure 8). Here, the Raman spectrum collected for this pyrrhotite crystal does not contain peaks characteristic of hematite, while abundant sulfide spherules within the shock melt pocket do exhibit such peaks.

3.4 Volatile abundances in shock melt glass

Water content in shock melt pockets in Tissint is highly variable, ranging from <100 ppm to several thousand ppm between regions of shock melt within MET11640/2-3-4/TEP (Figure 11). Water is positively correlated with chlorine, but not correlated with fluorine, phosphorus, or sulfur (Figure 11). δD values in Tissint glass ranged from ~2600 ‰ to ~4340 ‰. δD is negatively correlated with $1/H_2O$ (Figure 12). In one area that contains texturally homogeneous glass, ion probe traverses reveal that water content decreases and δD increases when a large vesicle is approached (Figure 13).

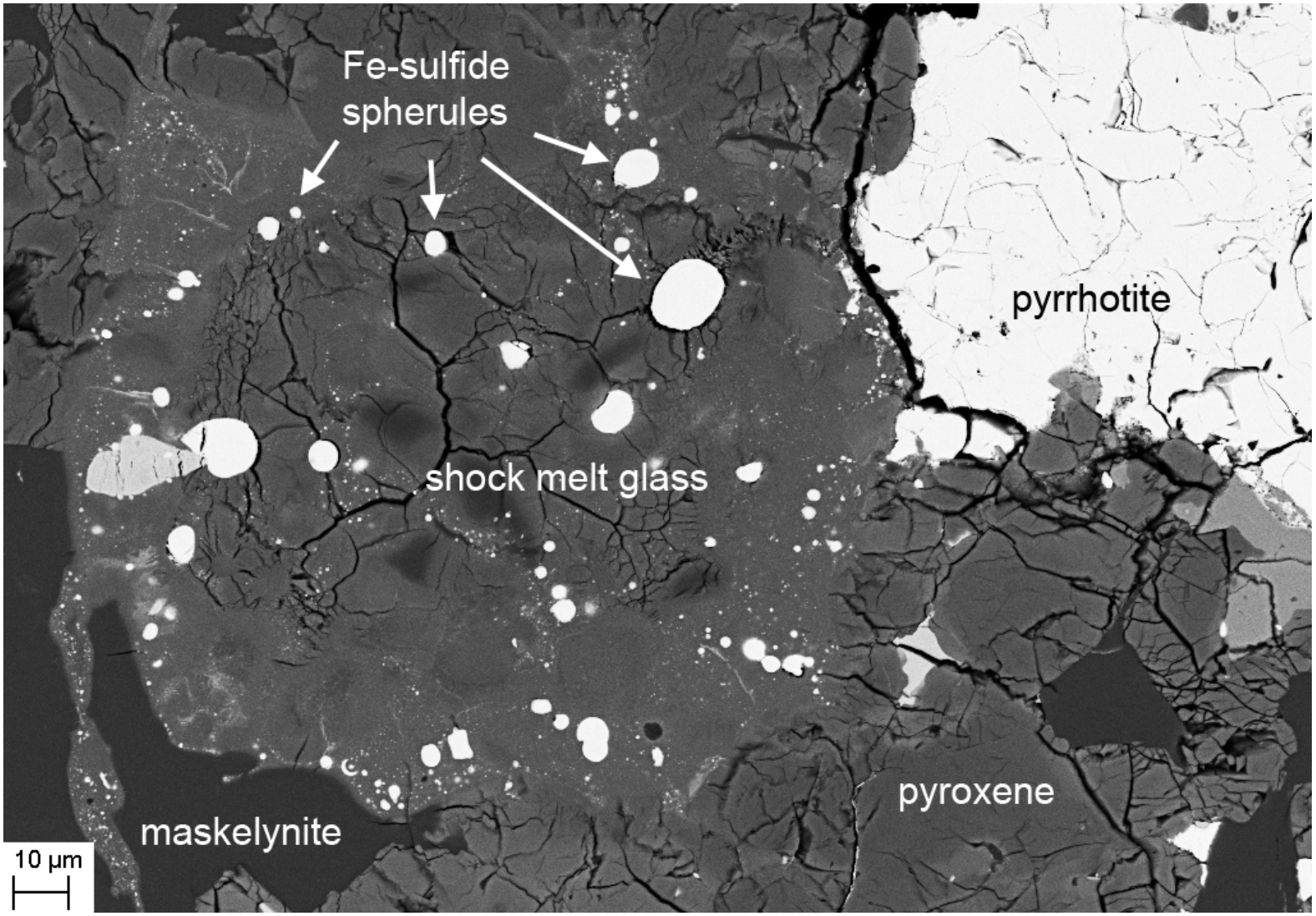

Figure 8: BSE image of a shock melt pocket containing abundant iron sulfide spherules entrained within shock melt glass; these spherules comprise the population for melt pocket b in Figure 7. The pyrrhotite grain in the top right has a composition of $Fe_{0.88}S$.

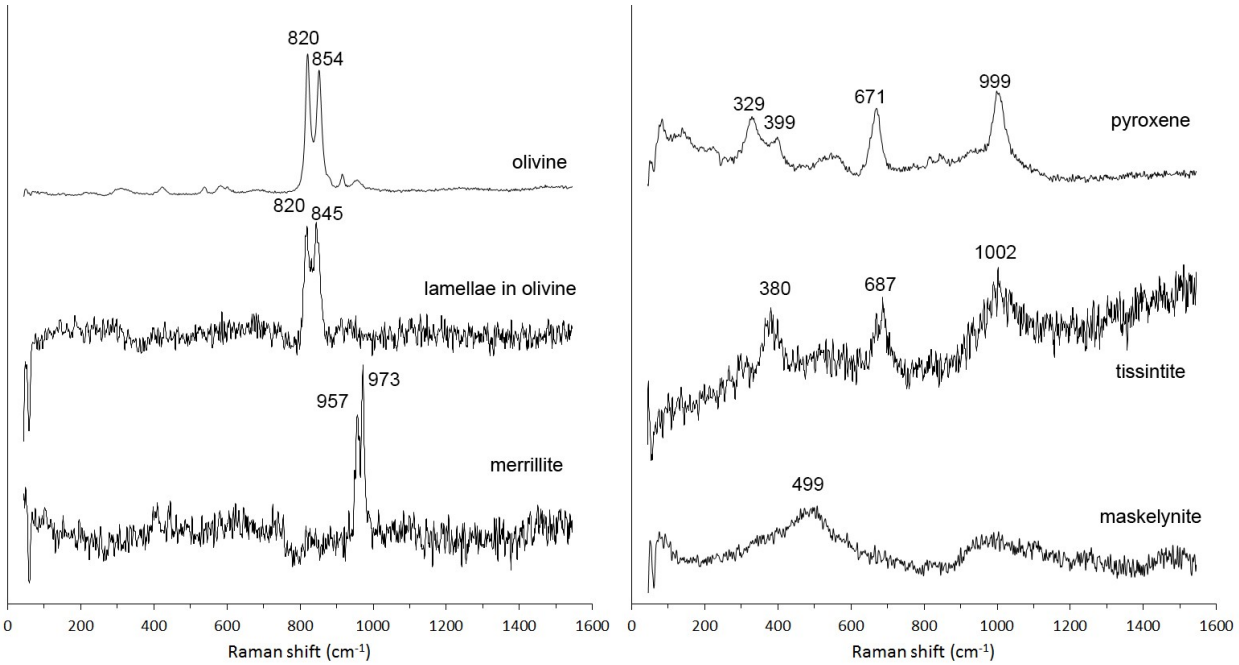

Figure 9: Representative Raman spectra for minerals in Tissint. The maskelynite Raman spectrum was collected from the core of a grain, while the tissintite Raman spectrum was collected from the boundaries of that grain in contact with a shock melt pocket; the petrologic context is similar to that in Figure 4A.

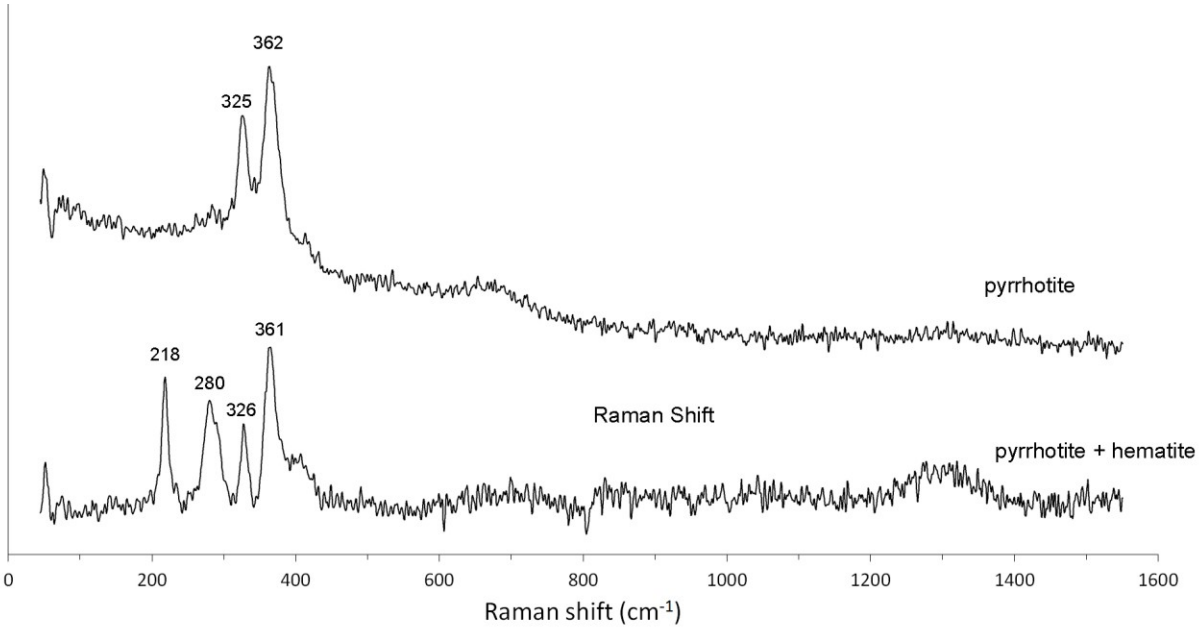

Figure 10: Representative Raman spectra for iron sulfides in Tissint. Top: Raman spectrum from an igneous sulfide with peaks at 362 and 325 cm^{-1}, characteristic of pyrrhotite. Bottom: Raman spectrum from an iron sulfide spherule within a shock melt pocket. In addition to peaks characteristic of pyrrhotite, the spectrum contains additional peaks at 218 and 280 cm^{-1}, characteristic of hematite.

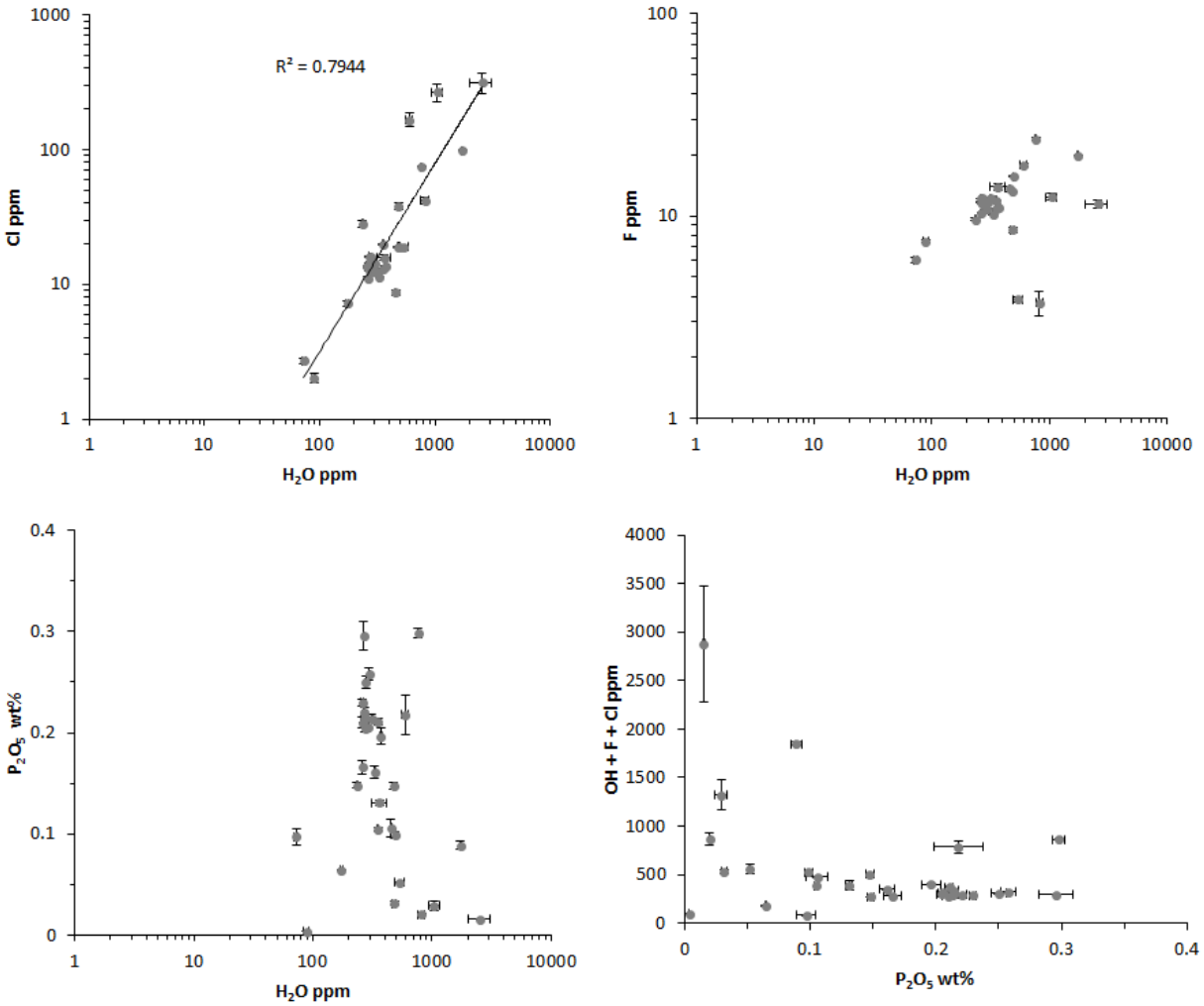

Figure 11: Volatile abundances in Tissint shock melt glass as measured by SIMS. Chlorine is positively correlated with water. Fluorine and phosphorus exhibit no correlation with water concentration. A combination of water, fluorine, and chlorine is not correlated with phosphorus content.

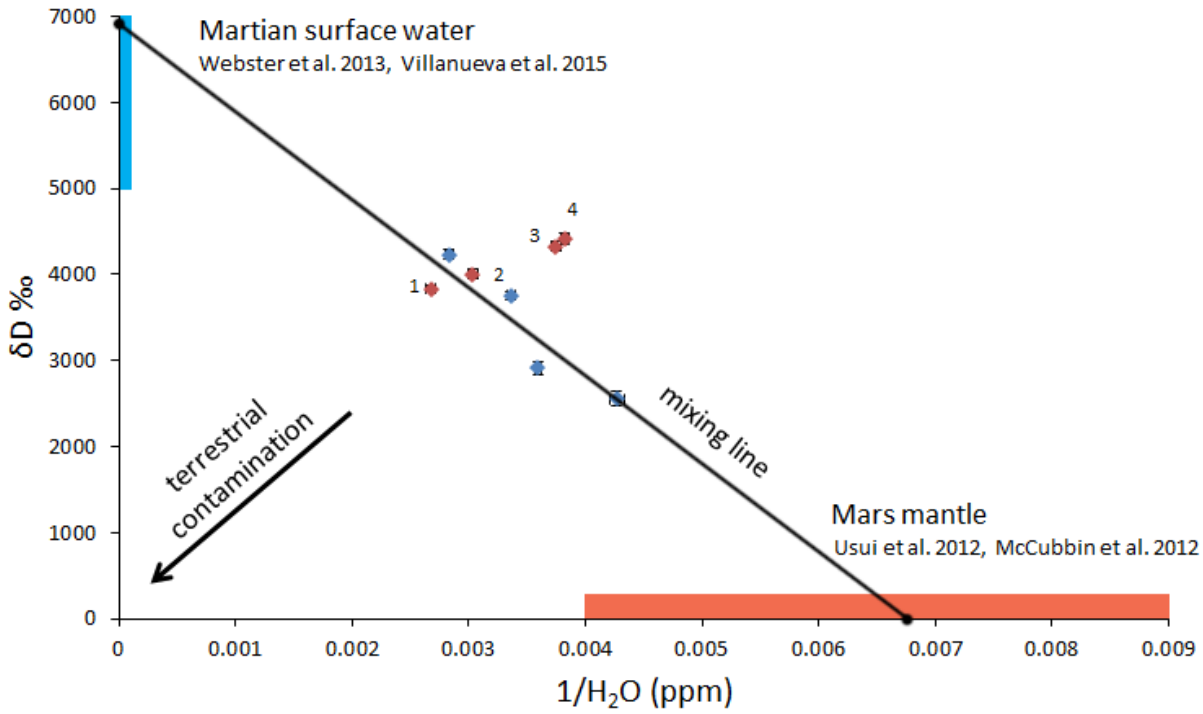

Figure 12: δD values versus1/H_2O for Tissint shock melt glass. Numbered points correspond to SIMS spots within glass labeled in Figure 13. The mixing line is calculated by regressing a line through the data, excluding points labelled 3 and 4; R^2 = 0.82. Y intercept = 6924 δD; X intercept = 0.00675 1/H_2O (148 ppm H_2O).

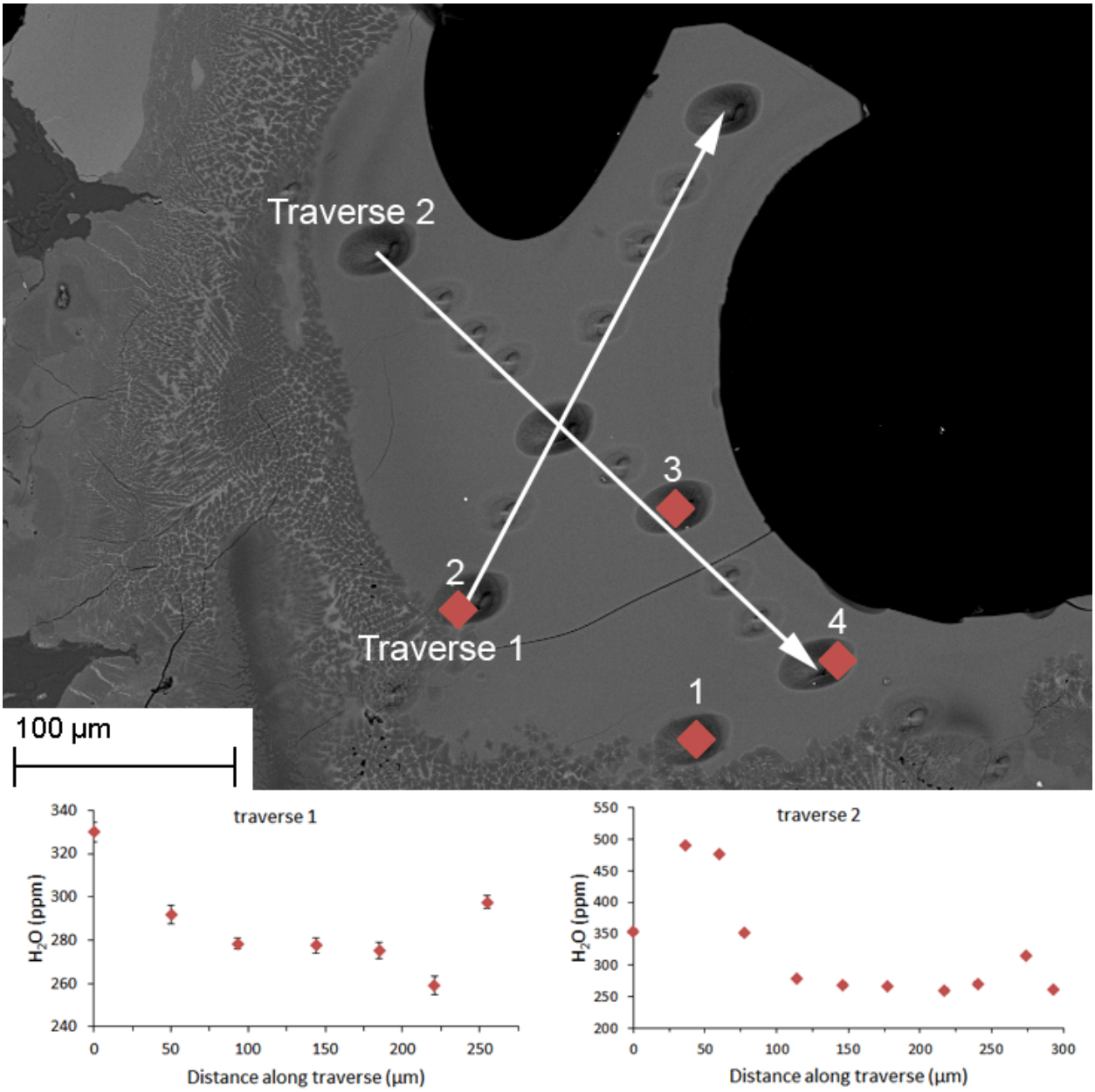

Figure 13. Top: BSE image of a shock melt pocket with vesicles (black, top right). Near the vesicles, the shock melt has quenched to glass. Pits in the glass indicate spots excavated by the primary ion beam during SIMS analysis. δD values for spots indicated by diamonds are reported in Figure 12. Bottom: traverses through the glass demonstrate that H_2O content in glass decreases with proximity to the large vesicle.

3.5 Trace element concentrations in shock melt pockets

Results of LA-ICP-MS analyses are given in Figure 14. Data were normalized against elemental abundances in CI chondrites reported by Palme et al. (2014). Olivine has a relatively low REE abundance compared to the other minerals. Pyroxene and maskelynite have similar abundances of rare earth elements, although maskelynite exhibits a distinctive positive europium anomaly. Pyroxene, olivine, and maskelynite are depleted in LREE, which is typical for depleted shergottites (Figure 14). Although only one merrillite analysis was possible, results are generally consistent with REE reported for Tissint merrillite (Balta et al., 2015; Liu et al., pers. comm.).

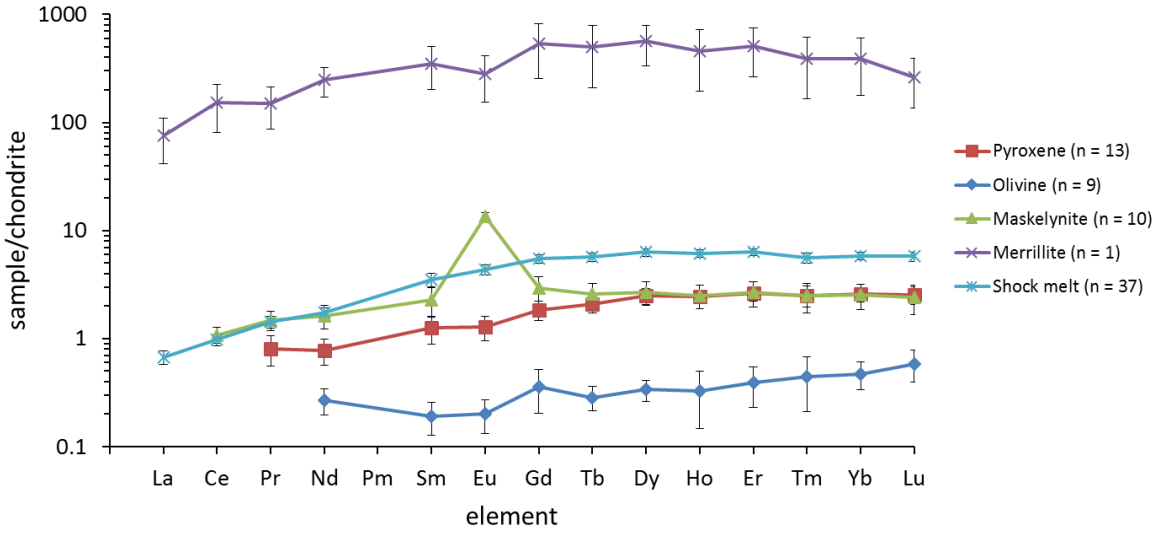

Figure 14. Average CI-normalized REE abundances for Tissint. Groundmass minerals were measured for MET11640/2-3-4/TEP. Shock melt REE abundances are averaged for 37 analyses across all three thin sections examined here.

Shock melt, both for areas that were texturally homogeneous and glassy, and for crystallite-rich areas with interstitial glass, exhibit little variation in trace element abundances between different regions of shock melt, or between sections (Figure 15). Tissint shock melt contains a higher concentration of rare earth elements than the country rock silicates, and is depleted in LREE. No evidence for LREE enrichment or a positive cerium anomaly was observed.

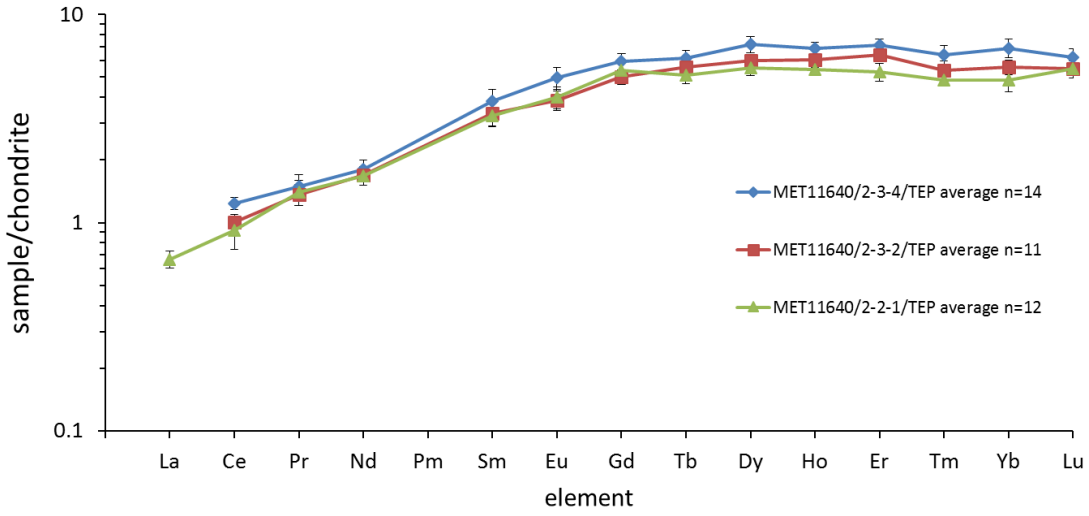

Figure 15. Average trace element abundances for Tissint samples. There is little variation in trace element concentrations between samples. The shock melt pockets are depleted in LREE, with concentrations similar to those reported by Barrat et al., 2014.

3.6 Cooling history of shock melt pockets modelled by HEAT

The distributions of shock melt within the three thin sections are shown in Figure 16. Tissint MET11640/2-3-4/TEP contains seven modelled shock melt pockets, the largest pocket being <0.5 mm^2; HEAT results calculate that it cooled completely to the solidus in 0.14 s. Tissint MET11640/2-3-2/TEP contains slightly more melt volume with larger melt pockets, and cooled to the solidus in 0.50 s. Tissint MET11640/2-2-1/TEP contains considerably more melt than the other sections, with a large abundance of shock melt; the melt in this section cooled much more slowly, with all melt cooling to the solidus within 2.60 s. Within this section, small isolated pockets cooled very quickly, while heat persisted near the center of the section, where the heat from several large, closely-spaced melt pockets constructively interfered.

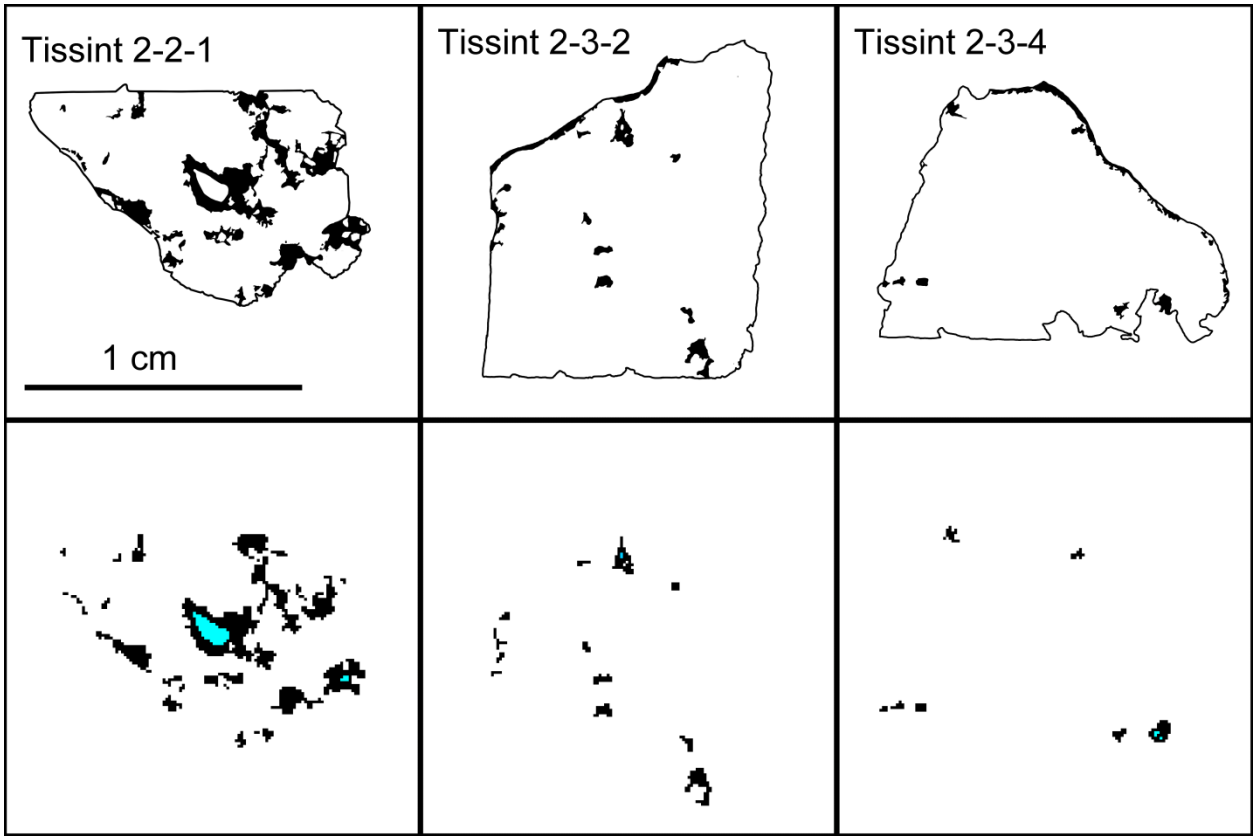

Figure 16. Top: digital sketches showing the distribution of shock melt in the three thin sections of Tissint (cf. Figure 3). Bottom: initial model conditions for shock melt pockets, mapped onto a 0.1 mm grid within the HEAT program. Blue is air, black is shock melt, and white is host rock.

Notably, areas that contain dendrite-poor or dendrite-free glass correspond to those areas within the model that cooled the fastest. The largest skeletal and dendritic crystals of both olivine and pyroxene are correlated to those regions in the model that remained above solidus for extended periods of time; for example, relatively large dendritic crystals are seen within the center of large pockets within Tissint MET11640/2-2-1/TEP (Figure 17). Shock melt pockets containing vesicles cooled considerably faster than shock melt pockets of similar size that were vesicle-free. Modeling demonstrates that shock melt adjacent to a vesicle will solidify first, and the solidification front will radiate outwards from the vesicle.

Results of HEAT modeling demonstrate that the cooling time for shock melt pockets in each of the three thin sections is rapid. Small, isolated shock melt pockets cool much more

rapidly than those shock melt pockets that are large and proximal to other pockets or veins. Individual shock melt pockets that contain vesicles cooled considerably faster than those that were vesicle-free, with regions immediately adjacent to a vesicle cooling the fastest.

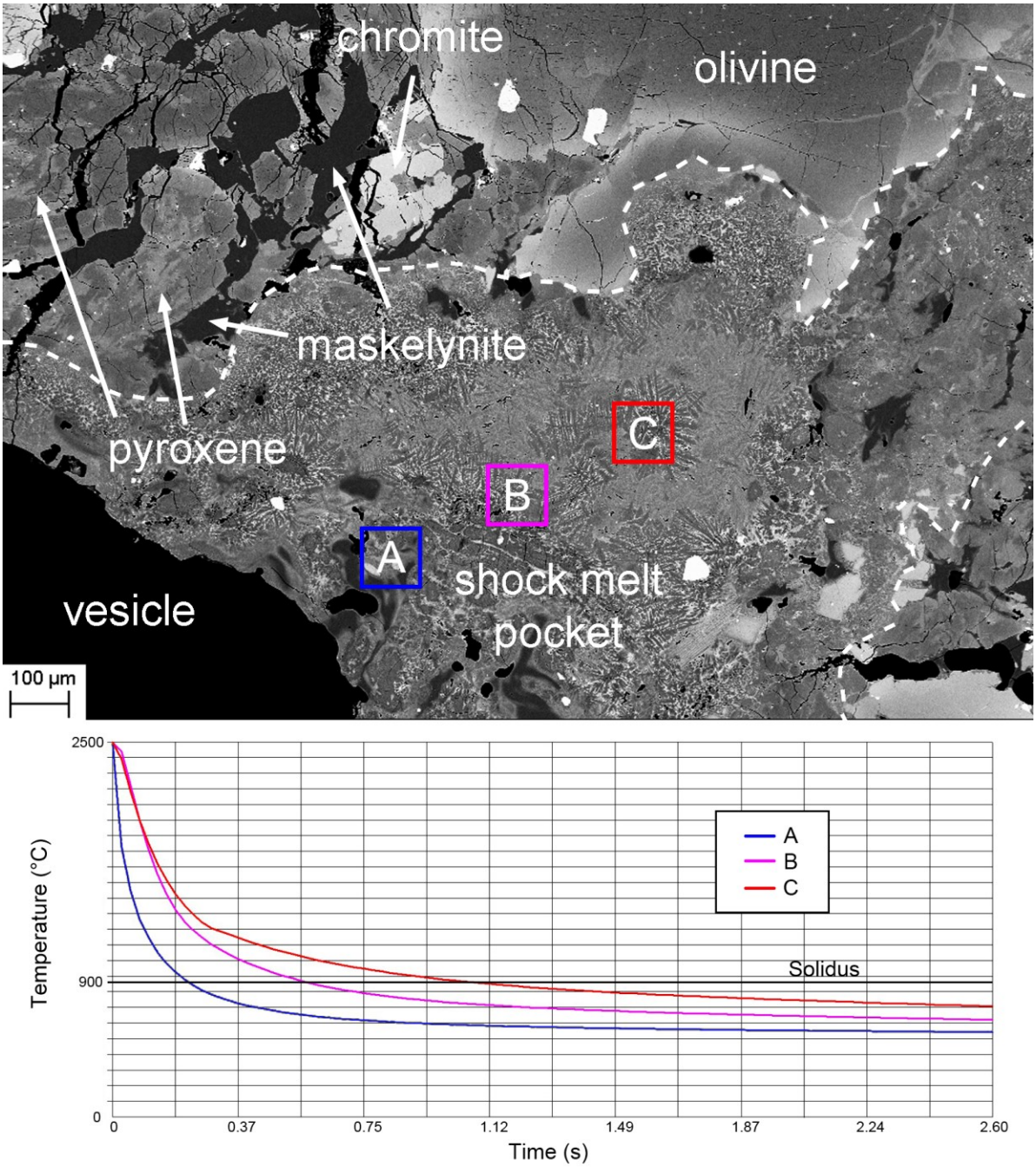

Figure 17. Cooling profiles for three points within a large vesiculated shock melt pocket in Tissint section MET11640/2-2-1/TEP. Point A, nearest to the vesicle, cools the fastest, cooling to the solidus in 0.22 s. Further from the vesicle, point B solidifies in 0.57 s. Point C, near the center of a large region of shock melt, cools to the solidus in 1.07 s.

4. Discussion

4.1 Major, minor, and trace elemental compositions of shock melt pockets

EPMA demonstrated a basaltic composition for shock melt glass, consistent with the melting and mixing of local igneous phases. The major and minor elemental compositions of silicate glass and crystallites within both shock melt pockets and veins in Tissint reflect the melting and incorporation of local igneous minerals in varying abundances. Aluminum and calcium (wt% oxides) co-vary, as do iron and magnesium; this covariance may be attributed to the melting and incomplete mixing of the major igneous silicate minerals - namely plagioclase, pyroxene, and olivine - to specific spots within a melt pocket, leading to compositional heterogeneities. In all cases where examined by EPMA, chlorine was below the limit of determination, and no "hot-spots" of chlorine, fluorine, or phosphorus were detected within X-ray maps. X-ray elemental maps and WDS and EDS analyses on shock melt pockets suggest an absence of significant igneous apatite within Tissint shock melt glass. All phosphates detected here contain significant sodium and magnesium, which are not present in major amounts in apatite. Additionally, all phosphates analysed by Raman spectroscopy demonstrated a double-peak with centers at 957 and 973 cm^{-1}, characteristic of merrillite (Figure 9). Potassium contents of shock melt pockets are consistent with that reported for the bulk rock (Chennaoui Aoudjehane et al., 2012); there is no evidence for incorporation of a K-rich alteration phase such as jarosite ($KFe^{3+}_3(OH)_6(SO_4)_2$).

Individual mineral phases are depleted in LREE, which is typical for depleted shergottites, and their trace element abundances are in good agreement with abundances reported by other authors (Chennaoui Aoudjehane et al., 2012; Barrat et al., 2014; Balta et al., 2015). Trace element abundances for shock melt pockets are depleted in LREE and reflect bulk Tissint, similar to bulk and glass analyses reported by Chennaoui Aoudjehane et al. (2012) and Barrat et al. (2014). Shock melt pockets typically exhibit a higher abundance of HREE than what could be contributed from

any combination of the dominant igneous phases (pyroxene, olivine, or maskelynite); this can be explained by a minor contribution of merrillite to the shock melt, <0.5%. Even a minor amount of merrillite incorporation is able to account for this enrichment, as merrillite is the main REE carrier in Tissint, hosting the overwhelming majority of rare earth elements in the meteorite (Balta et al., 2015).

Similar to Barrat et al. (2014), a cerium anomaly is not observed for Tissint shock melt pockets, and an enrichment in light rare earth elements relative to igneous minerals is not observed. Therefore, an extraneous LREE-bearing component is not required to explain the REE patterns of Tissint shock melt pockets. The trace element abundance of Tissint shock melt reflects the melting and mixing of local igneous phases into the shock melt.

4.2 Hematite as evidence for oxidation during shock metamorphism

Terrestrial alteration of meteorites can result in secondary mineralization, including by hematite, even in hot deserts in a relatively short time (e.g., tens of years; Barrat et al., 1999); however, it is unlikely that Tissint experienced significant weathering during its 3-month residence on Earth prior to collection (Chennaoui Aoudjehane et al., 2012). In Tissint, hematite is only present within shock melt pockets and is associated with sulfide spherules. Raman spectra collected on igneous pyrrhotite do not exhibit Raman peaks characteristic of hematite; those Raman peaks characteristic of hematite were only observed within shock melt pockets.

Hematite has been documented in other shergottites. Hematite identified by Raman spectroscopy in EETA79001 exhibited sharp peaks with high signal to noise ratios, interpreted to be well-crystallized hematite that was not formed by *in situ* oxidation by laser damage (Wang et al., 2004a; Wang et al., 2004b). However, the authors did not rule out an origin by terrestrial weathering. Hematite has also been identified by Raman spectroscopy in Zagami (a fall, Wang et

al., 1999). In Zagami, hematite appears as grains adjacent to pyrrhotite. In both EETA79001 and Zagami, it has been suggested that the hematite is original to the meteorites (i.e., Martian), and not a consequence of terrestrial weathering or oxidation induced by the Raman excitation laser, and therefore the meteorites must have experienced a highly-localized oxidation event (Wang et al., 1999; Wang et al., 2004a; Wang et al., 2004b).

Sulfide spherules are common within shergottite shock melt glass, and are derived from preferential melting of igneous sulfides due to their high compressibility and low melting temperature (Ross et al., 2013; Walton et al., 2010). These sulfides become incorporated immiscibly into the silicate melt (Walton et al., 2010). Sulfide spherules within Tissint shock melt glass are chemically distinct from the country rock sulfides from which they are derived: iron to sulfur ratios for metamorphic sulfides within shock melt pockets are elevated relative to those in the regions of the rock that was not shock-melted (Figure 7), implying that the sulfides were altered after the rock's emplacement. Altered Fe/S in shock-metamorphic sulfides has been observed in Tissint and other shergottites by previous workers (Ross et al., 2013; Sutton et al., 2014).

An alternative origin for sulfide spherules with Fe/S ratios >1 has been suggested: rather than being derived from melted igneous sulfides, Ross et al. (2013) hypothesized that an additional precursor component – namely, a trapped sulfate (e.g., jarosite) – within the shock melt was shock-reduced to sulfide. However, given the relatively high water content within Tissint shock melt pockets (>2500 ppm for some melt pockets) and that the Amazonian (the Martian geologic period from ~3.0 Ga to present) atmosphere is relatively oxidizing, not reducing, shock oxidation is more likely than shock reduction. Additionally, the EPMA and SIMS analyses on Tissint shock melt glass undertaken in this study do not provide evidence for a significant jarosite component, which would be detectable by excess potassium, sulfur, and water.

The nature of hematite in Tissint is of interest, as it is not a phase that would be in equilibrium with the igneous host rock: formation of hematite represents a much higher oxygen fugacity than that represented by the Fe-bearing phases (olivine, pyroxene, spinel and iron-titanium oxides) present within the igneous regions of the meteorite. The igneous crystallization conditions for Tissint were QFM -3.5 to -4.0 (Balta et al., 2015), much lower than the oxygen fugacity required to allow the formation of hematite above the MH buffer. As such, the formation of hematite simply by melting local igneous phases and incorporating them into a shock melt pocket before solidification may be ruled out; some oxygenation event is necessary to raise the oxygen fugacity that is inherent to the igneous rock. The oxidizing event that allowed for the formation of hematite was likely associated with the formation of the shock melt pockets. The source of the oxidizing agent may be Martian atmosphere within open pores or fractures in the pre-shocked rock. Alternatively, if the cracks and fractures within the rock were infiltrated by water, shock-loading may induce localized hydrothermal alteration, including the oxidation of iron (Kieffer and Simonds, 1980; Feldman, 1994). Another possibility is that the hematite formed by aqueous alteration prior to the formation of the shock melt pockets, and its origin is unrelated to shock metamorphism. However, since the iron-bearing phases in the groundmass show no signs of significant alteration (from alteration textures or from compositions from EPMA), and sulfides with elevated Fe/S values are restricted to shock melt pockets and veins, shock oxidation is more likely. Preliminary identification of hematite within a shock melt pocket may prove to be a useful indicator that an individual portion of shock glass is a viable candidate for searching for a near-surface signature.

It should be noted that it is possible to induce the oxidation of sulfides with a high-power Raman excitation laser. The oxidation of pyrrhotite by a Raman laser has been demonstrated for laser powers of 25 mW in an oxidizing environment (normal air, Mernagh and Trudu, 1993; Avril

et al., 2013). Under such conditions, heat from the laser builds up in the opaque mineral, accommodating oxidation. Such laser powers are an order of magnitude higher than the laser power used to collect Raman spectra on Tissint sulfide here; a low-power excitation laser of 2 W is unlikely to induce oxidization in pyrrhotite. After subjecting individual grains of pyrrhotite to repeated exposure to the Raman laser or allowing the laser to dwell on the mineral for several minutes, no change in the Raman spectrum was observed.

A mechanism then is proposed: the rock crystallized at relatively low oxygen fugacity conditions of QFM-4, and was then emplaced near the Martian surface (Balta et al., 2015). During its residence on Mars, cracks formed within the rock, allowing exposure to the Martian atmosphere. During an impact event, shockwaves concentrated into these cracks and fractures, closing them via void collapse, generating a shock melt pocket that incorporates an oxidizing agent derived from the Martian near-surface. Shock-oxidation would therefore explain the elevated Fe/S ratios observe for shock metamorphic sulfides, and the presence of hematite. Under oxidizing conditions, pyrrhotite will oxidize to hematite (via magnetite) at temperatures >450 °C (Dekkers, 1990); such temperatures are easily exceeded during shock melt pocket generation (Sharp and DeCarli, 2006; Spray and Walton, 2013; Walton et al., 2010).

4.3 The volatile inventory of Tissint shock melt glass

SIMS analysis detected minor amounts of fluorine, chlorine, phosphorus, and water. While present in minor amounts, these elements are not present in sufficient abundance to indicate incorporation of a significant sulfate or phosphate component. Major, minor and trace elements demonstrate a minor incorporation of phosphate (merrillite), and no evidence for significant incorporation of jarosite from the Martian surface.

Water is present within shock melt pockets in variable amounts. Similarly to major and minor elements, the abundance of water varies between shock melt pockets, and even within a single melt pocket. Water content ranges from relatively dry, <100 ppm for the driest glass spot analyzed, to >2500 ppm for the wettest.

The bulk of the Tissint meteorite is composed of nominally anhydrous minerals (NAM) dominated by pyroxene, olivine, and plagioclase (now maskelynite). Water contents for these minerals in Tissint were estimated by Chen et al. (2015) to be 0 ppm for olivine, 0-100 ppm for plagioclase, and 500-600 ppm for pyroxene, with an average for Tissint NAMs to be 200 ppm H_2O. Thus, water contents within Tissint shock melt pockets are much higher than in the igneous proportion of the rock. To explain the elevated water content within Tissint shock melt pockets, the presence of a hydrous phase is required, and this component must be preferentially incorporated into the shock melted proportion of the rock. Significant contribution of water to shock melt pockets by preferential melting of hydrous igneous minerals is unlikely: the only nominally hydrous mineral present within the meteorite is apatite, and only in trace amounts (Chennaoui Aoudjehane et al., 2012). The only phosphate phase documented here is merrillite, which is nominally anhydrous.

Within all shock melt pockets analyzed, chlorine is correlated with water, suggesting that chlorine followed water when originally introduced to the rock. This positive correlation with water is not observed for fluorine, sulfur, or phosphorus (Figure 11). Igneous apatite may be ruled out as the main source of the water within the shock melt pockets, as there would be a positive correlation of phosphorus with the volatile components F, Cl, and H_2O. Instead, the water and chlorine in Tissint shock melt pockets is most likely a remnant geochemical fingerprint of aqueous or alteration processes on Mars. This is a secondary signature that overprints the igneous chemistry

of the rock; this signature is most likely derived from processes affecting the rock in the Martian near-surface after the rock's igneous crystallization but prior to the ejection event.

Ion probe analyses on glass demonstrate that δD values in Tissint shock-produced glass plot along a negatively-sloping line when plotted against $1/H_2O$. This negatively-sloping trend most likely represents a mixing line between two isotopic reservoirs. The water-poor, low-δD reservoir (0 ‰ δD, 148 ppm H_2O) is likely derived from the igneous mineralogy of the rock, which inherited an isotopic signature that reflects the Martian mantle, δD ≤ 275 ‰ and ≤ 250 ppm H_2O (Leshin et al., 1996; Usui et al., 2012; McCubbin et al., 2012). The second hydrogen reservoir is near-surface water with an elevated δD of 6924 ‰. While such high δD values >2000 ‰ would be unusual for terrestrial sources, they are consistent with sources of water from the Martian surface and atmosphere. (Greenwood et al., 2008; Hu et al., 2014). Measurements made on Mars by the Curiosity Rover suggest that Martian surface and atmospheric waters have δD values in excess of 5000 ‰, and that water near the poles of the planet may have δD values as high as 7000 ‰ (Webster et al., 2013; Villanueva et al., 2014).

Two data points plot above the δD value vs. $1/H_2O$ line. The context for these points is important: these two points were collected from shock melt glass in close proximity to a large vesicle; furthermore, they are correlated with a lower abundance of water within this specific melt pocket. Glass becomes drier and enriched in the heavier isotope as the large vesicle is approached (Figure 13), likely a consequence of devolatilizing water into the vesicle while the shock melt pocket was molten. It has been demonstrated experimentally that impact-induced devolatilization will cause the fractionation of hydrogen isotopes, in which hydrogen is preferentially partitioned into the released gas (Tyburczy et al., 2001). This mechanism is likely responsible for the trend observed in the shock melt pocket highlighted in Figure 13.

High δD values also rule out significant terrestrial weathering. For all data collected, no data plot below the line towards the origin of the graph (water-rich, low δD). Any terrestrial alteration (for example, by dew percolating into cracks) would spread data towards a low δD and low $1/H_2O$. Tissint demonstrates an absence of terrestrial weathering, and the volatile signature preserved within the shock melt glass is Martian, not terrestrial.

4.4 Insights into crystallization of shock melt pockets

In shock melt pockets and veins, a coarsening progression is observed with the finest grains (or glass) at the margins and the coarsest crystals near the center. This is consistent with the interpretation the shock melt pockets cooled outside-in by conducting heat to the colder host rock (Walton and Herd, 2007; Shaw and Walton, 2013). As a consequence, the center of the melt features stayed molten longer and cooled more slowly, which allowed for the nucleation and growth of larger crystallites. The exception to this crystallization trend occurs when vesicles are present within the shock melt pocket. In those shock melt pockets that contain vesicles, the vesicles are enveloped by homogeneous or schlieren-rich glass, indicating that these regions cooled more rapidly than those areas lacking vesicles. Even in relatively large shock melt pockets, those areas near vesicles cooled very rapidly, more rapidly than would be explained by conduction to the colder host rock. For a large region of shock melt in Tissint MET11640/2-2-1/TEP (Figure 2), the largest crystallites are found within the interior of the region of shock melt, distal to both vesicles and the borders of the shock melt pocket with the surrounding host rock (Figure 13).

Shock melt pockets that contain lithic fragments entrained from the host rock often show some minor growth along the borders of the clast. When mineral fragments are incorporated into a melt pocket but they themselves are not entirely melted, those extant crystals act as nucleation sites and allow for the nucleation and growth of crystals to form from the shock melt. These are

usually seen as microscopic euhedral crystals (which may be zoned from a magnesium-rich core to an iron-rich rim) or as skeletal or dendritic crystals that radiate outwards from the central clast.

All of these observations are consistent with the formation of shock melt pockets *in situ* from void collapse or shock impedance contrasts, with cooling by conduction of heat to the colder host rock. The crystallization front moves from the outside-in as cooling is prolonged by excess heat left over from the formation of the shock melt pocket.

4.5 Shock-induced formation of high-pressure phases

Transformation of plagioclase to maskelynite is common in heavily-shocked meteorites, including the majority of Martian meteorites (Rubin, 2015). The high-pressure phases present in Tissint (ahrensite, ringwoodite, maskelynite, tissintite, stishovite, and amorphized bridgmanite + magnesiowüstite) formed by solid-state transformation of precursor igneous minerals or by crystallization from impact melt (Walton, 2013). These phases record shock pressures >19 GPa but < 30 GPa (Walton et al., 2013). The association between high-pressure phases and shock melt pockets is common. Ringwoodite is typically observed as lamellae within olivine that is adjacent to a shock melt pocket (Figure 4); evidence for olivine-to-ringwoodite transition was not observed within Tissint in igneous olivine distal to shock melt pockets. The reason for this may be that despite the high pressures present during the passing of the shock wave, the additional heat from the shock melt pockets was required to overcome the energy barrier to allow for the solid-state transformation from olivine to ringwoodite and ahrensite (Walton et al., 2014). However, it is also noted that much of the "ringwoodite" (high-density lamellae in olivine) does not exhibit characteristic Raman peaks for ringwoodite (peaks near 798 and 844 cm^{-1}), but rather exhibits a spectrum that is typical of olivine with peak positions near 820 and 850 cm^{-1}. This may be due to

a back-transformation of ringwoodite to olivine, accommodated by the leftover energy from the heat remaining in the shock melt pocket following the passing of the shock wave.

Tissintite is observed within the center of maskelynite clasts entrained within shock melt pockets, and within maskelynite along the margins of shock melts. The same mechanisms may apply with tissintite as they do with olivine polymorphs: high heat from the shock event is required to overcome the activation energy required to make the transition to the high-pressure form. The pressure required for phase transformation is temperature-dependent: at elevated temperatures, transformation of plagioclase to high-pressure phases such as maskelynite, jadeite, and garnet may proceed at lower pressures (Kubo et al., 2009). Similar to jadeite formation, transformation of maskelynite to tissintite is facilitated by high post-shock temperatures: the hotter portion of the grain in direct contact with the shock melt transformed to tissintite (Figure 4d). Excess waste heat leftover from the shock event may allow for the back-transition back to maskelynite: the exterior of the clasts within shock melt pockets may have back-transformed to maskelynite, while the center of the clasts were somewhat insulated from the high post-shock heat (Figure 4c). In either case, crystallization must have been rapid, at high pressures, before the pressures generated from the propagating shock wave had completely dissipated.

4.6 Thermal histories of shock melt pockets and volatile preservation potential

The HEAT models demonstrate that shock melt pockets cool from the outside-in, radiating heat away from the hot shock melt pockets and veins, and into the colder host rock. The solidification front moves from the periphery to the center of shock melt pockets and veins; this is in good agreement with the crystal coarsening trends observed texturally in BSE images. Shock melt pockets that contain larger skeletal or dendritic crystals, rather than quenched to glass, correspond to those regions within the thermal model that were cooled the slowest. The cooling

rate of individual shock melt pockets is affected by the size of the shock melt pocket, its geometry, its proximity to other shock melt pockets, and by the presence or absence of vesicles.

Those shock melt pockets that contain vesicles cool very rapidly, which is in agreement with the observation of quenched glass surrounding vesicles as seen in BSE images. In MET11640/2-2-1/TEP, the largest region of shock melt near the center of the section quickly quenches around the large vesicle in the center of the sample, then cools relatively slowly as the heat from the surrounding melt is radiated away. The large shock melt region in the center of the section that exhibits the largest skeletal and dendritic olivine and pyroxene crystals. In the center of this section, there are no extant high-pressure phases; any high-pressure phases that may have crystallized at high-pressures were either melted by the heat generated by the shockwave passing, or were allowed to back-transform to low-pressure phases.

Longer cooler times may have altered or destroyed a signal characteristic of the Martian near surface. Those areas that contain glass were quenched quickly, and have the best chance to preserve a geochemical signature without significant overprinting or alteration. For large melt pockets with vesicles, or vesiculated pockets near larger pockets: large volumes of melt will delay cooling; delay may keep melt hot enough long enough to allow diffusion/devolatilization to vesicles, altering the volatile signature.

5. Conclusions

Shock-produced melt in Tissint, a recent Martian meteorite fall, have been investigated using an array of advanced analytical techniques with the purpose of identifying Martian alteration products associated with these features. Data from EPMA and LA ICP-MS analyses suggests that there has not been any appreciable incorporation of a near-surface component (soil, jarosite, etc.). The shock melt pocket volatile inventory measured by SIMS indicates that Tissint contains

evidence that a component derived from the Martian near-surface has been trapped within the meteorite. The evidence for a Martian surface signature is present in very minor amounts, and is only detectable by sensitive techniques. EPMA is insufficient to quantify this signature; *in situ* mass spectrometry is required to quantify volatile components at the ppm level.

Hydrogen isotopes demonstrated that Tissint lacks an absence of significant terrestrial contamination. Water content is variable by up to hundreds of ppm within the same shock melt pocket. Water in Tissint melt pockets represents mixing from two H isotope reservoirs, a relatively dry, low-δD mantle reservoir, and a high-δD surface water reservoir.

Some shock melt pockets in Tissint contain a geochemical signature characteristic of Martian alteration products, seen primarily in water and chlorine concentrations and altered sulfides. The distribution of such melt pockets is likely heterogeneous within the host rock as cracks and voids that hosted these alteration products preferentially melted as the shockwave passed through the rock, inducing void collapse. A number of additional mechanisms other than void collapse are involved in the formation of shock melts, and as such, any near-surface materials may be heterogeneously trapped. The initial distribution of Martian weathering products in the pre-shocked rock is also presumably heterogeneous, contributing to the heterogeneous distribution of incorporated surface components therein. Hematite in Tissint is associated with shock melt pockets as an alteration product of pyrrhotite in a hot, locally-oxidized environment. Preliminary identification of hematite may aid in determining which shock melt pockets may have a geochemical signature indicative of incorporation of Martian near-surface weathering products. As shock melt glass is pervasive, first identification of hematite should prove useful for prioritizing regions for studies searching for Martian near-surface components in shergottites. Furthermore this hematite signature may be detected using a readily available, rapid and non-destructive technique such as Raman spectroscopy, which is desirable when analyzing rare and valuable

materials. Shock melt pockets that contain hematite should be considered as targets for analyses searching for geochemical signatures of near-surface components.

The chemical signature of the volatile component is sensitive, and may be altered or destroyed during prolonged cooling as a result of excess heat that lingers after the generation of shock melt. Additionally, if bubbles were present, the melt may partially devolatilized before the volatiles may be locked into the rock. Ideally, the volatile signature would be best preserved within an isolated, quickly-cooled glassy shock melt pocket free of vesicles.

A mechanism for preserving Martian near-surface materials within meteorites is proposed: A rock emplaced near the Martian surface develops open fractures or cracks. The rock is then subjected to secondary alteration while on Mars, as material derived from the Martian near-surface interacts with the rock and imparts a minor volatile-bearing signature, concentrated within fractures. A hypervelocity impact on Mars (presumably the ejection event) causes a shockwave to pass through the rock, inducing shock-metamorphism, including formation of high-pressure phases and generation of shock melt pockets and veins, including via void collapse. Energy released by void collapse generates head, locally melting portions of the rock; the volatile-bearing material is incorporated into the melt. Ideally, this volatile-bearing shock melt will be quenched to glass, vesicle-free, and isolated from the influence of nearby shock melt pockets or veins. If the region of shock melt is overly large, subjected to the heat conducted from nearby shock melt features, or vesiculated, the volatile signature may be altered or destroyed. After ejection from Mars and traversing to Earth, the meteorite is witnessed as a fireball, falls into a hot desert, and is not subjected to terrestrial precipitation prior to collection. Careful collection techniques, curation, and dry processing are preferred, as to minimize terrestrial contamination.

Works Cited

Avril, C., Malavergne, V., Caracas, R., Zanda, B., Reynard, B., Charon, E., Bobociou, E., Brunet, F., Borensztajn, S., Pont, Sylvain, Tarrida, M., & Guyot, F. (2013). Raman spectroscopic properties and Raman identification of CaS-MgS-MnS-FeS-Cr (sub 2) FeS (sub 4) sulfides in meteorites and reduced sulfur-rich systems. *Meteoritics & Planetary Science*, *48*(8), 1415-1426.

Balta, J. B., Sanborn, M. E., Udry, A., Wadhwa, M., & McSween, H. J. (2015). Petrology and trace element geochemistry of Tissint, the newest shergottite fall. *Meteoritics & Planetary Science*, *50*(1), 63-85.

Barrat, J. A., Gillet, P., Lesourd, M., Blichert-Toft, J., & Poupeau, G. R. (1999). The Tatahouine diogenite; mineralogical chemical effects of sixty-three years of terrestrial residence. *Meteoritics & Planetary Science*, *34*(1), 91-97.

Barrat, J.A., Jambon, A., Ferrière, L., Bollinger, C., Langlade, J.A., Liorzou, C., Boudouma, O., & Fialin, M. (2014). No Martian soil component in shergottite meteorites. *Geochimica et Cosmochimica Acta, 125,* 23-33.

Bischoff, A., and Stöffler, D. (1992). Shock metamorphism as a fundamental process in the evolution of planetary bodies: Information from meteorites. *European Journal of Mineralogy, 4,* 707-755.

Brennecka, G. A., Borg, L. E., & Wadhwa, M. (2014). Insights into the Martian mantle; the age and isotopics of the meteorite fall Tissint. *Meteoritics & Planetary Science*, *49*(3), 412-418.

Chen, M., & El Goresy, A. (2000). "The nature of maskelynite in shocked meteorites; not diaplectic glass but a glass quenched from shock-induced dense melt at high pressures." *Earth And Planetary Science Letters* 179, no. 3-4: 489-502.

Chen, M., Chen, J., Xie, X., & Xu, J. (2007). A microstructural investigation of natural lamellar ringwoodite in olivine of the shocked Sixiangkou chondrite. *Earth And Planetary Science Letters*, *264*(1-2), 277-283.

Chen, Y., Liu, Y., Guan, Y., Eiler, J. M., Ma, C., Rossman, G. R., & Taylor, L. A. (2015). Evidence in Tissint for recent subsurface water on Mars. *Earth And Planetary Science Letters*, *425*55-63.

Chennaoui Aoudjehane, H., Avice, G., Barrat, J. A., Boudouma, O., Chen, G., Duke, M. J. M., Franchi, I. A., Gattacceca, J., Grady, M. M., Greenwood, R. C., Herd, C. D. K., Hewins, R., Jambon, A., Marty, B., Rochette, P., Smith, C. L., Sautter, V., Verchovsky, A., Weber, P., & Zanda, B. (2012). Tissint Martian Meteorite: A Fresh Look at the Interior, Surface, and Atmosphere of Mars. *Science, 338*(6108), 785-788.

Crozaz, G., & Wadhwa, M. (2001). The terrestrial alteration of Saharan shergottites Dar al Gani 476 and 489; a case study of weathering in a hot desert environment. *Geochimica Et Cosmochimica Acta*, *65*(6), 971-977.

Crozaz, G., Floss, C., & Wadhwa, M. (2003). Chemical alteration and REE mobilization in meteorites from hot and cold deserts. *Geochimica Et Cosmochimica Acta*, *67*(24), 4727-4741.

Dekkers, M. J. (1990). Magnetic monitoring of pyrrhotite alteration during thermal demagnetization. *Geophysical Research Letters*,*17*(6), 779-782.

Feldman, V. I. (1994). The conditions of shock metamorphism. *Special Paper - Geological Society Of America*, *293*121-132.

Franchi, I. A., Wright, I. P., Sexton, A. S., & Pillinger, C. T. (1999). The oxygen-isotopic composition of Earth and Mars. *Meteoritics & Planetary Science 34*, 657-661.

Fritz, J., Artemieva, N., & Greshake, A. (2005). Ejection of Martian meteorites. *Meteoritics & Planetary Science*, *40*(9-10), 1393-1411.

Greenwood, J. P., Itoh, S., Sakamoto, N., Vicenzi, E. P., & Yurimoto, H. (2008). Hydrogen isotope evidence for loss of water from Mars through time. *Geophysical Research Letters*, *35*(5), CitationL05203. doi:10.1029/2007GL0327.

Greshake, A., Fritz, J., Boettger, U., & Goran, D. (2013). Shear-induced ringwoodite formation in the Martian shergottite Dar al Gani 670. *Earth and Planetary Science Letters 375,* 383-394.

Hu, J., Sharp, T. G., & Walton, E. L. (2013). Shock Effects in Tissint II: Olivine Transformation to Silicate Perovskite and Oxide. *Lunar and Planetary Science XLIV, Houston, Lunar. Planet. Inst, Abstract #1041.*

Hu, S., Lin, Y., Zhang, J., Hao, J., Feng, L., Xu, L., Wang, W., & Yang, J. (2014). NanoSIMS analyses of apatite and melt inclusions in the GRV 020090 Martian meteorite; hydrogen isotope evidence for recent past underground hydrothermal activity on Mars. *Geochimica Et Cosmochimica Acta*, *140,* 321-333.

Irving, A. J., Kuehner, S. M., Tanaka, R., Herd, C. D. K., Chen, G., & Lapen, T. J. (2012). The Tissint depleted permafic olivine-phyric shergottite; petrologic, elemental and isotopic characterization of a recent fall in Morocco. *Lunar and Planetary Science XLIII, Houston, Lunar. Planet. Inst, Abstract #2510.*

Kieffer, S. W. & Simonds, C. H. (1980). The Role of Volatiles and Lithology in the Impact Cratering Process. *Reviews of Geophysics and Space Physics, 18*(1), 143-181.

Kubo, T., Kimura, M., Kato, T., Nishi, M., Tominaga, A., Kikegawa, T., & Funakoshi, K. (2010). Plagioclase breakdown as an indicator for shock conditions of meteorites. *Nature Geoscience*, *3*(1), 41-45.

Lafuente, B., Downs, R. T., Yang, H., & Stone, N. (2015). The power of databases: the RRUFF project. *Highlights in Mineralogical Crystallography*, eds. Armbruster, T., & Danisi, R. M. Berlin, Germany, W. De Gruyter, pp 1-30

Leshin, L. A., Epstein, S., & Stolper, E. M. (1996). Hydrogen isotope geochemistry of SNC meteorites. *Geochimica Et Cosmochimica Acta*, *60*(14), 2635-2650.

Ma, C., Tschauner, O., Liu, Y., Beckett, J.R., Rossman, G.R., Zuravlev, K., Prakapenka, V., Dera, P., Sinogeikin, S., Smith, J., & Taylor, L.A., 2014. Discovery of ahrensite γ -Fe_2SiO_4 and tissintite (Ca, Na,)$AlSi_2O_6$: two new high pressure minerals from the Tissint Martian meteorite. *Lunar and Planetary Science XLV, Houston, Lunar. Planet. Inst, Abstract #1222.*

Ma, C., Tschauner, O., Beckett, J. R., Liu, Y., Rossman, G. R., Zhuravlev, K., Prakapenka, V., Dera, P., & Taylor, L. A. (2015). Tissintite, (Ca,Na,)$AlSi_2O_6$, a highly-defective, shock-induced, high-pressure clinopyroxene in the Tissint martian meteorite. *Earth And Planetary Science Letters*, *422,* 194-205.

McCubbin, F. M., Hauri, E. H., Elardo, S. M., Vander Kaaden, K. E., Wang, J., & Shearer, C. J. (2012). Hydrous melting of the Martian mantle produced both depleted and enriched shergottites. *Geology (Boulder)*, *40*(8), 683-686.

Melosh, H. J. (1985). Ejection of rock fragments from planetary bodies. *Geology (Boulder), 13*(2), 144-148.

Mernagh, T. P., & Trudu, A. G. (1993). A laser Raman microprobe study of some geologically important sulphide minerals. *Chemical Geology*,*103*(1-4), 113-127.

Miyahara, M., Ohtani, E., Kimura, M., El Goresy, A., Ozawa, S., Nagase, T., Nishijima, M., & Hiraga, K. (2010). Coherent and subsequent incoherent ringwoodite growth in olivine of shocked L6 chondrites. *Earth And Planetary Science Letters*, *295*(1-2), 321-327.

Miyahara, M., Ohtani, E., Ozawa, S., Kimura, M., El Goresy, A., Sakai, T., Nagase, T., Hiraga, K., Hirao, N., & Ohishi, Y. (2011). Natural dissociation of olivine to (Mg,Fe)SiO_3 perovskite and magnesiowustite in a shocked Martian meteorite. *Proceedings Of The National Academy Of Sciences Of The United States Of America*, *108*(15), 5999-6003.

Nyquist L. E., Bogard D. D., Shih C. Y., Greshake A., Stöffler D., & Eugster O. (2001). Ages and histories of Martian meteorites. *Chronology and Evolution of Mars 96*, 105–164.

Palme, H., Lodders, K., & Jones, A. (2014). Solar system abundances of the elements. In: Holland, H.D., Turekian, K.K. (Eds.), *Treatise on Geochemistry, vol. 2. Second edition*. Elsevier, Oxford, pp. 15–36.

Potts, P. J. (1992) *A Handbook of Silicate Rock Analysis*, 622 p. Springer, New York.

Ross, D. K., Rao, M. N., Nyquist, L. E., Agee, C. B., & Sutton, S. (2013). Compositions of magmatic and impact melt sulfides in Tissint and EETA 79001; precursors of immiscible sulfide melt blebs in shergottite impact melts. *Lunar and Planetary Science XLIV, Houston, Lunar. Planet. Inst, Abstract #1715.*

Rubin, A. E. (2015). Maskelynite in basaltic meteorites; an indicator of shock pressure during impact ejection from parent bodies. *Lunar and Planetary Science XLVI, Houston, Lunar. Planet. Inst, Abstract #1047.*

Sharp, T. G., & DeCarli, P. S. (2006). Shock effects in meteorites. *Meteorites and the early solar system II*, 653-677.

Shaw, C. J., & Walton, E. (2013). Thermal modeling of shock melts in Martian meteorites; implications for preserving Martian atmospheric signatures and crystallization of high-pressure minerals from shock melts. *Meteoritics & Planetary Science*, *48*(5), 758-770.

Stöffler, D., Keil, K., & Scott, E. R. D. (1991). Shock metamorphism of ordinary chondrites. *Geochimica et Cosmochimica Acta, 55,* 3845-3867.

Sutton, S. R., Ross, D. K., Rao, M. N., & Nyquist, L. E. (2014). Identification of Martian regolith sulfur components in shergottites using sulfur K XANES and Fe/S ratios. *Lunar and Planetary Science XLV, Houston, Lunar. Planet. Inst, Abstract #1524.*

Treiman, A. H., Gleason, J. D., & Bogard, D. D. (2000). The SNC meteorites are from Mars. *Planetary and Space Science 48,* 1213-1230.

Tyburczy, J. A., Xu, X., Ahrens, T. J., & Epstein, S. (2001). Shock-induced devolatilization and isotopic fractionation of H and C from Murchison Meteorite; some implications for planetary accretion. *Earth And Planetary Science Letters*, *192*(1), 23-30.

Villanueva, G. L., Mumma, M. J., Novak, R. E., Kaeufl, H. U., Hartogh, P., Encrenaz, T., Tokunaga, A., Khayat, A., & Smith, M. D. (2015). Strong water isotopic anomalies in the Martian atmosphere; probing current and ancient reservoirs. *Science*, *348*(6231), 218-221.

Usui, T., Alexander, C. O., Wang, J., Simon, J. I., & Jones, J. H. (2012). Origin of water and mantle-crust interactions on Mars inferred from hydrogen isotopes and volatile element abundances of olivine-hosted melt inclusions of primitive shergottites. *Earth And Planetary Science Letters*, *357-358*119-129.

Walton, E. L., & Herd, C. D. K. (2007). Dynamic crystallization of shock melts in Allan Hills 77005: Implications for melt pocket formation in Martian meteorites. *Geochimica et Cosmochimica Acta 71,* 5267–5285.

Walton, E. L., Kelley, S. P., & Herd, C. K. (2007). A laser probe $^{40}Ar/^{39}Ar$ investigation of two Martian lherzolitic basaltic shergottites. *Meteoritics & Planetary Science*, *42, Supplement* A159.

Walton, E. L., Jugo, P. J., Herd, C. K., & Wilke, M. M. (2010). Martian regolith in Elephant Moraine 79001 shock melts?; evidence from major element composition and sulfur speciation. *Geochimica et Cosmochimica Acta*, *74*(16), 4829-4843.

Walton, E. L., Kelley, S. P., Herd, C. K., Irving, A. J., & Bunch, T. E. (2011). A laser probe $^{40}Ar/^{39}Ar$ investigation of shergottite Northwest Africa 4797; implications for shock metamorphism prior to ejection. *Meteoritics & Planetary Science*, *46, SUPPL.*A245.

Walton, E. L. (2013). Shock metamorphism of Elephant Moraine A79001: Implications for olivine–ringwoodite transformation and the complex thermal history of heavily shocked Martian meteorites. *Geochimica et Cosmochimica Acta 107*, 299–315.

Walton, E. L., Sharp, T. G., Hu, J., & Filiberto, J. (2014). Heterogeneous mineral assemblages in Martian meteorite Tissint as a result of a recent small impact event on Mars. *Geochimica Et Cosmochimica Acta*, *140*334-348.

Wang, A., Jolliff, B. L., & Haskin, L. A. (1999). Raman spectroscopic characterization of a Martian SNC meteorite; Zagami. *Journal Of Geophysical Research*, *104*(E4), 8509-8519.

Wang, A., Kuebler, K. E., Jolliff, B. L., & Haskin, L. A. (2004a). Raman spectroscopy of Fe-Ti-Cr-oxides, case study; Martian meteorite EETA79001. *American Mineralogist*, 89(5-6), 665-680.

Wang, A., Kuebler, K. E., Jolliff, B. L., & Haskin, L. A. (2004b). Mineralogy of a Martian meteorite as determined by Raman spectroscopy. *Journal of Raman Spectroscopy, 35,* 504-514.

Webster, C. R., Mahaffy, P. R., Leshin, L. A., Atreya, S. K., Flesch, G. J., Stern, J., Christenson, L. E., Vasavada, A. R., Owen, T., Niles, P. B., Jones, J. H., Franz, H., & MSL Science Team (2013). Mars atmospheric escape recorded by H, C and O isotope ratios in carbon dioxide and water measured by the SAM tunable laser spectrometer on the Curiosity Rover. *Lunar and Planetary Science XLIV, Houston, Lunar. Planet. Inst, Abstract #1365.*

Wohletz K., Civetta L., & Orsi G. (1999). Thermal evolution of the Phlegraean magmatic system. *Journal of Volcanology and Geothermal Research, 91*, 391–414.

Appendix

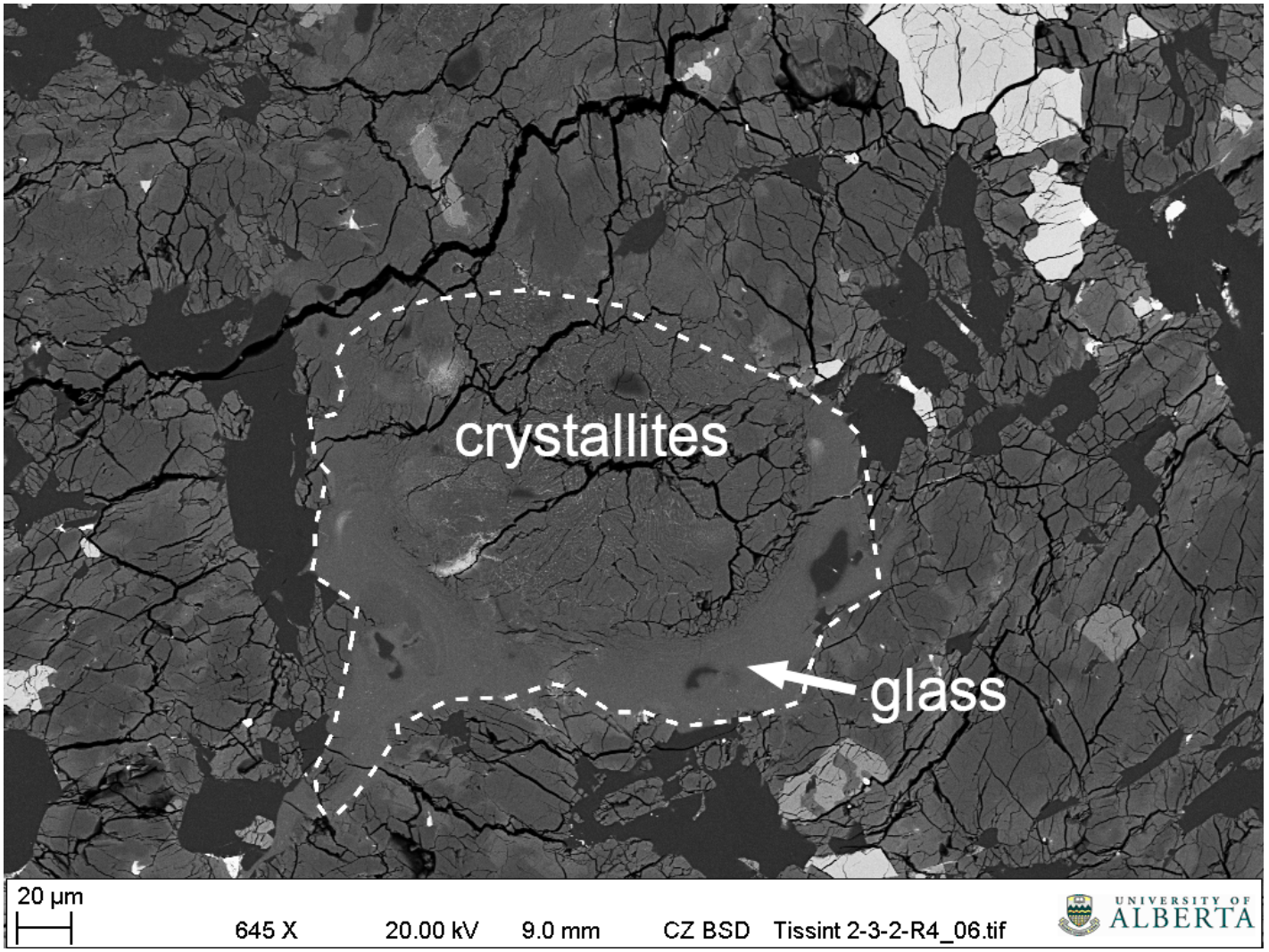

Figure A1: BSE image of a shock melt pocket in MET11640/2-3-2/TEP. The melt pocket is crystalline at its core, comprised primarily of crystallites of pyroxene. Glass is limited to the periphery of the melt pocket.

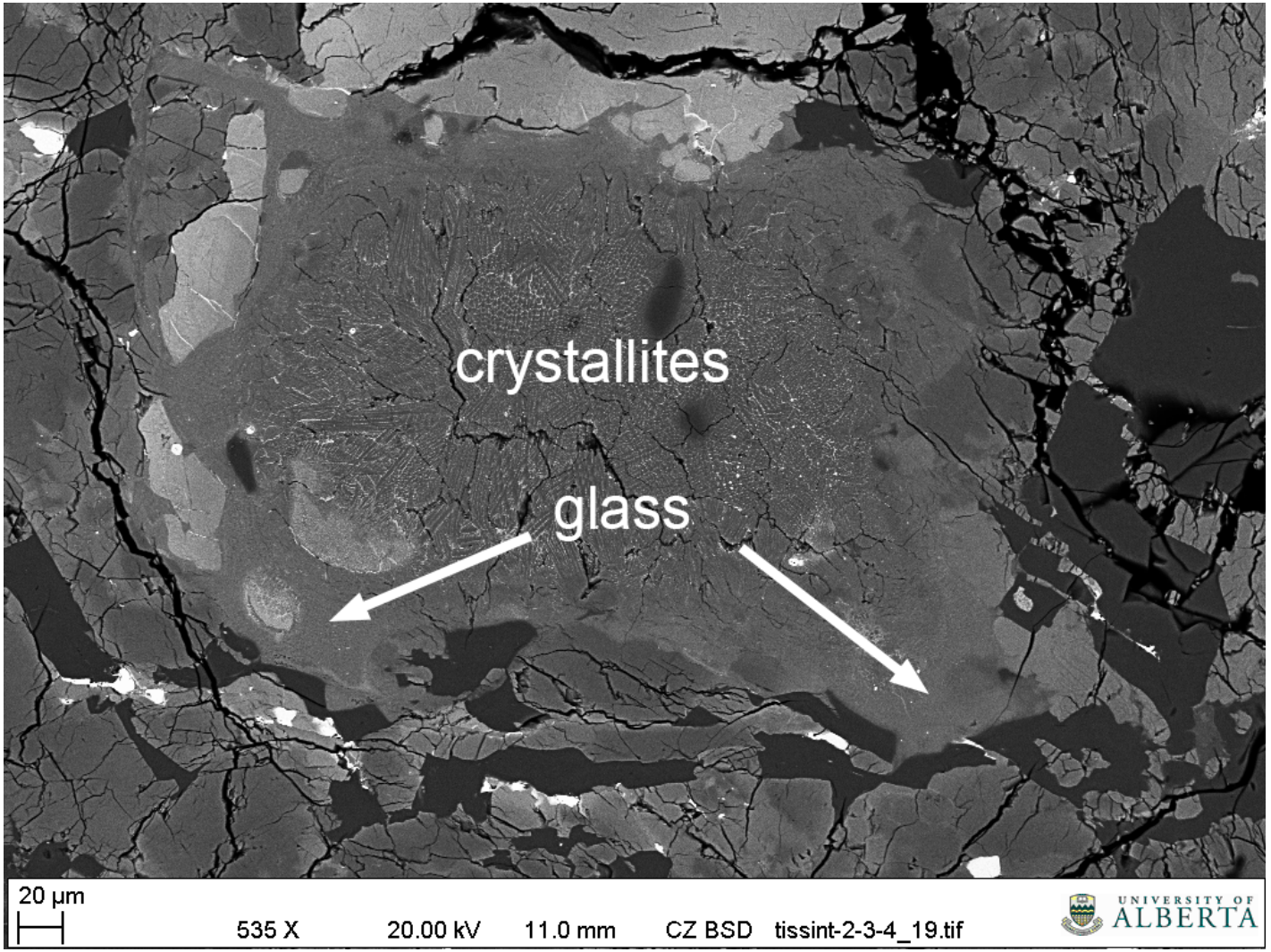

Figure A2: BSE image of a shock melt pocket in MET11640/2-3-4/TEP. Similar to Figure A1, the melt pocket is crystalline at its core, with glass along the periphery. Crystallinity increases from glass to coarse crystallites towards the center of the melt pocket.

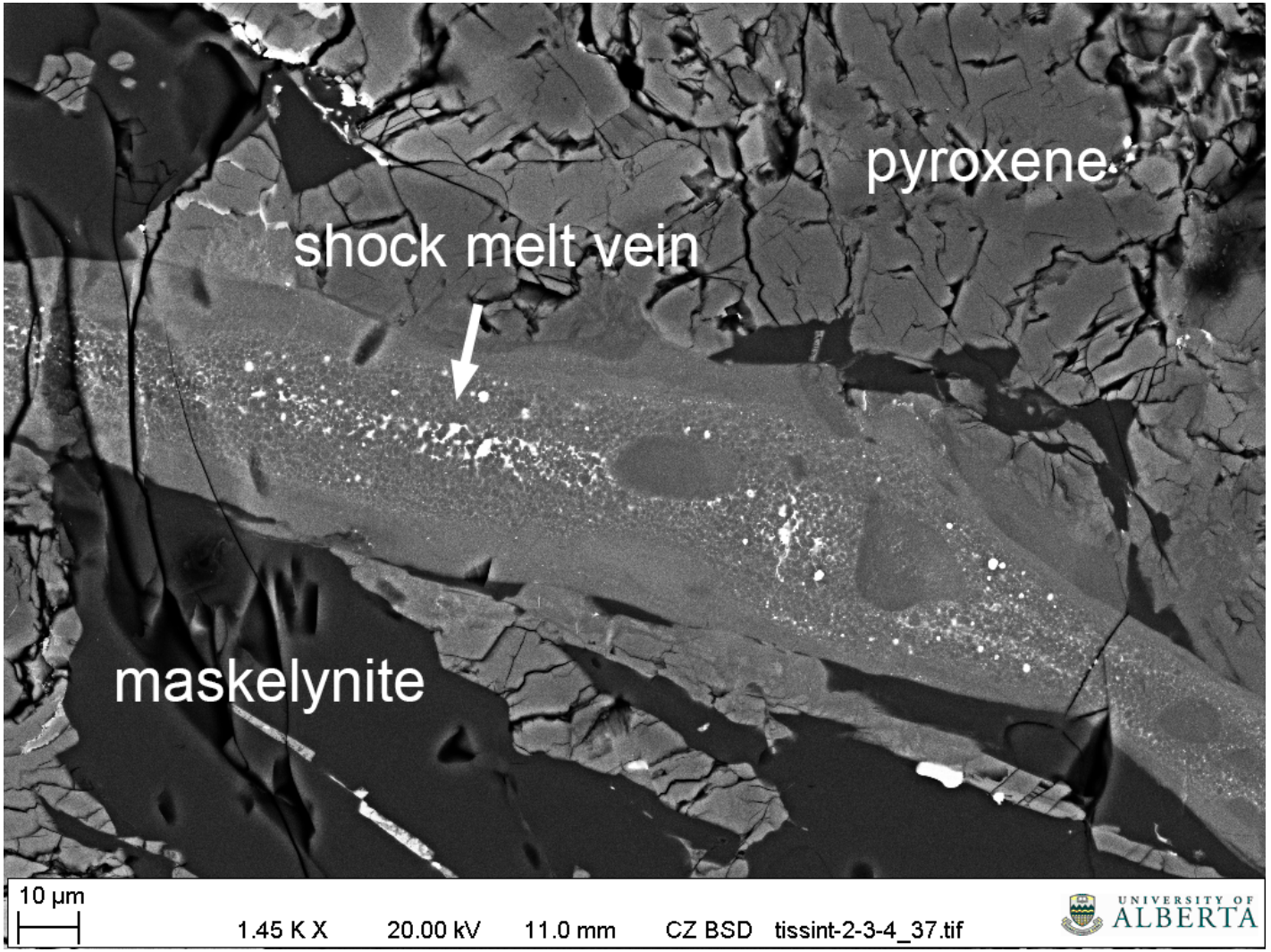

Figure A3. BSE image of a shock melt vein in MET11640/2-3-4/TEP. Similar to shock melt pockets, crystallinity increases towards the center of the vein.

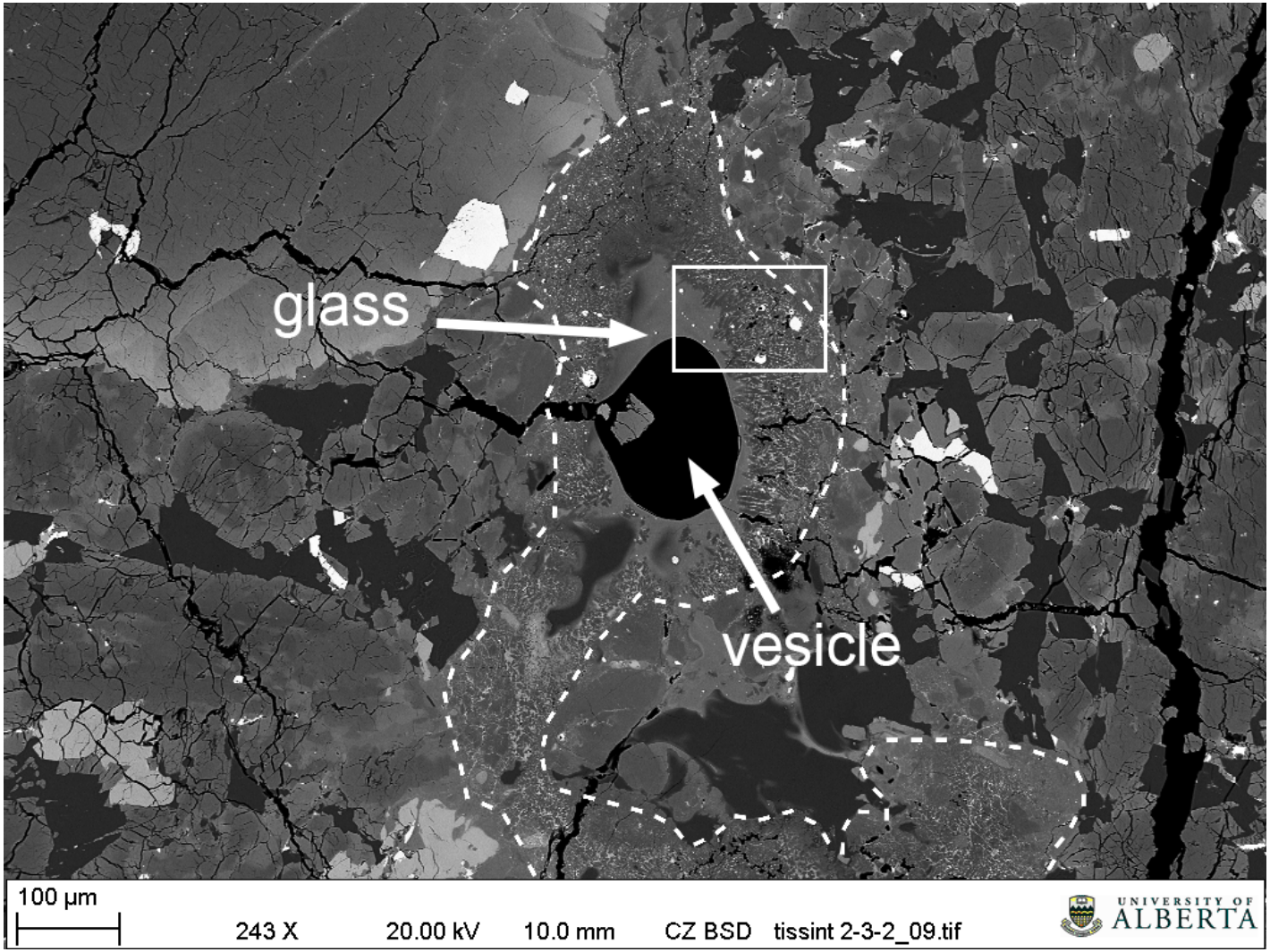

Figure A4: BSE image of a vesiculated shock melt pocket. The vesicle is enveloped by glass. The white box is the border of Figure A5.

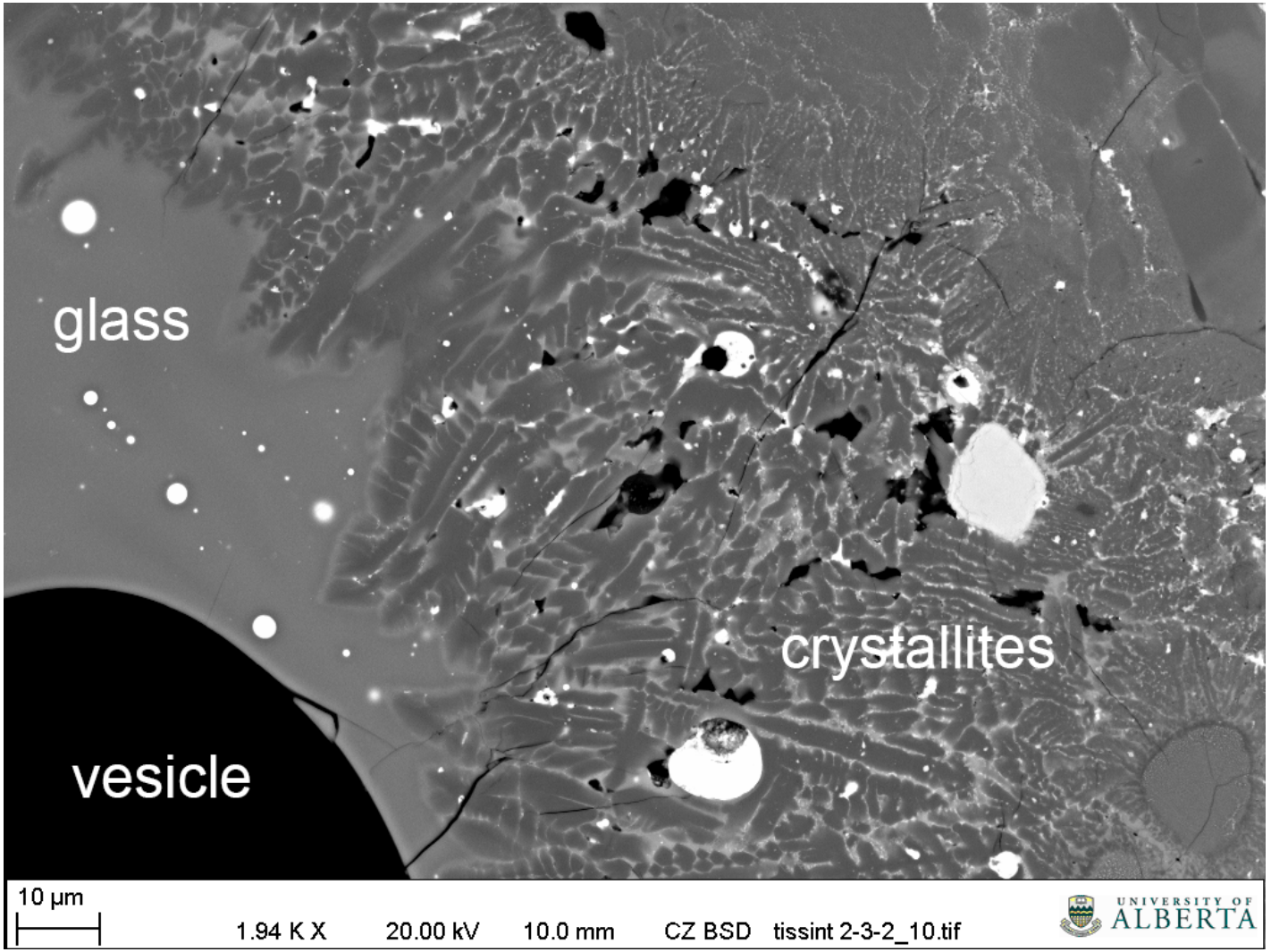

Figure A5: BSE image of glass and pyroxene crystallites within a shock melt pocket. Iron sulfide spherules are sporadically distributed amongst the crystallites and within the glass.

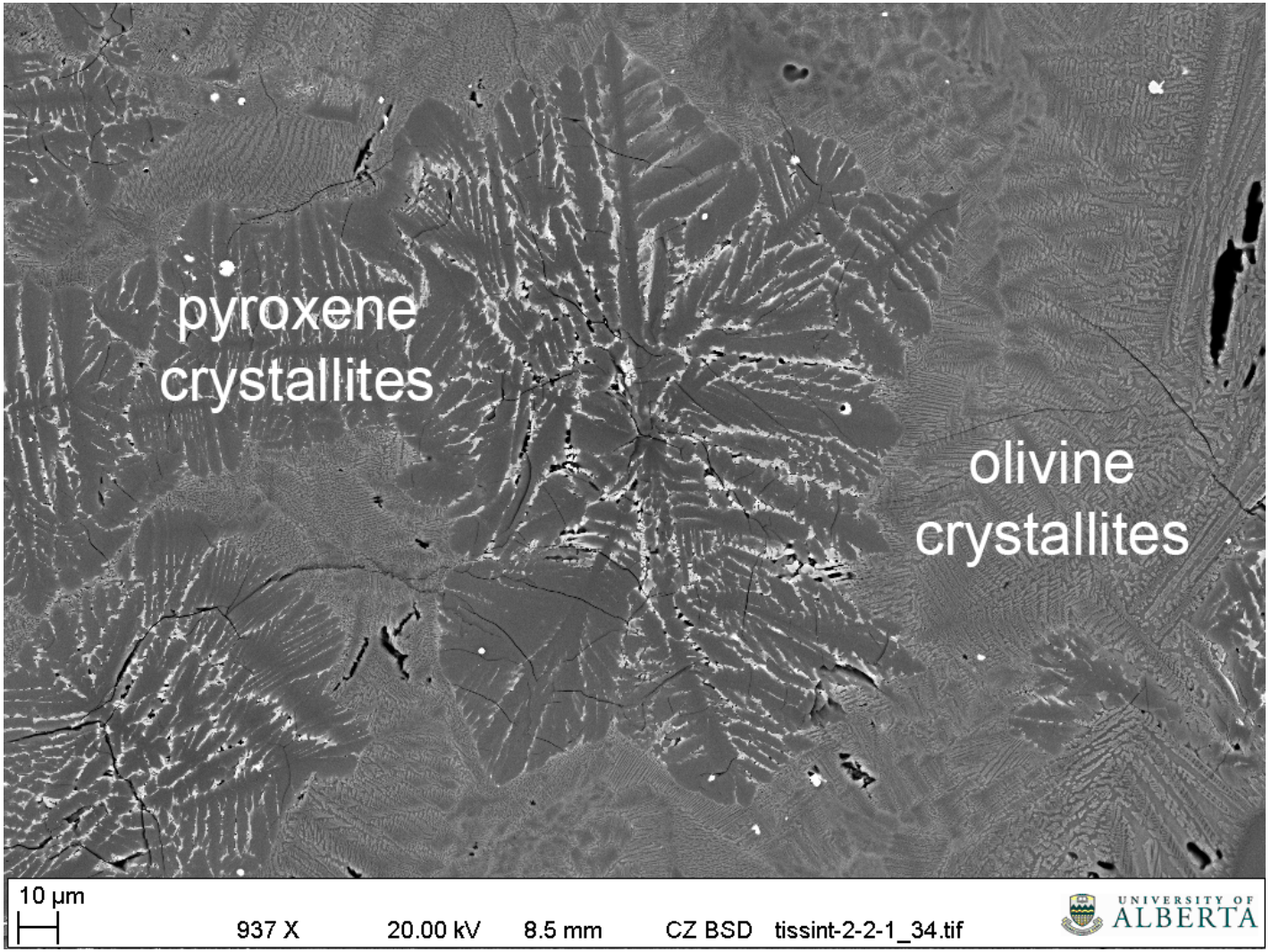

Figure A6: BSE image of feathery and skeletal crystallites of pyroxene and olivine within the center of a large shock melt pocket. This image corresponds to "Point C" in Figure 17.

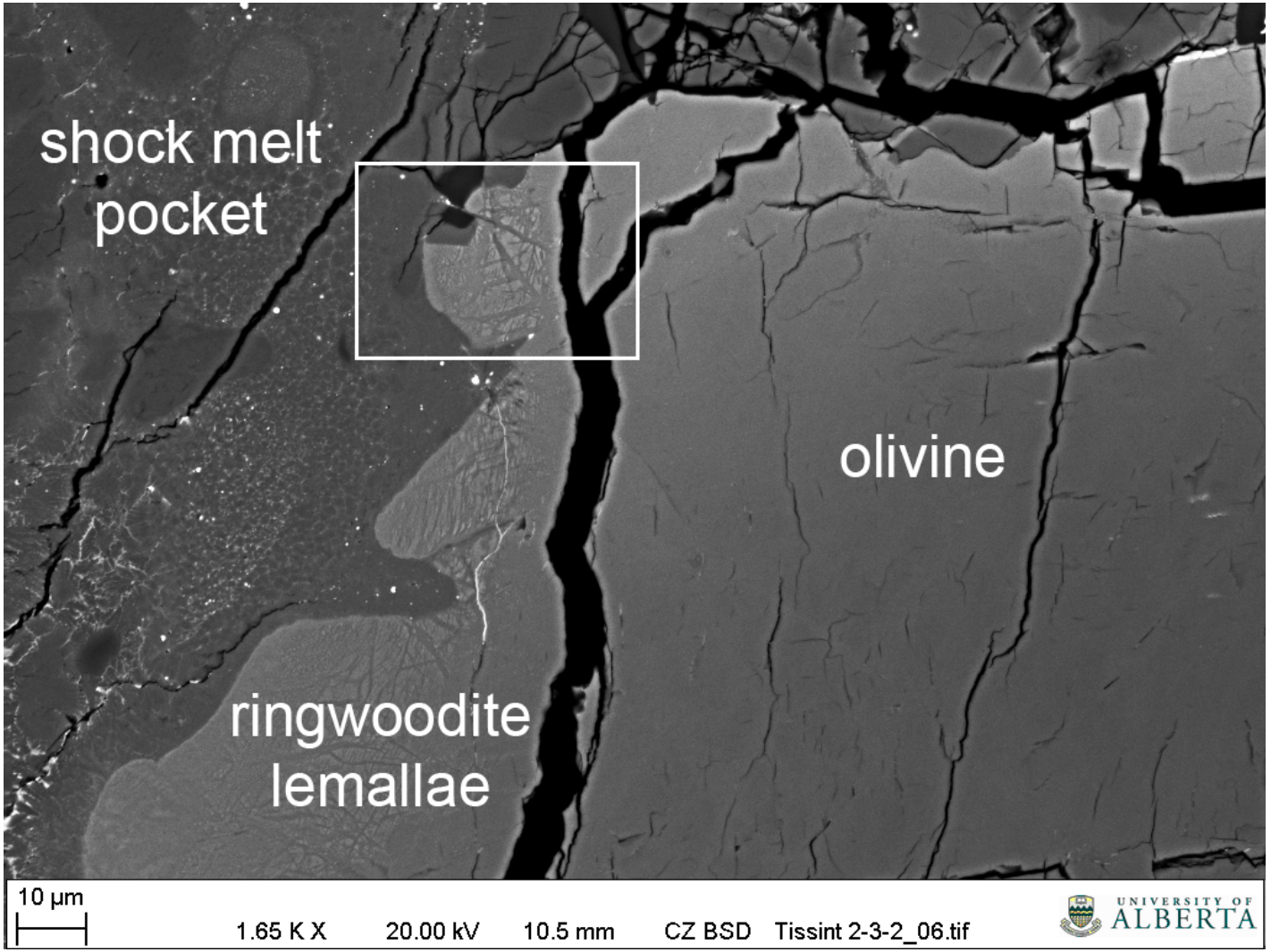

Figure A7: BSE image of an olivine macrocrysts in contact with a shock melt pocket. Where the olivine is proximal to the shock melt, abundant ringwoodite is present as, high-contrast (high density) lamellae. The white box is the border of Figure A8.

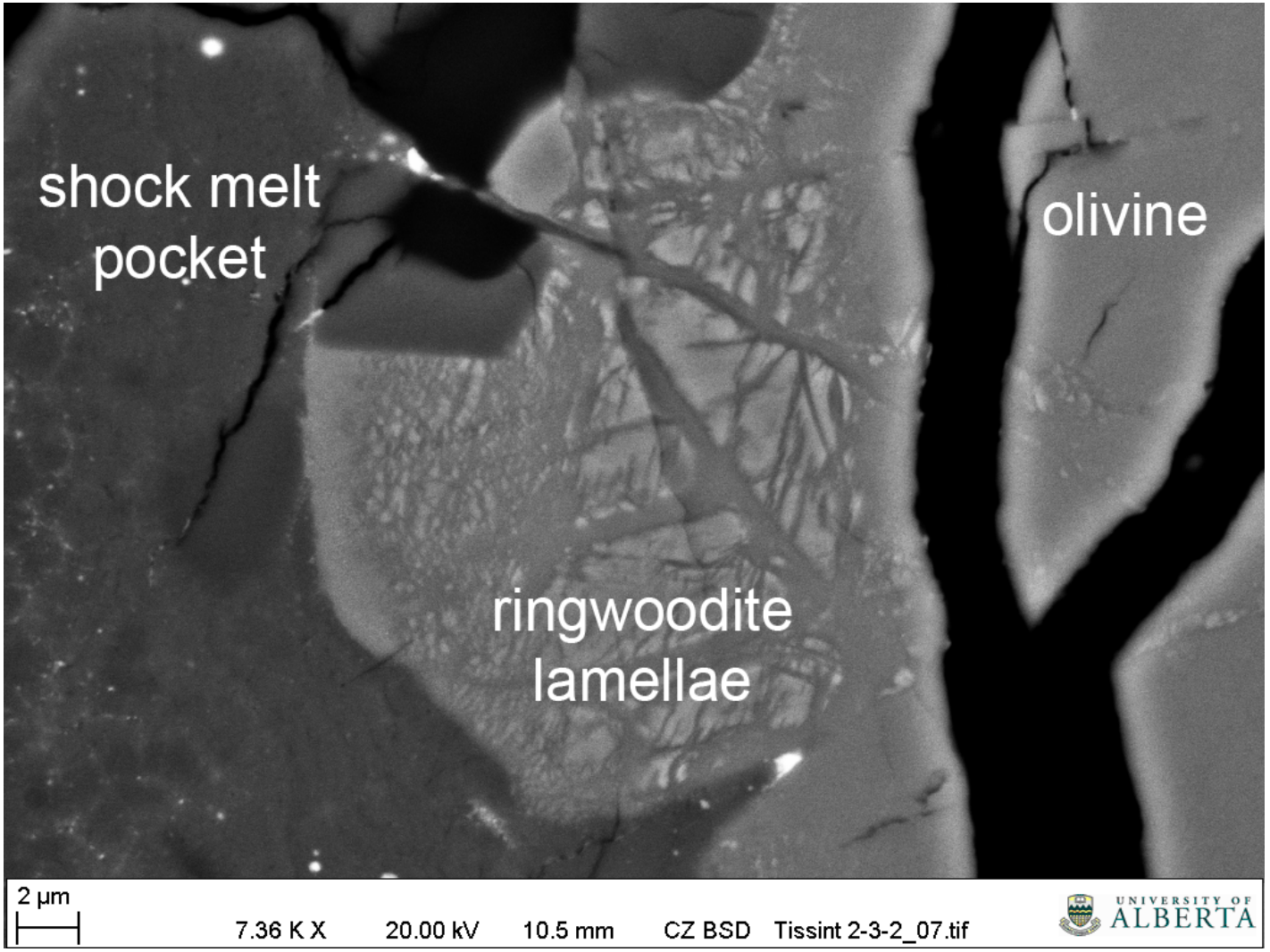

Figure A8. BSE image of high-density ringwoodite lamellae within olivine in contact with a shock melt pocket.

sample	SiO_2	TiO_2	Al_2O_3	Cr_2O_3	FeO	MnO	MgO	CaO	Na_2O	K_2O	P_2O_5	SO_3	Cl	Total
221-g1-1	48.70	0.42	3.74	0.89	20.05	0.58	18.86	7.18	0.50	0.03	0.26	0.51		101.72
221-g1-2	48.15	0.51	3.57	0.79	20.35	0.56	18.81	7.34	0.45	0.02	0.49	0.34	0.02	101.41
221-g1-3	47.85	0.45	4.25	0.72	20.62	0.57	18.47	7.30	0.47		0.24	0.31		101.25
221-g1-4	49.52	0.36	14.34	0.47	13.82	0.38	11.51	9.05	1.56	0.05	0.15	0.20		101.40
221-g1-5	49.91	0.36	14.82	0.37	13.16	0.35	10.72	9.10	1.54	0.03	0.29	0.15		100.81
221-g1-6	47.85	0.43	3.56	0.75	21.41	0.64	17.90	7.73	0.65	0.04	0.24	0.45		101.64
221-g1-7	48.41	0.44	3.83	0.81	20.42	0.54	18.78	7.24	0.52	0.03	0.21	0.38		101.59
221-g1-8	48.77	0.47	6.51	0.64	18.73	0.51	16.66	7.90	0.79	0.02	0.32	0.31		101.61
221-g1-9	48.88	0.47	11.78	0.49	15.38	0.43	12.06	9.68	1.23	0.04	0.52	0.11	0.02	101.10
221-g1-10	48.93	0.25	18.84	0.33	11.42	0.31	9.23	9.66	1.90	0.06	0.45	0.13		101.51
221-g1-11	48.89	0.48	5.39	0.76	19.38	0.49	17.37	7.80	0.35	0.02	0.29	0.37	0.02	101.60
221-g2-1	48.04	0.52	3.66	0.77	19.77	0.54	19.06	7.81	0.36		0.26	0.33		101.12
221-g2-2	48.34	0.45	3.51	0.67	21.33	0.56	17.54	7.95	0.39	0.03	0.29	0.23		101.29
LOD	0.02	0.03	0.02	0.03	0.03	0.03	0.02	0.04	0.02	0.02	0.03	0.04	0.02	

	SiO_2	TiO_2	Al_2O_3	Cr_2O_3	FeO	MnO	MgO	CaO	Na_2O	K_2O	P_2O_5	SO_3	NiO	Total
221-g3-1	47.59	0.50	3.75	0.87	20.38	0.55	18.78	6.70	0.27	0.02	0.34	0.42	0.05	100.17
221-g3-2	47.32	0.50	3.46	0.75	20.84	0.56	19.10	6.52	0.42	0.02	0.35	0.33	0.03	100.17
221-g3-3	47.78	0.45	4.59	0.75	19.81	0.52	17.91	6.97	0.49	0.02	0.35	0.38	0.05	100.02
221-g3-4	47.98	0.47	4.35	0.76	19.96	0.56	18.09	6.90	0.38	0.02	0.34	0.46	0.03	100.26
221-g3-5	48.36	0.47	3.87	0.84	19.98	0.54	18.50	6.75	0.20	0.01	0.31	0.33	0.04	100.16
221-g3-6	46.83	0.46	3.51	0.80	21.50	0.59	18.48	6.92	0.31	0.01	0.31	0.40	0.04	100.11
221-g3-7	47.94	0.46	3.84	0.74	20.31	0.57	17.98	7.01	0.33	0.03	0.26	0.43	0.04	99.89
221-g4-1	48.15	0.47	3.03	1.03	19.95	0.55	18.92	7.29	0.17	0.01	0.42	0.27	0.03	100.25
221-g4-2	49.38	0.46	2.56	0.65	19.94	0.57	18.83	7.10	0.13	0.01	0.18	0.15	0.04	99.96
221-g4-3	45.45	0.42	3.07	0.68	23.17	0.62	19.66	5.94	0.42	0.02	0.29	0.16	0.02	99.90
221-g4-4	47.82	0.45	3.19	0.91	20.70	0.61	18.63	6.94	0.32	0.02	0.26	0.22	0.04	100.07
221-g4-5	49.11	0.45	4.82	0.49	18.91	0.55	16.30	8.46	0.14	0.02	0.33	0.25	0.03	99.83
221-g5-1	48.33	0.45	3.59	0.75	20.23	0.57	18.27	7.04	0.21	0.02	0.26	0.45	0.02	100.16
221-g5-2	47.75	0.59	3.87	0.80	20.01	0.62	17.77	7.35	0.23	0.02	0.59	0.30		99.90
221-g5-3	48.84	0.42	3.48	0.71	20.79	0.58	16.56	7.58	0.21	0.01	0.26	0.39		99.83
221-g5-4	48.16	0.52	4.02	0.75	20.98	0.60	16.95	7.65	0.36	0.03	0.26	0.42	0.02	100.70
221-g5-5	48.54	0.47	3.50	0.79	19.85	0.57	18.18	7.21	0.34	0.03	0.32	0.41	0.04	100.20
221-g5-6	49.39	0.47	3.58	0.74	19.27	0.58	17.34	7.82	0.20	0.02	0.26	0.22		99.89
221-g5-7	49.09	0.47	4.00	0.67	19.92	0.57	16.25	8.17	0.19	0.01	0.34	0.24	0.02	99.92
221-g5-8	49.45	0.54	3.69	0.86	18.32	0.53	18.77	7.22	0.06		0.30	0.13		99.87

	SiO_2	TiO_2	Al_2O_3	Cr_2O_3	FeO	MnO	MgO	CaO	Na_2O	K_2O	P_2O_5	SO_3	NiO	Total
221-g5-9	48.47	0.39	3.42	0.76	20.03	0.59	17.14	7.68	0.24	0.01	0.21	0.26	0.02	99.21
221-g5-10	49.43	0.38	3.69	0.70	18.42	0.53	18.91	6.74	0.51	0.02	0.24	0.14	0.03	99.70
221-g6-1	51.55	0.41	2.66	0.51	18.00	0.63	17.18	8.37	0.34	0.03	0.32	0.28	0.02	100.28
221-g6-2	50.87	0.39	2.49	0.54	18.65	0.60	17.48	7.91	0.33	0.03	0.32	0.22	0.03	99.82
221-g6-3	51.75	0.43	2.56	0.51	17.53	0.62	17.34	8.22	0.30	0.02	0.30	0.19		99.78
LOD	0.02	0.03	0.02	0.04	0.03	0.03	0.03	0.01	0.02	0.01	0.02	0.04	0.02	

Table A1: EPMA results for shock melt glass in MET11640/2-2-1/TEP.

sample	SiO_2	TiO_2	Al_2O_3	Cr_2O_3	FeO	MnO	MgO	CaO	Na_2O	K_2O	P_2O_5	SO_3	Cl	Total
221-c1-1	47.77	0.50	3.77	0.82	21.29	0.58	18.23	7.36	0.40		0.27	0.49	0.02	101.51
221-c1-2	50.00	0.46	3.65	1.00	18.01	0.55	20.57	6.42	0.10		0.27	0.28	0.02	101.33
221-c1-3	46.78	0.54	3.63	0.79	23.34	0.62	17.66	7.51	0.27	0.02	0.26	0.51		101.92
221-c1-4	40.35	0.05	0.34	0.52	18.01	0.35	40.29	0.61	0.06		0.09	0.04		100.69
221-c1-5	50.17	0.37	3.42	0.79	18.46	0.54	20.18	7.01	0.41		0.21	0.43		101.98
221-c1-6	52.95	0.21	2.80	1.01	14.18	0.47	23.16	5.87	0.31		0.09	0.25		101.28
221-c1-7	50.43	0.45	3.57	0.95	18.18	0.50	20.83	6.30	0.13		0.30	0.25		101.89
221-c1-8	45.46	0.38	2.95	0.73	20.47	0.52	22.91	5.06	0.52		0.25	0.43	0.02	99.71
221-c2-1	47.96	0.49	3.57	0.68	20.62	0.59	18.75	7.93	0.41	0.02	0.23	0.29	0.03	101.57
221-c2-2	52.09	0.51	2.05	0.77	14.85	0.54	15.72	14.94	0.16		0.05	0.05		101.73
221-c2-3	49.19	0.38	3.38	0.78	19.60	0.56	19.04	7.91	0.44		0.22	0.26		101.76
221-c2-4	49.18	0.49	3.62	0.61	20.98	0.63	17.01	8.67	0.41	0.03	0.34	0.26		102.23
221-c2-5	49.98	0.58	3.49	0.71	19.35	0.58	17.68	8.88	0.41	0.02	0.18	0.25	0.03	102.14
221-c2-6	49.69	0.48	3.02	0.72	20.15	0.63	18.73	7.84	0.32	0.02	0.26	0.27		102.11
221-c2-7	49.80	0.40	6.89	0.62	17.36	0.54	16.49	9.12	0.45		0.24	0.08		101.98
221-c2-8	49.97	0.52	4.07	0.79	18.43	0.55	17.90	8.52	0.23		0.24	0.20		101.42
221-c2-9	49.99	0.49	3.90	0.78	18.80	0.56	19.04	7.41	0.13		0.30	0.17		101.57
221-c2-10	48.03	0.47	4.61	0.77	20.58	0.53	17.53	7.51	0.76	0.02	0.26	0.39		101.45
221-c2-11	48.68	0.41	4.19	0.76	20.29	0.57	17.04	8.22	0.52		0.25	0.28		101.21
221-c2-12	48.27	0.49	3.72	0.78	20.31	0.59	18.92	7.00	0.60	0.02	0.25	0.47		101.41
221-c2-13	49.50	0.37	3.82	0.73	19.44	0.60	18.42	8.32	0.41		0.22	0.37		102.19
221-c2-14	49.46	0.62	3.22	0.97	19.30	0.56	18.57	8.05	0.22		0.33	0.44		101.76
221-c2-15	49.53	0.40	7.56	0.70	17.25	0.50	16.47	8.25	0.58	0.03	0.25	0.16		101.70
LOD	0.02	0.03	0.02	0.03	0.03	0.03	0.02	0.04	0.02	0.02	0.03	0.04	0.02	

	SiO_2	TiO_2	Al_2O_3	Cr_2O_3	FeO	MnO	MgO	CaO	Na_2O	K_2O	P_2O_5	SO_3	NiO	Total
221-c3-1	51.18	0.45	2.98	0.51	17.84	0.54	16.85	8.51	0.35	0.01	0.30	0.41	0.03	99.94
221-c3-2	51.26	0.43	2.26	1.14	19.05	0.60	18.20	6.66	0.24	0.02	0.28	0.09	0.02	100.23
221-c3-3	52.12	0.21	1.57	0.63	17.05	0.57	21.27	6.58	0.20	0.01	0.13	0.05	0.02	100.39
221-c3-4	50.87	0.44	3.39	0.51	18.68	0.59	16.45	8.63	0.42	0.01	0.25	0.60	0.04	100.85
221-c3-5	51.24	1.57	4.47	0.42	15.72	0.51	16.75	8.43	0.56	0.04	0.30	0.22	0.03	100.23
221-c3-6	51.29	0.51	3.37	1.15	16.24	0.51	20.23	6.29	0.16	0.02	0.18	0.27		100.23
221-c3-7	48.32	0.46	3.65	0.71	19.50	0.51	19.23	6.24	0.57	0.02	0.26	0.39	0.04	99.86
221-c3-8	47.36	0.44	3.34	0.75	20.25	0.55	20.23	5.56	0.49	0.03	0.37	0.37	0.04	99.74
221-c3-9	49.84	0.40	3.59	0.61	18.52	0.53	19.18	7.21	0.43	0.02	0.20	0.31	0.04	100.85
221-c3-10	50.64	0.42	3.48	0.78	16.84	0.55	18.06	8.66	0.49	0.03	0.25	0.39	0.04	100.57

	SiO_2	TiO_2	Al_2O_3	Cr_2O_3	FeO	MnO	MgO	CaO	Na_2O	K_2O	P_2O_5	SO_3	NiO	Total
221-c3-11	50.36	0.46	3.25	0.74	16.95	0.52	20.73	6.47	0.09	0.01	0.24	0.11	0.06	99.93
221-c3-12	49.68	0.47	3.88	0.69	17.68	0.54	18.08	7.95	0.15	0.01	0.25	0.22	0.04	99.59
221-c3-13	49.61	0.47	3.41	0.55	19.67	0.58	18.08	7.27	0.37	0.01	0.23	0.26	0.03	100.52
221-c3-14	49.04	0.48	4.04	0.71	18.75	0.57	17.86	7.52	0.52	0.02	0.25	0.40	0.03	100.16
221-c3-15	49.62	0.43	1.94	0.40	22.64	0.61	18.03	5.80	0.24	0.01	0.09	0.11		99.93
221-c4-1	52.84	0.29	1.31	0.53	16.87	0.57	20.96	6.17	0.16	0.02	0.33	0.15	0.04	100.20
221-c4-2	52.83	0.33	0.98	0.40	19.52	0.63	19.68	5.60	0.08		0.08	0.07	0.04	100.19
221-c4-3	53.52	0.16	0.76	0.56	17.53	0.65	21.69	5.10	0.07		0.02	0.04	0.03	100.09
221-c4-4	50.50	0.56	1.80	0.70	19.16	0.57	15.68	10.47	0.15	0.01	0.10	1.77	0.07	101.48
221-c4-5	49.11	0.40	2.76	0.60	19.41	0.57	18.15	8.44	0.29	0.02	0.20	0.88	0.03	100.83
221-c4-6	48.68	0.41	2.47	0.57	20.64	0.55	17.67	7.79	0.28	0.02	0.25	1.19	0.07	100.51
221-c4-7	50.25	0.34	1.10	0.30	22.21	0.69	16.89	6.75	0.10	0.01	0.15	0.74	0.02	99.53
221-c4-8	47.97	0.66	3.50	0.58	20.00	0.55	16.68	8.01	0.43	0.03	0.41	1.94	0.07	100.75
221-c4-9	46.08	0.54	3.63	1.58	21.86	0.53	16.32	7.75	0.48	0.03	0.23	2.57	0.08	101.59
221-c4-10	46.78	0.43	3.31	0.59	21.53	0.57	16.91	7.79	0.42	0.02	0.32	2.29	0.04	100.96
221-c5-1	49.58	0.78	3.41	0.67	17.31	0.56	17.97	8.18	0.43	0.02	0.95	0.45	0.02	100.31
221-c5-2	47.49	0.54	3.55	0.66	21.79	0.56	17.90	6.81	0.56	0.04	0.32	0.60		100.82
221-c5-3	48.57	0.49	5.12	0.85	19.28	0.59	16.90	7.65	0.55	0.03	0.25	0.52	0.06	100.80
221-c5-4	46.61	0.47	3.80	0.67	23.51	0.65	16.81	6.99	0.38	0.02	0.32	0.53	0.03	100.75
221-c5-5	49.04	0.52	3.70	0.74	19.27	0.57	16.04	8.60	0.32	0.01	0.27	0.27	0.04	99.35
221-c6-1	47.96	0.48	3.58	0.74	20.57	0.55	16.63	8.29	0.36	0.03	0.32	0.34		99.84
221-c6-2	47.38	0.46	3.55	0.77	20.37	0.54	18.19	6.89	0.55	0.02	0.31	0.42	0.03	99.44
221-c6-3	47.77	0.49	3.70	0.79	20.11	0.53	18.56	6.77	0.57	0.03	0.27	0.43	0.04	100.02
221-c6-4	45.65	0.50	3.72	0.62	21.61	0.61	16.70	7.82	0.30	0.05	0.31	0.38		98.27
221-c6-5	47.89	0.48	3.84	0.78	20.20	0.50	18.33	6.89	0.31	0.03	0.36	0.48		100.08
221-c6-6	50.07	0.31	3.02	0.82	16.93	0.50	20.03	7.23	0.51	0.01	0.20	0.35		99.98
221-c6-7	49.57	0.40	3.57	0.81	18.12	0.54	19.15	7.39	0.41	0.02	0.28	0.36	0.02	100.63
221-c6-8	51.62	0.33	1.73	0.70	13.77	0.52	16.05	13.87	0.18	0.02	0.17		0.02	98.96
221-c6-9	48.94	0.43	3.62	0.72	19.24	0.56	18.21	7.55	0.29	0.02	0.23	0.51		100.31
221-c6-10	48.83	0.45	3.93	0.78	18.96	0.54	18.71	7.26	0.29	0.02	0.24	0.43		100.43
221-c7-1	52.64	0.39	2.11	0.82	15.63	0.56	21.40	6.19	0.20	0.01	0.11	0.09	0.03	100.15
221-c7-2	52.82	0.17	1.17	0.38	15.60	0.53	22.57	5.18	0.15	0.01	0.06	0.07		98.71
221-c7-3	50.76	0.31	2.51	1.09	17.62	0.56	21.71	5.12	0.18	0.03	0.16	0.15	0.04	100.21
221-c7-4	47.85	0.37	3.90	0.69	19.26	0.56	17.37	7.29	0.42	0.05	0.31	0.68	0.03	98.75
221-c7-5	48.73	0.39	2.40	0.51	19.78	0.59	19.22	7.04	0.27	0.02	0.35	0.17		99.46
221-c7-6	49.10	0.39	3.07	1.02	19.06	0.57	19.15	7.13	0.33	0.02	0.18	0.29	0.05	100.30
221-c7-7	48.71	0.36	4.12	0.63	18.26	0.55	18.37	7.40	0.49	0.02	0.24	0.41	0.08	99.56

	SiO_2	TiO_2	Al_2O_3	Cr_2O_3	FeO	MnO	MgO	CaO	Na_2O	K_2O	P_2O_5	SO_3	NiO	Total
221-c7-8	48.48	0.55	5.07	0.58	18.36	0.56	15.06	9.26	0.38	0.02	0.27	0.24		98.82
221-c7-9	50.11	0.32	3.26	0.89	17.39	0.53	20.22	6.36	0.28	0.02	0.21	0.26		99.85
221-c7-10	48.80	0.53	4.19	0.69	19.23	0.62	17.28	7.86	0.56	0.02	0.20	0.41	0.02	100.39
221-c8-1	45.23	0.35	2.70	1.22	20.15	0.48	22.70	5.83	0.37	0.02	0.19	0.23	0.07	99.48
221-c8-2	45.22	0.41	3.16	0.79	22.47	0.61	20.75	5.96	0.44	0.02	0.39	0.53	0.09	100.75
221-c8-3	50.49	0.30	3.24	0.84	16.46	0.51	20.98	6.25	0.35	0.01	0.18	0.30	0.02	99.90
221-c8-4	49.34	0.41	3.25	1.03	17.60	0.52	21.28	5.44	0.25	0.02	0.26	0.43	0.03	99.82
221-c8-5	46.82	0.49	3.31	0.90	19.79	0.56	20.47	6.41	0.33	0.02	0.19	0.26		99.54
221-c8-6	44.54	0.22	2.17	0.65	21.18	0.52	25.88	3.91	0.38	0.02	0.13	0.29	0.08	99.89
221-c8-7	50.05	0.21	3.44	0.69	16.07	0.50	20.55	6.99	0.57	0.01	0.17	0.54	0.06	99.78
221-c8-8	46.38	0.49	3.44	0.77	20.18	0.55	19.47	6.32	0.52	0.02	0.30	0.42		98.85
221-c8-9	48.58	0.46	3.25	0.71	19.99	0.58	18.21	7.10	0.20	0.02	0.45	0.37		99.91
221-c8-10	47.74	0.48	3.48	0.78	20.11	0.59	18.47	6.81	0.19	0.02	0.27	0.35	0.03	99.28
221-c8-11	46.41	0.52	3.72	0.72	22.31	0.61	17.55	7.19	0.29	0.03	0.33	0.65		100.33
221-c9-1	52.30	0.22	0.84	0.58	18.27	0.59	24.00	2.72	0.06	0.02	0.02	0.04	0.02	99.66
221-c9-2	51.41	0.50	3.66	0.35	17.90	0.59	17.75	5.87	0.53	0.04	0.40	0.19	0.03	99.19
221-c9-3	49.91	0.30	3.25	0.70	17.49	0.56	19.58	6.91	0.38	0.01	0.15	0.21	0.03	99.46
221-c9-4	47.52	0.51	3.79	0.95	20.48	0.59	18.00	7.59	0.46	0.02	0.26	0.21		100.37
221-c9-5	46.79	0.44	3.38	0.98	20.92	0.62	18.25	7.37	0.38	0.02	0.25	0.33		99.73
221-c9-6	45.59	0.55	3.76	0.86	22.92	0.59	17.16	7.42	0.55	0.02	0.29	0.26		99.96
221-c9-7	46.90	0.52	2.79	0.71	21.52	0.62	17.99	6.93	0.36	0.01	0.32	0.16	0.03	98.83
221-c10-1	50.28	0.43	3.46	1.00	17.57	0.56	16.70	8.31	0.47	0.03	0.26	0.24	0.03	99.31
221-c10-2	47.43	0.57	4.19	0.55	21.40	0.58	16.37	8.16	0.39	0.03	0.36	0.61		100.63
221-c10-3	48.72	0.75	3.20	0.47	19.32	0.56	13.90	10.85	0.41	0.03	0.36	0.46	0.02	99.02
221-c10-4	47.64	0.52	4.10	0.74	20.81	0.56	16.48	7.70	0.52	0.04	0.26	0.50	0.03	99.86
221-c10-5	47.02	0.39	3.92	0.52	20.73	0.53	19.14	6.18	0.61	0.03	0.30	0.32	0.05	99.70
221-c10-6	47.73	0.50	4.38	0.79	19.29	0.55	17.62	7.58	0.42	0.02	0.33	0.51	0.03	99.71
221-c11-1	48.64	0.54	3.62	0.63	19.22	0.55	17.10	7.97	0.45	0.01	0.29	0.69	0.05	99.70
221-c11-2	41.57	0.40	3.02	0.57	16.91	0.49	14.94	13.39	0.49	0.02	7.63	0.61	0.05	100.05
221-c11-3	47.05	0.51	3.43	0.67	21.42	0.62	17.73	7.26	0.42	0.02	0.28	0.36	0.02	99.77
221-c11-4	51.17	0.30	1.15	0.45	19.91	0.63	19.73	5.34	0.11	0.01	0.17	0.16	0.03	99.13
221-c11-5	48.72	0.39	3.62	0.85	19.02	0.53	19.23	6.46	0.15	0.01	0.23	0.38	0.05	99.60
LOD	0.02	0.03	0.02	0.04	0.03	0.03	0.03	0.01	0.02	0.01	0.02	0.04	0.02	

Table A2: EPMA results for crystallite-rich regions of shock melt in MET11640/2-2-1/TEP.

sample	SiO_2	TiO_2	Al_2O_3	Cr_2O_3	FeO	MnO	MgO	CaO	Na_2O	K_2O	P_2O_5	SO_3	NiO	Total
232-c1-1	48.71	0.52	4.12	0.65	18.59	0.53	16.02	8.23	0.72	0.02	0.67	0.81	0.02	99.59
232-c1-2	49.63	0.48	5.34	0.63	18.26	0.51	15.27	7.78	0.84	0.02	0.20	0.44	0.02	99.38
232-c1-3	49.35	0.50	4.16	0.60	18.76	0.55	16.03	8.15	0.62	0.02	0.26	0.57	0.04	99.58
232-c1-4	48.65	0.42	3.87	0.56	19.66	0.55	16.68	7.32	0.54	0.02	0.28	0.57		99.11
232-c1-5	49.17	0.49	4.69	0.59	18.84	0.56	15.92	7.77	0.69	0.02	0.23	0.61	0.02	99.59
232-c1-6	49.77	0.42	7.96	0.46	16.64	0.44	13.77	8.09	1.12	0.03	0.21	0.37		99.28
232-c1-7	49.68	0.46	6.16	0.55	17.70	0.47	14.36	8.52	0.95	0.03	0.23	0.40		99.51
232-c1-8	49.29	0.48	3.73	0.59	19.82	0.56	16.54	7.54	0.47	0.02	0.24	0.76	0.02	100.04
232-c1-9	49.12	0.47	3.79	0.58	19.60	0.54	16.94	7.27	0.53	0.03	0.21	0.69	0.02	99.76
232-c1-10	48.07	0.53	3.55	0.59	20.46	0.59	15.73	7.74	0.89	0.22	0.29	0.60		99.25
232-c2-1	50.69	0.51	4.14	0.60	18.27	0.56	15.52	8.75	0.49	0.02	0.20	0.41	0.03	100.17
232-c2-2	51.01	0.50	4.93	0.61	17.04	0.53	14.77	9.00	0.77	0.02	0.18	0.12		99.47
232-c2-3	50.95	0.51	4.24	0.59	17.51	0.56	15.26	9.20	0.54	0.03	0.19	0.35	0.03	99.93
232-c2-4	50.44	0.53	3.88	0.70	17.85	0.55	15.34	9.12	0.40	0.01	0.21	0.29	0.04	99.33
232-c2-5	50.77	0.57	4.44	0.69	17.16	0.52	15.18	9.40	0.64	0.02	0.24	0.29		99.91
232-c2-6	50.88	0.58	4.11	0.57	17.85	0.56	14.84	9.15	0.46	0.03	0.23	0.63	0.03	99.87
232-c2-7	50.87	0.52	4.22	0.67	17.80	0.54	15.35	9.00	0.52	0.03	0.20	0.12	0.04	99.85
LOD	0.02	0.03	0.02	0.04	0.03	0.03	0.03	0.01	0.02	0.01	0.02	0.04	0.02	

Table A3: EPMA results for shock melt glass in MET11640/2-3-2/TEP.

sample	SiO_2	TiO_2	Al_2O_3	Cr_2O_3	FeO	MnO	MgO	CaO	Na_2O	K_2O	P_2O_5	SO_3	NiO	Total
232-c1-1	46.87	0.53	4.75	0.58	22.17	0.61	15.87	7.42	0.60	0.02	0.33	0.82	0.03	100.56
232-c1-2	46.56	0.53	2.65	0.36	22.93	0.58	14.90	10.19	0.27	0.01	0.17	0.34		99.48
232-c1-3	50.70	0.42	3.10	0.66	15.97	0.53	16.50	11.01	0.41	0.01	0.20	0.24	0.03	99.76
232-c1-4	49.32	0.45	4.76	0.59	18.68	0.54	16.18	8.18	0.59	0.03	0.21	1.58	0.05	101.10
232-c1-5	48.62	0.51	4.79	0.64	19.46	0.58	16.35	7.83	0.62	0.02	0.34	1.58	0.06	101.35
232-c1-6	47.77	0.50	4.99	0.58	20.42	0.55	15.82	7.91	0.65	0.03	0.27	2.01	0.02	101.50
232-c1-7	45.79	0.54	4.62	0.38	23.73	0.57	16.27	7.07	0.70	0.03	0.21	1.05	0.02	100.96
232-c1-8	45.86	0.39	3.56	0.48	23.30	0.64	18.80	6.52	0.49	0.02	0.18	0.67	0.06	100.91
232-c1-9	47.64	0.36	4.09	0.65	21.04	0.56	17.30	7.26	0.59	0.01	0.21	0.45	0.04	100.15
232-c2-1	50.69	0.61	2.73	0.82	16.86	0.55	15.94	10.18	0.35	0.02	0.12		0.02	98.86
232-c2-2	52.61	0.20	1.10	0.57	15.93	0.56	19.80	7.82	0.12		0.02		0.03	98.72
232-c2-3	48.55	0.77	2.66	1.10	19.95	0.59	16.64	8.15	0.33	0.02	0.17	0.12	0.02	99.07
232-c2-4	51.21	0.51	3.61	0.50	18.45	0.55	15.69	8.13	0.39	0.02	0.07		0.03	99.14
232-c3-1	47.51	0.48	2.94	0.57	21.33	0.62	18.34	7.56	0.39	0.02	0.20	0.18	0.03	100.13
232-c3-2	50.33	0.85	1.65	0.62	16.47	0.55	16.15	11.22	0.19	0.03	0.16			98.21
232-c3-3	46.75	0.48	1.94	0.46	22.50	0.63	18.96	7.35	0.20	0.01	0.23	0.04		99.54
232-c4-1	48.79	0.52	3.39	0.47	19.70	0.61	16.12	8.20	0.42	0.03	0.24	0.95		99.43
232-c4-2	48.30	0.43	4.30	0.41	19.53	0.58	15.48	8.01	0.56	0.02	0.26	1.87		99.76
232-c4-3	49.38	0.44	4.66	0.52	18.40	0.54	14.91	8.34	0.57	0.03	0.21	3.15	0.05	101.15
232-c4-4	51.58	0.38	2.34	0.52	18.26	0.58	17.16	8.15	0.23	0.02	0.19	0.54		99.95
232-c4-5	49.73	0.46	3.26	0.49	18.03	0.55	15.55	9.56	0.39	0.02	0.23	1.44		99.73
232-c5-1	48.02	0.45	3.68	0.52	19.79	0.57	17.50	7.13	0.49	0.02	0.43	0.26	0.02	98.86
232-c5-2	51.86	0.16	1.08	0.49	16.59	0.59	19.98	6.93	0.16	0.01	0.03	0.28		98.15
232-c5-3	50.61	0.49	1.60	0.43	20.06	0.66	15.81	9.16	0.20	0.02	0.06	0.04	0.03	99.14
232-c5-1	50.90	0.51	1.19	0.35	23.95	0.76	15.05	6.52	0.15	0.02	0.16	0.48	0.06	100.05
232-c5-2	48.71	0.73	4.15	0.61	20.75	0.56	15.62	7.66	0.58	0.02	0.19	0.35		99.93
232-c5-3	49.84	0.60	3.81	0.70	18.31	0.58	15.65	8.99	0.56	0.04	0.17	0.43	0.04	99.67
232-c5-4	49.94	0.57	3.72	0.64	19.14	0.61	16.07	8.42	0.52	0.03	0.21	0.83		100.69
232-c5-5	53.75	0.11	0.70	0.45	17.04	0.59	23.15	3.86	0.06	0.01	0.02	0.04		99.79
232-c6-1	49.08	0.46	3.95	0.54	19.22	0.58	17.43	7.38	0.57	0.01	0.36	0.75	0.02	100.33
232-c6-2	52.04	0.23	3.17	0.55	14.29	0.48	19.40	7.84	0.56	0.01	0.07	0.36		99.00
232-c6-3	50.86	0.22	4.08	0.61	16.36	0.53	18.09	7.89	0.69	0.01	0.21	0.85	0.03	100.40
232-c6-4	51.32	0.28	1.71	0.45	20.00	0.69	19.57	6.05	0.15	0.02	0.13	0.19		100.57
232-c6-5	46.74	1.45	4.02	0.61	23.56	0.62	16.11	6.86	0.57	0.03	0.27	1.57	0.03	102.41
232-c6-6	49.27	0.47	4.34	0.60	18.13	0.53	16.98	7.69	0.67	0.02	0.30	1.10	0.02	100.11
232-c6-7	50.31	0.48	3.56	0.53	19.27	0.57	17.11	7.13	0.46	0.02	0.23	0.78		100.45
232-c6-8	43.18	0.59	3.81	0.36	26.38	0.62	18.97	4.85	0.48	0.03	0.22	2.07	0.06	101.54

	SiO_2	TiO_2	Al_2O_3	Cr_2O_3	FeO	MnO	MgO	CaO	Na_2O	K_2O	P_2O_5	SO_3	NiO	Total
LOD	0.02	0.03	0.02	0.04	0.03	0.03	0.03	0.01	0.02	0.01	0.02	0.04	0.02	

Table A4: EPMA results for crystallite-rich regions of shock melt in MET11640/2-3-2/TEP.

sample	SiO_2	TiO_2	Al_2O_3	Cr_2O_3	FeO	MnO	MgO	CaO	Na_2O	K_2O	P_2O_5	SO_3	Cl	Total
234-g1-1	46.91		3.32		21.59	0.60	19.33	6.53	0.41		0.26			98.96
234-g1-2	47.10		3.56		21.45	0.61	19.18	6.71	0.40		0.20			99.21
234-g1-3	47.30		2.97		21.83	0.58	19.82	6.48	0.37		0.28			99.63
234-g1-4	46.75		3.13		21.79	0.58	19.26	6.63	0.40		0.30			98.82
234-g1-5	46.33		3.07		22.06	0.56	19.21	6.56	0.36		0.25			98.41
234-g1-6	46.30		3.15		21.92	0.58	19.26	6.63	0.37		0.30			98.50
234-g1-7	48.90		2.63		19.17	0.57	19.45	8.34	0.38					99.43
234-g1-8	51.71		1.34		16.24	0.51	19.37	9.61	0.24					99.02
234-g1-9	50.31		6.09		17.48	0.47	16.12	7.63	0.97					99.07
234-g1-10	51.70		2.40		17.58	0.63	19.03	7.50	0.41					99.23
234-g1-11	49.25		1.89		19.99	0.60	18.54	8.47	0.26					99.00
234-g1-12	46.90		3.12		21.12	0.62	19.44	7.30	0.33		0.35			99.19
234-g1-13	46.85		3.12		21.67	0.51	19.39	6.71	0.30		0.27			98.83
234-g1-14	46.98		3.14		21.20	0.52	19.12	6.86	0.37		0.27			98.45
234-g1-15	47.52		3.16		20.85	0.64	19.32	6.73	0.43					98.65
234-g1-16	47.49		4.09		20.68	0.58	19.12	6.68	0.47		0.23			99.32
234-g1-17	47.18		13.02		14.50	0.45	9.64	10.52	1.49		1.00			97.79
234-g1-18	50.20		2.57		19.12	0.55	16.91	8.65	0.45		0.67			99.11
234-g1-19	51.79		13.89		12.21		9.72	9.48	1.85					98.94
234-g1-20	48.47		7.10		17.80	0.46	16.22	7.82	0.84					98.69
234-g1-21	47.26		3.26		21.07	0.56	19.07	6.99	0.39		0.26			98.87
234-g1-22	47.01		3.54		21.14	0.55	18.99	7.06	0.40		0.20			98.89
234-g2-1	48.59		3.73		20.17	0.56	17.23	8.01	0.46		0.27			99.02
234-g2-2	48.43		4.32		20.15	0.57	16.17	8.32	0.56		0.30			98.83
234-g2-3	48.43		4.11		20.29	0.53	16.65	8.13	0.52		0.26			98.92
234-g2-4	51.10		2.67		16.13	0.55	16.71	11.37	0.20					98.75
234-g2-5	50.38		1.50		17.36	0.62	16.67	11.55	0.18					98.27
234-g2-6	49.44		2.61		17.59	0.53	17.39	10.95	0.27					98.78
234-g2-7	47.74		2.90		21.63	0.57	16.47	8.12	0.33		0.30	0.68		98.75
234-g2-8	47.39		2.91		21.43	0.62	17.03	7.96	0.28		0.36	1.14		99.13
234-g2-9	47.51		2.69		21.50	0.62	16.92	8.11	0.29		0.29	0.96		98.88
234-g3-1	50.15		3.62		18.01	0.60	15.80	9.72	0.41		0.23	1.03		99.55
234-g3-2	48.40		5.35		17.25	0.49	14.98	9.69	0.65		0.36	2.18		99.35
234-g3-3	51.63		1.48		15.50	0.57	18.22	11.55	0.14					99.08
234-g3-4	43.54		3.85	1.20	22.64	0.63	15.67	7.26	0.49		0.25	1.22		96.74
234-g3-5	47.53		5.66		17.35	0.53	14.46	9.80	0.66		0.38	1.85		98.22
234-g3-6	51.39		0.95		18.85	0.68	19.83	6.59	0.17			0.63		99.08

	SiO_2	TiO_2	Al_2O_3	Cr_2O_3	FeO	MnO	MgO	CaO	Na_2O	K_2O	P_2O_5	SO_3	Cl	Total
234-g3-7	52.29		0.92		17.54	0.62	21.26	6.91	0.18					99.73
234-g3-8	50.66		2.57		16.32	0.54	16.56	11.66	0.22					98.54
234-g3-9	47.24		5.34		18.01	0.51	14.48	9.72	0.75		0.39	2.52		98.95
LOD	1.53	2.14	0.62	0.89	0.94	0.43	0.32	0.61	0.06	0.12	0.19	0.56	0.06	

Table A5: EPMA results for shock melt glass in MET11640/2-3-4/TEP.

sample	SiO_2	TiO_2	Al_2O_3	Cr_2O_3	Fe	MnO	MgO	CaO	Na_2O	K_2O	P_2O_5	S	Cl	total	Fe/S
p-1			0.02		61.34							39.48		100.84	0.892
p-2	0.07			0.08	60.49	0.07		0.12				39.56		100.40	0.878
p-3	0.05				60.82			0.03				39.34		100.25	0.888
p-4	0.09	0.05			60.37			0.16				39.49		100.16	0.878
sa-1	0.63	0.06	0.07	0.12	66.14	0.24	0.19	0.30	0.05			32.78		100.59	1.159
sa-2	2.18	0.09	0.14	0.09	67.43	0.30	0.51	0.51				23.52		94.77	1.646
sa-3	2.07	0.18	0.31	0.20	66.49	0.17	0.18	0.72	0.05			28.29		98.65	1.349
sa-4	0.37			0.22	68.35	0.22		0.30	0.04			28.30		97.80	1.387
sa-5	1.94	0.06	0.12	0.09	64.27	0.15	0.54	0.34	0.05			28.90		96.45	1.277
sb-1	0.05			0.12	61.50	0.10		0.14	0.04			37.52		99.46	0.941
sb-2	0.08		0.02	1.15	62.00	0.15		0.17				37.28		100.86	0.955
sb-3	0.13		0.03	1.70	61.15	0.14		0.23	0.06			37.70		101.14	0.931
sb-4	0.17	0.06	0.04	0.34	60.86	0.13		0.22				36.88		98.71	0.948
sb-5	0.17	0.04	0.03	0.37	60.96	0.18		0.25				37.28		99.28	0.939
sb-6	0.17			0.34	61.42	0.19		0.25				36.98		99.35	0.954
sb-7	0.09	0.07		0.32	61.97	0.15		0.19				37.02		99.80	0.961
sb-8	0.12			0.44	61.31	0.21		0.20				37.21		99.49	0.946
sb-9	0.06				60.92			0.07				39.51		100.56	0.885
sb-10	0.72		0.11	0.08	61.21	0.12	0.32	0.41	0.05			36.35		99.36	0.967
sb-11	0.23		0.03	0.07	60.94	0.07	0.03	0.22	0.05			35.38	0.07	97.07	0.989
sb-12	0.29	0.04	0.03	0.09	61.07	0.14	0.03	0.17				37.28		99.14	0.941
sb-13	0.34		0.04	0.19	60.95	0.07	0.05	0.23				36.46		98.32	0.960
sb-14	0.15		0.04	0.14	62.19	0.16		0.26				34.38	0.04	97.36	1.039
sb-15	0.33	0.05	0.04	0.22	61.26	0.12		0.28				36.83		99.13	0.955
sb-16	0.42	0.06	0.03	0.27	60.68	0.15	0.05	0.36	0.06			36.10		98.19	0.965
sb-17	0.29			0.38	61.94	0.12	0.04	0.30				35.88		98.94	0.991
LOD	0.04	0.04	0.02	0.05	0.05	0.05	0.03	0.03	0.03	0.03	0.06	0.08	0.04		

Table A6: EPMA results for iron sulfides MET11640/2-3-4/TEP. Data labeled "p" are groundmass pyrrhotite. Data labelled "s" are shock metamorphic sulfide spherules.

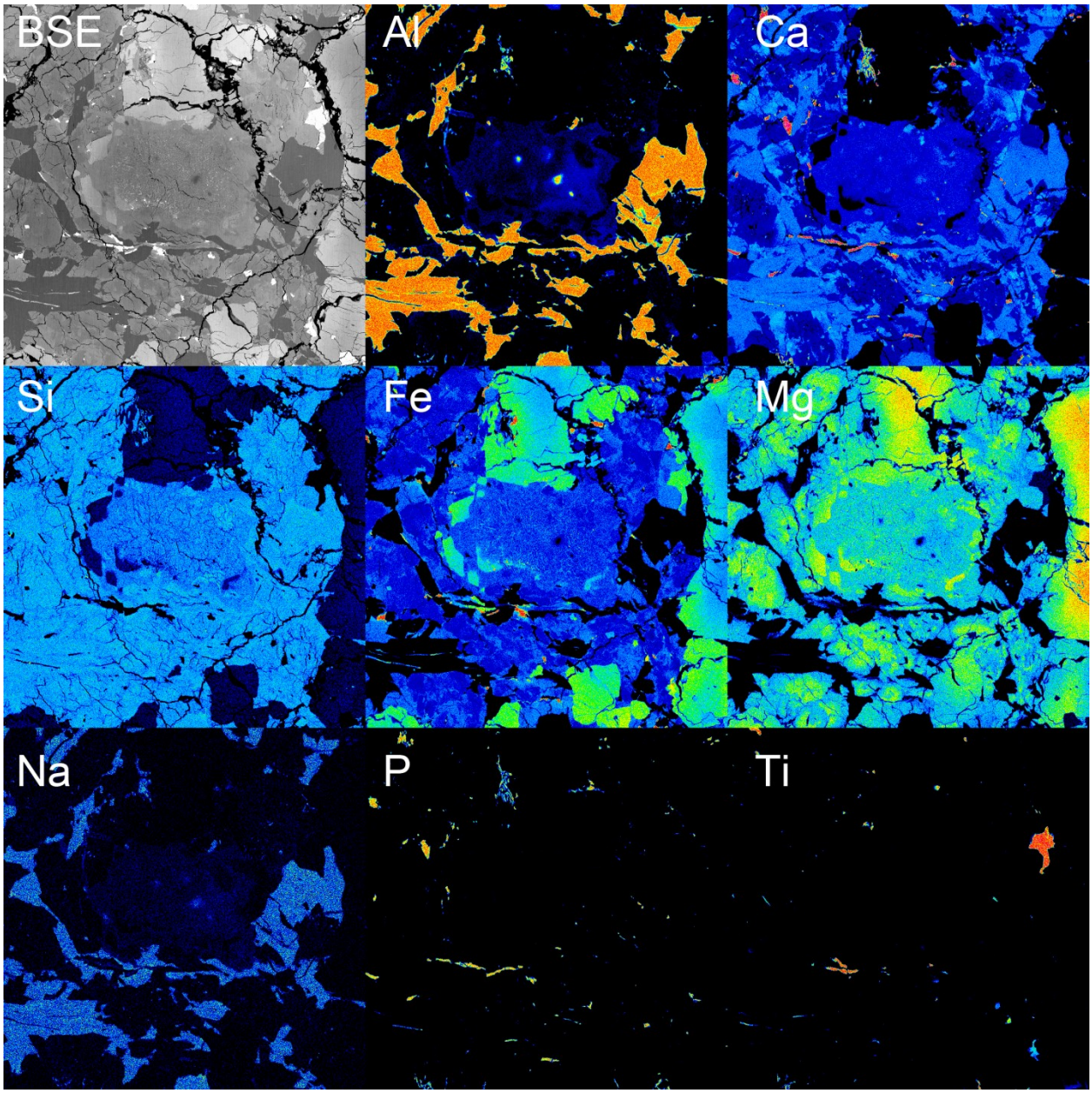

Figure A9: X-ray elemental maps for a shock melt pocket in MET11640/2-3-4. Small crystals exhibiting high concentrations of both phosphorus and calcium demonstrate that merrillite present in this region with a small modal %. Field of view = 800 µm.

	H_2O		F		Cl		S		P_2O_5			
sample	ppm	2σ	ppm	2σ	ppm	2σ	ppm	2σ	wt%	2σ	δD	2σ
234-1	297.6	3.1	11.7	0.1	14.2	0.1	1067.4	6.7	0.2576	0.0061	3757	49
234-2	278.5	2.3	11.7	0.1	15.9	0.1	1073.2	2.7	0.2499	0.0064	2913	77
234-3	261.6	2.6	10.3	0.1	11.2	0.2	614.7	9.9	0.1657	0.0072	4422	67
234-4	373.9	6.1	10.9	0.1	13.5	0.1	809.7	10.6	0.1963	0.0079	3831	38
234-5	329.9	4.6	10.2	0.1	11.3	0.1	715.3	6.3	0.1610	0.0063	4007	56
234-6	353.0	4.2	10.8	0.1	19.9	0.2	288.2	3.9	0.1048	0.0020	4232	53
234-7	266.9	2.6	11.5	0.1	16.1	0.1	1075.0	9.1	0.2956	0.0137	4325	57
234-8	234.3	3.6	9.6	0.1	28.2	1.6	573.6	22.8	0.1479	0.0028	2559	89
234-9	1043.5	110.3	12.4	0.5	266.4	40.9	1218.2	246.1	0.0291	0.0049		
234-10	533.6	48.3	3.9	0.1	18.9	0.8	146.4	5.0	0.0520	0.0006		
234-11	2555.4	541.4	11.5	0.5	315.2	53.8	3802.8	329.5	0.0153	0.0010		
234-12	1732.5	23.8	19.8	0.3	98.4	0.9	1180.2	41.3	0.0886	0.0044		
234-13	88.7	4.4	7.5	0.1	2.0	0.2	349.6	78.1	0.0034	0.0001		
234-14	484.6	18.2	8.5	0.2	37.8	2.0	1962.8	472.3	0.0311	0.0021		
234-15	601.0	39.2	17.8	0.3	166.1	19.4	4345.5	785.7	0.2178	0.0194		
234-16	817.7	58.7	3.7	0.5	42.0	2.4	63.9	7.2	0.0201	0.0007		
234-17	174.3	4.7			7.2	0.3	156.0	7.9	0.0643	0.0007		
234-18	764.7	7.0	23.9	0.4	74.2	1.2	4858.2	45.9	0.2980	0.0049		
234-19	259.2	4.3	11.7	0.1	13.7	0.1	1337.9	24.3	0.2100	0.0050		
234-20	275.2	3.8	11.5	0.1	13.6	0.1	1070.2	1.9	0.2047	0.0041		
234-21	277.5	3.7	11.6	0.1	13.0	0.1	1070.5	1.9	0.2147	0.0037		
234-22	291.1	4.4	10.8	0.1	12.4	0.1	1001.7	8.3	0.2061	0.0044		
234-23	363.9	50.7	13.9	0.6	15.7	0.8	425.8	16.9	0.1308	0.0023		
234-24	453.8	7.6	13.6	0.4	8.7	0.3	341.3	25.9	0.1057	0.0086		
234-25	490.3	3.1	15.7	0.1	19.0	0.1	378.4	2.8	0.0986	0.0031		
234-26	476.7	2.3	13.3	0.1	18.9	0.1	633.6	2.6	0.1472	0.0031		
234-27	350.8	3.6	11.9	0.1	12.9	0.1	919.6	7.2	0.2106	0.0031		
234-28	268.6	4.3	11.5	0.1	14.2	0.1	1070.9	3.1	0.2130	0.0023		
234-29	259.6	4.2	12.2	0.1	13.3	0.1	987.0	5.8	0.2298	0.0028		
234-30	270.2	3.9	12.2	0.1	12.8	0.1	977.7	4.7	0.2209	0.0039		
234-31	314.5	3.0	12.2	0.1	12.5	0.1	881.9	6.5	0.2140	0.0041		
234-32	72.6	3.2	6.1	0.2	2.7	0.1	65.4	2.5	0.0969	0.0076		

Table A7: SIMS results for volatile concentrations and hydrogen isotopes in MET11640/2-3-4/TEP shock melt glass.

sample	La			Ce			Pr			Nd			Sm		
	ppm	2σ%	LOD	ppm	2σ%	LOD	ppm	2σ%	LOD	ppm	2σ%	LOD	ppm	2σ%	LOD
Ol-1			0.18			0.17			0.14			0.12			0.21
Ol-2			0.32			0.65			0.07			0.25			0.07
Ol-3			0.37			0.57			0.05			0.27			0.07
Ol-4			0.30			0.53			0.06			0.22			0.04
Ol-5			0.30			0.53	0.50	200	0.05			0.17			0.04
Ol-6			0.22			0.41			0.05			0.12	0.02	42	0.01
Ol-7			0.02			0.04			0.005			0.01	0.01	33	0.01
Ol-8			0.75			1.04			0.11			0.60			0.04
Ol-9			0.36			0.72			0.09			0.28			0.07
Ol-10			0.17			0.28			0.03	0.13	28	0.09	0.06	30	0.01
Ol-11			0.44			0.91			0.12			0.29			0.06
Ol-12			0.44			0.79			0.08			0.30			0.05
Ol-13			0.47			0.81			0.09			0.41			0.03
Px-1			0.18			0.38			0.03	0.26	18	0.12	0.20	29	0.01
Px-2			0.30			0.68	0.07	14	0.06	0.44	11	0.21	0.39	19	0.04
Px-3			0.50			0.90			0.09			0.19	0.13	39	0.08
Px-4			0.36			0.68			0.08			0.25	0.12	19	0.08
Px-5			0.36			0.60			0.07	0.28	36	0.25	0.22	18	0.04
Px-6			0.29			0.57	0.08	44	0.08	0.50	42	0.22	0.31	35	0.03
Px-7			0.24			0.48			0.06			0.13	0.10	23	0.05
Px-8			0.32			0.63			0.06			0.22	0.10	42	0.02
Px-9			0.57			1.06			0.11			0.36			0.05
Px-10			0.40			0.71			0.07			0.34	0.14	13	0.04
Px-11			0.38			0.69			0.07			0.27	0.16	37	0.07
Px-12			0.39			0.72			0.09			0.29	0.23	32	0.03
Px-13			0.60			1.00			0.17			0.34	0.21	43	0.13
Msk-1			0.67			1.04			0.10			0.52			0.10
Msk-2			0.62			1.05			0.11			0.44	0.03	104	0.02
Msk-3			0.47			0.78			0.10			0.38	0.31	45	0.01
Msk-4			0.40			0.78	0.09	29	0.08	0.32	31	0.20	0.26	46	0.08
Msk-5			0.25	0.42	21	0.37			0.25	0.47	34	0.23	0.32	34	0.20
Msk-6			0.45			0.87			0.08			0.46	0.12	31	0.03
Msk-7			0.56			1.03			0.14			0.45			0.17
Msk-8			0.40	0.90	19	0.75	0.17	27	0.09	0.93	24	0.29	0.61	25	0.05
Msk-9			1.27			2.39			0.28			0.77			0.16
Msk-10			0.52			0.99	0.16	8	0.14	1.37	21	0.50	0.80	20	0.11
Mer-1	18.2	44.5	0.1	94.0	46.8	0.5	14.1	41.8	0.6	117.0	29.9	0.1	54.0	42.6	1.7

sample	Eu			Gd			Tb			Dy			Ho		
	ppm	2σ%	LOD	ppm	2σ%	LOD	ppm	2σ%	LOD	ppm	2σ%	LOD	ppm	2σ%	LOD
Ol-1			0.17			0.11			0.15			0.15			0.18
Ol-2			0.02			0.03			0.003			0.05			0.01
Ol-3			0.05			0.06			0.01	0.03	41	0.02	0.01	42	0.01
Ol-4			0.02			0.05			0.004			0.05			0.01
Ol-5			0.04			0.05	0.01	35	0.01			0.09	0.004	95	0.004
Ol-6			0.01			0.04	0.004	63	0.003	0.04	31	0.01	0.01	48	0.01
Ol-7	0.003	23	0.001	0.03	37	0.01	0.005	10	0.001	0.04	21	0.004	0.01	29	0.001
Ol-8			0.04	0.05	126	0.03			0.01			0.16	0.02	168	0.01
Ol-9			0.05			0.07			0.01			0.12			0.02
Ol-10	0.02	36	0.02	0.15	18	0.03	0.03	20	0.003	0.23	18	0.02	0.05	11	0.001
Ol-11			0.05			0.07			0.01			0.11			0.01
Ol-12			0.01			0.06			0.01			0.05			0.01

	Eu			Gd			Tb			Dy			Ho		
	ppm	2σ%	LOD	ppm	2σ%	LOD	ppm	2σ%	LOD	ppm	2σ%	LOD	ppm	2σ%	LOD
Ol-13			0.04			0.10			0.01			0.04			0.01
Px-1	0.09	20	0.01	0.49	15	0.04	0.11	11	0.005	0.88	7	0.03	0.17	7	0.01
Px-2	0.13	16	0.03	0.75	8	0.09	0.14	9	0.02	1.18	10	0.11	0.28	4	0.03
Px-3	0.06	29	0.04	0.29	29	0.07	0.05	22	0.01	0.44	17	0.08	0.10	9	0.03
Px-4	0.06	33	0.04	0.34	11	0.03	0.08	12	0.01	0.60	20	0.04	0.12	16	0.02
Px-5	0.05	20	0.03	0.39	14	0.05	0.08	7	0.01	0.57	9	0.07	0.13	14	0.01
Px-6	0.14	28	0.05	0.71	28	0.02	0.14	30	0.01	1.14	24	0.04	0.24	24	0.01
Px-7	0.08	27	0.02	0.27	28	0.04	0.05	19	0.01	0.50	22	0.05	0.10	19	0.003
Px-8	0.04	32	0.02	0.18	24	0.04	0.03	20	0.01	0.30	24	0.06	0.07	14	0.01
Px-9			0.05	0.14	28	0.01	0.03	34	0.01	0.28	30	0.05	0.07	24	0.02
Px-10	0.05	28	0.04	0.29	22	0.08	0.06	26	0.01	0.43	19	0.03	0.10	19	0.01
Px-11	0.06	32	0.03	0.27	28	0.03	0.05	18	0.003	0.45	15	0.07	0.10	19	0.002
Px-12	0.09	28	0.06	0.52	17	0.13	0.13	14	0.02	0.93	12	0.14	0.22	9	0.03
Px-13	0.06	36	0.05	0.29	41	0.14	0.06	27	0.02	0.53	25	0.07	0.11	18	0.02
Msk-1			0.05			0.10			0.01			0.06			0.02
Msk-2	0.86	7	0.08			0.13	0.01	48	0.01	0.09	44	0.07	0.03	27	0.01
Msk-3	0.75	13	0.04	0.55	25	0.06	0.09	34	0.02	0.66	32	0.07	0.14	33	0.02
Msk-4	0.74	8	0.06	0.47	43	0.06	0.08	39	0.01	0.49	35	0.04	0.09	34	0.02
Msk-5	0.72	15	0.26	0.52	37	0.23			0.26	0.67	27	0.17			0.23
Msk-6	0.75	7	0.03	0.19	32	0.05	0.04	32	0.02	0.29	21	0.06	0.05	20	0.02
Msk-7	0.73	11	0.06	0.17	53	0.12	0.04	39	0.01	0.23	42	0.11	0.06	29	0.03
Msk-8	0.89	6	0.03	1.01	29	0.05	0.18	28	0.01	1.38	23	0.10	0.29	30	0.01
Msk-9	0.76	5	0.16			0.28			0.06			0.21			0.06
Msk-10	0.92	9	0.02	1.31	16	0.13	0.25	13	0.02	1.71	17	0.12	0.33	13	0.01
Mer-1	16.7	46.1	1.2	112.0	52.7	0.1	19.0	57.9	0.9	145.0	40.7	0.9	26.0	57.7	0.4

sample	Er			Tm			Yb			Lu		
	ppm	2σ%	LOD	ppm	2σ%	LOD	ppm	2σ%	LOD	ppm	2σ%	LOD
Ol-1			0.16			0.15			0.17			0.14
Ol-2			0.05	0.01	49	0.005			0.07	0.01	50	0.01
Ol-3	0.06	27	0.04	0.01	53	0.01	0.11	29	0.01	0.02	28	0.01
Ol-4	0.03	52	0.02	0.01	45	0.004	0.07	42	0.06	0.01	41	0.01
Ol-5			0.05			0.001			0.03	0.01	36	0.003
Ol-6	0.03	38	0.02			0.01	0.05	43	0.01	0.01	49	0.005
Ol-7	0.02	26	0.001	0.004	17	0.001	0.03	19	0.002	0.004	24	0.001
Ol-8	0.13	74	0.08	0.02	88	0.02			0.16	0.03	38	0.01
Ol-9			0.06	0.01	77	0.01			0.13	0.01	34	0.01
Ol-10	0.14	15	0.01	0.02	23	0.003	0.16	14	0.03	0.03	18	0.001
Ol-11			0.04			0.004			0.04			0.01
Ol-12			0.04			0.01	0.06	49	0.03			0.01
Ol-13	0.04	47	0.03			0.01			0.07			0.01
Px-1	0.54	8	0.01	0.07	10	0.005	0.52	4	0.03	0.07	10	0.004
Px-2	0.87	10	0.08	0.12	23	0.004	0.87	10	0.05	0.13	11	0.01
Px-3	0.35	14	0.07	0.06	22	0.01	0.37	20	0.05	0.06	11	0.01
Px-4	0.36	13	0.02	0.05	32	0.004	0.42	18	0.02	0.05	17	0.01
Px-5	0.46	9	0.02	0.07	13	0.01	0.47	8	0.06	0.06	15	0.01
Px-6	0.71	24	0.02	0.11	15	0.004	0.67	22	0.04	0.11	24	0.01
Px-7	0.32	11	0.03	0.05	30	0.01	0.24	20	0.04	0.04	27	0.01
Px-8	0.25	25	0.03	0.04	30	0.01	0.28	26	0.05	0.03	15	0.005
Px-9	0.19	16	0.04	0.04	37	0.01	0.22	26	0.05	0.04	26	0.01
Px-10	0.33	24	0.04	0.06	27	0.004	0.34	18	0.07	0.05	29	0.01
Px-11	0.31	32	0.08	0.06	23	0.002	0.24	21	0.02	0.05	20	0.01

	Er			Tm			Yb			Lu		
	ppm	2σ%	LOD	ppm	2σ%	LOD	ppm	2σ%	LOD	ppm	2σ%	LOD
Px-12	0.64	8	0.07	0.09	19	0.005	0.67	13	0.08	0.09	16	0.01
Px-13	0.33	13	0.05	0.05	23	0.01	0.33	13	0.06	0.05	38	0.01
Msk-1			0.06			0.02			0.10			0.01
Msk-2	0.05	45	0.02			0.02	0.13	32	0.11	0.02	63	0.005
Msk-3	0.45	29	0.05	0.06	14	0.01	0.40	35	0.05	0.05	36	0.01
Msk-4	0.31	39	0.04	0.04	35	0.01	0.28	32	0.07	0.06	56	0.01
Msk-5	0.42	23	0.28			0.29	0.47	26	0.29			0.29
Msk-6	0.18	31	0.04	0.02	35	0.01	0.17	35	0.07	0.03	30	0.01
Msk-7	0.21	35	0.07	0.03	44	0.02	0.22	50	0.09	0.03	46	0.02
Msk-8	0.82	27	0.06	0.11	41	0.01	0.85	32	0.06	0.11	26	0.01
Msk-9			0.14			0.02			0.12			0.03
Msk-10	1.08	19	0.06	0.12	24	0.004	0.88	8	0.09	0.13	16	0.02
Mer-1	84.0	47.6	0.7	10.2	57.8	0.3	66.0	54.5	0.1	6.6	48.5	0.3

Table A8: trace element abundances for groundmass minerals in MET11640/2-3-4/TEP. Ol = olivine, Px = pyroxene, Msk = maskelynite, Mer = merrillite.

sample	La			Ce			Pr			Nd			Sm		
	ppm	2σ%	LOD	ppm	2σ%	LOD	ppm	2σ%	LOD	ppm	2σ%	LOD	ppm	2σ%	LOD
234-1-1			0.39			0.75	0.18	12.37	0.07	0.77	11.59	0.38	0.56	17.86	0.05
234-1-2			0.47			0.77	0.11	11.82	0.07	0.76	1.19	0.29	0.56	15.36	0.03
234-1-3			0.61			1.00	0.14	17.37	0.09	1.10	1.89	0.40	0.53	17.88	0.11
234-2-1			0.48			0.77	0.19	12.84	0.08	0.81	1.47	0.36	0.61	18.33	0.03
234-2-2			0.50			0.91	0.12	5.53	0.09	0.94	13.83	0.48	0.63	13.60	0.02
234-2-3			0.52			0.80	0.11	14.91	0.09	1.13	1.62	0.44	0.65	16.92	0.07
234-2-4			0.52	0.77	6.39	0.72	0.15	11.76	0.07	1.18	8.47	0.31	0.77	14.29	0.16
234-2-5			0.58			1.08			0.11	0.80	18.75	0.46	0.44	25.00	0.06
234-3-1			0.48			0.82	0.13	22.38	0.08	0.86	13.95	0.46	0.65	21.54	0.06
234-3-2			0.38			0.68	0.16	13.28	0.05	0.77	22.78	0.35	0.74	2.27	0.03
234-4-1			0.39			0.76	0.11	17.70	0.07	0.63	17.46	0.31	0.49	2.16	0.06
234-4-2			0.40			0.66	0.16	15.94	0.08	0.72	11.68	0.24	0.50	2.00	0.04
234-4-3			0.46			0.84			0.10			0.41	0.57	15.78	0.14
234-4-4			0.31			0.69	0.11	19.30	0.09	0.66	11.84	0.36	0.56	13.59	0.10
232-1-1			0.34	0.96	1.32	0.65	0.19	1.82	0.09	1.39	11.52	0.26	0.87	13.79	0.06
232-1-2			0.39			0.73			0.09	0.54	1.87	0.34	0.34	24.12	0.06
232-1-3			0.38			0.61			0.07	0.48	16.74	0.30	0.40	11.11	0.07
232-2-1			0.26			0.52	0.11	19.82	0.06	0.65	16.92	0.24	0.45	16.22	0.04
232-3-1			0.32			0.65	0.11	12.73	0.07	1.60	1.38	0.22	0.56	1.14	0.10
232-3-2			0.24	0.56	1.91	0.43	0.11	10.00	0.04	0.86	15.12	0.19	0.55	9.65	0.06
232-3-3			0.23	0.57	11.53	0.34	0.11	12.50	0.04	0.83	11.35	0.22	0.57	11.86	0.02
232-3-4			0.21	0.50	6.20	0.45	0.11	12.61	0.03	0.73	1.41	0.16	0.49	12.75	0.05
232-4-1			0.35			0.55			0.08	0.60	2.00	0.28	0.43	15.22	0.08
232-4-2			0.47			0.87			0.11	0.52	21.15	0.38	0.43	21.18	0.09
232-4-3			0.25	0.52	9.32	0.47	0.15	13.33	0.07	0.62	14.45	0.34	0.57	15.78	0.17
221-1-1			0.30	0.54	1.29	0.49	0.12	13.68	0.06	0.77	9.34	0.22	0.50	16.94	0.07
221-1-2			0.31	0.66	6.79	0.58	0.14	6.96	0.09	0.99	11.11	0.36	0.66	12.12	0.12
221-1-3	0.16	14.29	0.01	0.52	7.32	0.01	0.14	9.38	0.01	0.77	12.92	0.01	0.43	15.43	0.01
221-1-4			0.33			0.64	0.13	15.53	0.05	0.76	13.16	0.27	0.42	21.46	0.05
221-1-5			0.26	0.54	8.89	0.49	0.17	11.21	0.04	0.77	11.69	0.21	0.44	16.93	0.01
221-2-1			0.24	0.53	9.28	0.42	0.11	11.67	0.03	0.73	1.48	0.21	0.59	18.87	0.02
221-3-1			0.29	0.62	1.86	0.54	0.11	17.12	0.05	0.81	16.49	0.23	0.54	18.52	0.02
221-3-2			0.47			0.66			0.08	0.68	9.28	0.25	0.48	2.83	0.07
221-3-3			0.28	0.53	11.34	0.50	0.15	14.29	0.05	0.83	11.28	0.21	0.44	13.93	0.02
221-3-4			0.29	0.62	7.38	0.58	0.12	8.65	0.07	0.96	9.82	0.23	0.55	9.65	0.03
221-4-1			0.35			0.64	0.12	15.72	0.05	0.83	14.46	0.29	0.52	15.46	0.04
221-4-2			0.33			0.60			0.08	0.62	16.71	0.24	0.42	18.42	0.07

	Eu			Gd			Tb			Dy			Ho		
	ppm	2σ%	LOD	ppm	2σ%	LOD	ppm	2σ%	LOD	ppm	2σ%	LOD	ppm	2σ%	LOD
234-1-1	0.21	11.43	0.02	1.24	11.29	0.05	0.23	9.29	0.02	1.87	8.21	0.08	0.37	8.17	0.01
234-1-2	0.20	9.50	0.04	1.20	1.00	0.05	0.25	1.89	0.02	1.83	7.65	0.13	0.36	5.52	0.01
234-1-3	0.30	15.72	0.06	1.34	11.19	0.08	0.28	9.19	0.02	2.70	8.70	0.17	0.43	8.29	0.02
234-2-1	0.33	15.18	0.02	1.25	1.40	0.10	0.24	9.36	0.01	2.10	7.96	0.14	0.49	9.30	0.02
234-2-2	0.32	7.14	0.04	1.28	11.72	0.16	0.27	1.26	0.01	2.14	7.93	0.09	0.48	5.99	0.01
234-2-3	0.34	12.29	0.06	1.41	7.81	0.14	0.26	11.72	0.01	1.93	7.25	0.08	0.42	6.96	0.02
234-2-4	0.37	4.58	0.03	1.35	9.63	0.07	0.29	9.52	0.01	2.25	6.22	0.09	0.51	6.19	0.02
234-2-5	0.36	17.83	0.08	1.80	12.37	0.14	0.23	8.58	0.01	1.65	13.33	0.18	0.40	2.45	0.05
234-3-1	0.36	9.39	0.04	1.39	12.95	0.07	0.27	17.71	0.01	1.87	11.76	0.09	0.40	9.50	0.02
234-3-2	0.39	13.74	0.03	1.16	7.47	0.10	0.22	12.87	0.01	1.88	14.36	0.05	0.38	11.72	0.01
234-4-1	0.24	14.17	0.04	0.92	15.22	0.04	0.18	1.86	0.01	1.39	1.72	0.08	0.28	1.72	0.02
234-4-2	0.23	7.93	0.03	1.00	1.00	0.10	0.21	11.44	0.004	1.42	6.48	0.05	0.31	9.87	0.01

	Eu			Gd			Tb			Dy			Ho		
	ppm	2σ%	LOD	ppm	2σ%	LOD	ppm	2σ%	LOD	ppm	2σ%	LOD	ppm	2σ%	LOD
234-4-3	0.19	16.62	0.07	1.00	15.00	0.18	0.18	13.68	0.02	1.34	6.81	0.18	0.32	8.69	0.03
234-4-4	0.24	11.30	0.03	0.90	11.11	0.08	0.18	14.86	0.02	1.37	11.68	0.13	0.29	8.34	0.02
232-1-1	0.45	9.14	0.05	1.85	8.65	0.04	0.35	6.82	0.02	2.48	7.26	0.15	0.54	6.26	0.03
232-1-2	0.20	15.75	0.05	0.78	11.18	0.12	0.15	16.45	0.03	1.24	8.88	0.15	0.25	7.87	0.02
232-1-3	0.12	12.69	0.03	0.83	9.99	0.06	0.16	1.76	0.01	1.20	7.17	0.11	0.26	6.44	0.01
232-2-1	0.22	11.47	0.03	0.99	1.11	0.08	0.18	7.69	0.01	1.42	11.27	0.11	0.39	9.61	0.02
232-3-1	0.23	12.33	0.04	1.23	1.57	0.06	0.23	1.53	0.01	1.63	4.91	0.07	0.38	8.47	0.01
232-3-2	0.23	1.34	0.01	1.11	8.83	0.09	0.23	7.39	0.004	1.56	8.33	0.04	0.34	11.79	0.01
232-3-3	0.24	17.28	0.05	1.12	13.39	0.09	0.21	1.43	0.01	1.60	9.38	0.14	0.35	8.00	0.03
232-3-4	0.24	1.84	0.04	0.96	1.24	0.09	0.25	6.83	0.01	1.48	4.12	0.09	0.28	6.76	0.01
232-4-1	0.19	1.53	0.04	0.83	13.25	0.08	0.16	11.54	0.01	1.29	7.75	0.09	0.28	7.42	0.02
232-4-2	0.16	19.24	0.08	0.85	14.12	0.05	0.20	1.77	0.01	1.49	11.49	0.17	0.33	9.76	0.02
232-4-3	0.24	16.18	0.06	0.87	1.56	0.16	0.22	14.75	0.04	1.48	1.14	0.37	0.34	1.42	0.07
221-1-1	0.26	1.55	0.02	1.00	5.43	0.05	0.19	7.25	0.01	1.37	6.95	0.05	0.31	7.69	0.02
221-1-2	0.26	1.35	0.05	1.16	7.73	0.08	0.22	7.27	0.01	1.63	8.59	0.06	0.36	7.46	0.01
221-1-3	0.24	8.44	0.01	0.94	1.64	0.01	0.18	8.24	0.002	1.42	6.11	0.01	0.31	7.35	0.01
221-1-4	0.19	1.82	0.02	0.89	12.36	0.08	0.18	13.11	0.01	1.25	7.46	0.08	0.27	8.58	0.01
221-1-5	0.22	8.36	0.03	1.32	9.12	0.07	0.19	9.19	0.01	1.39	7.35	0.05	0.28	6.83	0.01
221-2-1	0.25	9.80	0.02	0.92	11.96	0.03	0.17	9.20	0.01	1.30	8.46	0.05	0.29	9.47	0.01
221-3-1	0.24	14.64	0.02	0.99	14.14	0.02	0.18	9.84	0.01	1.45	13.79	0.04	0.30	14.53	0.01
221-3-2	0.26	11.65	0.03	0.90	13.33	0.08	0.19	8.18	0.02	1.24	8.88	0.05	0.29	9.28	0.02
221-3-3	0.22	8.93	0.03	1.30	1.68	0.03	0.20	8.16	0.01	1.46	7.53	0.03	0.32	7.86	0.004
221-3-4	0.26	9.85	0.04	1.64	8.55	0.05	0.22	9.52	0.01	1.62	6.97	0.05	0.32	6.52	0.01
221-4-1	0.26	14.78	0.04	1.40	13.46	0.09	0.21	11.68	0.01	1.66	7.23	0.06	0.35	8.47	0.01
221-4-2	0.17	11.18	0.03	0.89	9.29	0.07	0.19	11.35	0.01	1.29	7.75	0.08	0.30	6.45	0.02

	Er			Tm			Yb			Lu		
	ppm	2σ%	LOD	ppm	2σ%	LOD	ppm	2σ%	LOD	ppm	2σ%	LOD
234-1-1	1.23	5.52	0.08	0.17	7.47	0.01	1.24	6.69	0.04	0.14	13.43	0.01
234-1-2	1.11	13.51	0.06	0.15	12.67	0.004	1.95	8.95	0.03	0.18	1.67	0.01
234-1-3	1.39	1.79	0.08	0.21	1.80	0.01	1.19	11.76	0.11	0.18	11.50	0.01
234-2-1	1.33	8.28	0.07	0.18	1.80	0.01	1.12	8.93	0.08	0.19	9.63	0.01
234-2-2	1.28	6.94	0.04	0.18	11.67	0.01	1.37	6.88	0.06	0.18	13.19	0.01
234-2-3	1.16	7.86	0.10	0.20	11.68	0.01	1.21	11.57	0.02	0.17	11.49	0.02
234-2-4	1.39	7.28	0.07	0.24	8.82	0.002	1.30	7.18	0.13	0.19	8.52	0.01
234-2-5	1.90	1.92	0.13	0.16	18.47	0.02	1.21	19.83	0.09	0.18	11.11	0.01
234-3-1	1.15	13.43	0.06	0.17	12.43	0.01	1.40	13.46	0.11	0.15	12.67	0.01
234-3-2	1.11	10.00	0.02	0.17	9.70	0.004	1.10	1.89	0.01	0.14	7.75	0.01
234-4-1	0.97	7.67	0.04	0.14	14.42	0.01	0.86	22.93	0.05	0.12	13.81	0.02
234-4-2	0.86	8.73	0.03	0.13	12.50	0.01	0.82	13.41	0.06	0.13	8.33	0.01
234-4-3	0.91	8.55	0.11	0.14	8.76	0.01	0.77	7.24	0.06	0.10	1.00	0.01
234-4-4	0.73	1.78	0.02	0.12	12.65	0.004	0.74	1.82	0.02	0.13	11.24	0.01
232-1-1	1.52	4.15	0.10	0.22	9.46	0.01	1.36	11.76	0.05	0.19	9.79	0.01
232-1-2	0.85	5.47	0.08	0.11	13.64	0.01	0.76	8.86	0.05	0.13	11.20	0.01
232-1-3	0.76	12.53	0.04	0.12	9.48	0.01	0.75	1.12	0.05	0.12	11.11	0.01
232-2-1	0.94	11.72	0.05	0.13	13.85	0.01	0.90	2.00	0.04	0.14	13.48	0.01
232-3-1	1.50	1.48	0.05	0.14	11.86	0.01	0.83	9.66	0.06	0.13	15.79	0.01
232-3-2	1.00	6.60	0.04	0.14	8.63	0.01	0.88	9.79	0.07	0.12	6.78	0.01
232-3-3	0.98	7.55	0.07	0.15	1.88	0.01	0.93	8.86	0.08	0.13	1.69	0.01
232-3-4	0.96	5.48	0.06	0.12	9.42	0.004	0.84	5.46	0.06	0.12	8.94	0.01
232-4-1	0.81	1.49	0.06	0.13	14.29	0.01	0.83	12.48	0.06	0.13	15.20	0.003
232-4-2	1.11	10.00	0.12	0.16	11.46	0.02	1.28	6.32	0.07	0.15	1.82	0.01

	Er			Tm			Yb			Lu		
	ppm	2σ%	LOD	ppm	2σ%	LOD	ppm	2σ%	LOD	ppm	2σ%	LOD
232-4-3	1.20	1.78	0.33	0.14	16.67	0.04	0.99	12.12	0.21	0.15	8.78	0.04
221-1-1	0.85	7.61	0.03	0.14	13.33	0.003	0.77	7.64	0.07	0.11	14.55	0.005
221-1-2	0.99	7.72	0.07	0.14	12.14	0.01	0.87	1.26	0.05	0.14	1.14	0.01
221-1-3	0.86	8.37	0.01	0.12	1.92	0.002	0.78	7.28	0.01	0.12	8.35	0.01
221-1-4	0.69	12.72	0.04	0.12	12.17	0.01	0.76	7.40	0.02	0.18	13.89	0.005
221-1-5	0.99	5.29	0.05	0.11	12.61	0.01	0.86	7.94	0.04	0.18	11.11	0.004
221-2-1	0.84	4.52	0.03	0.13	13.49	0.003	0.79	5.29	0.04	0.11	10.00	0.005
221-3-1	0.92	1.65	0.04	0.12	11.97	0.005	0.77	12.74	0.05	0.18	12.96	0.01
221-3-2	0.77	1.53	0.04	0.15	11.43	0.01	0.77	1.42	0.11	0.13	11.54	0.01
221-3-3	0.86	9.99	0.02	0.12	13.45	0.01	0.79	6.11	0.01	0.13	9.52	0.01
221-3-4	1.00	5.35	0.05	0.13	1.77	0.01	0.89	6.52	0.06	0.12	6.34	0.01
221-4-1	0.97	11.34	0.03	0.13	12.80	0.01	0.95	1.53	0.08	0.13	12.98	0.01
221-4-2	0.79	9.60	0.03	0.13	9.71	0.01	0.78	9.79	0.07	0.11	13.27	0.01

Table A9: trace element concentrations for Tissint shock melt pockets.

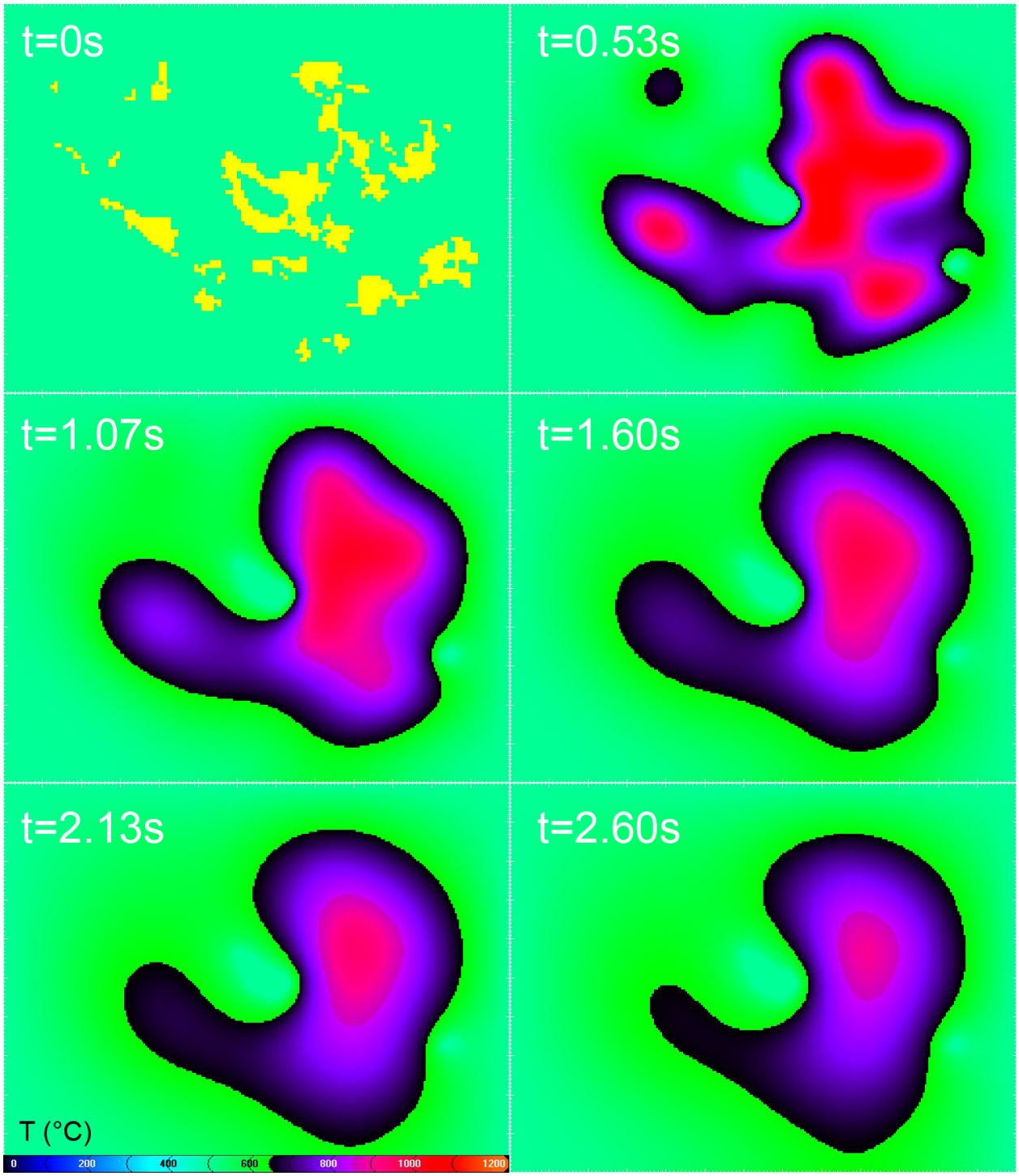

Figure A10: HEAT model results for MET11640/2-2-1/TEP. Small shock melt pockets distal to the large region of melt on the right side of the grid cooled quickly. The large volume of shock melt in this thin section contributed to a longer cooling period relative to the other sections. Heat was lost to vesicles faster than to the host rock by conduction. All shock melt cooled to the solidus within 2.60 s.

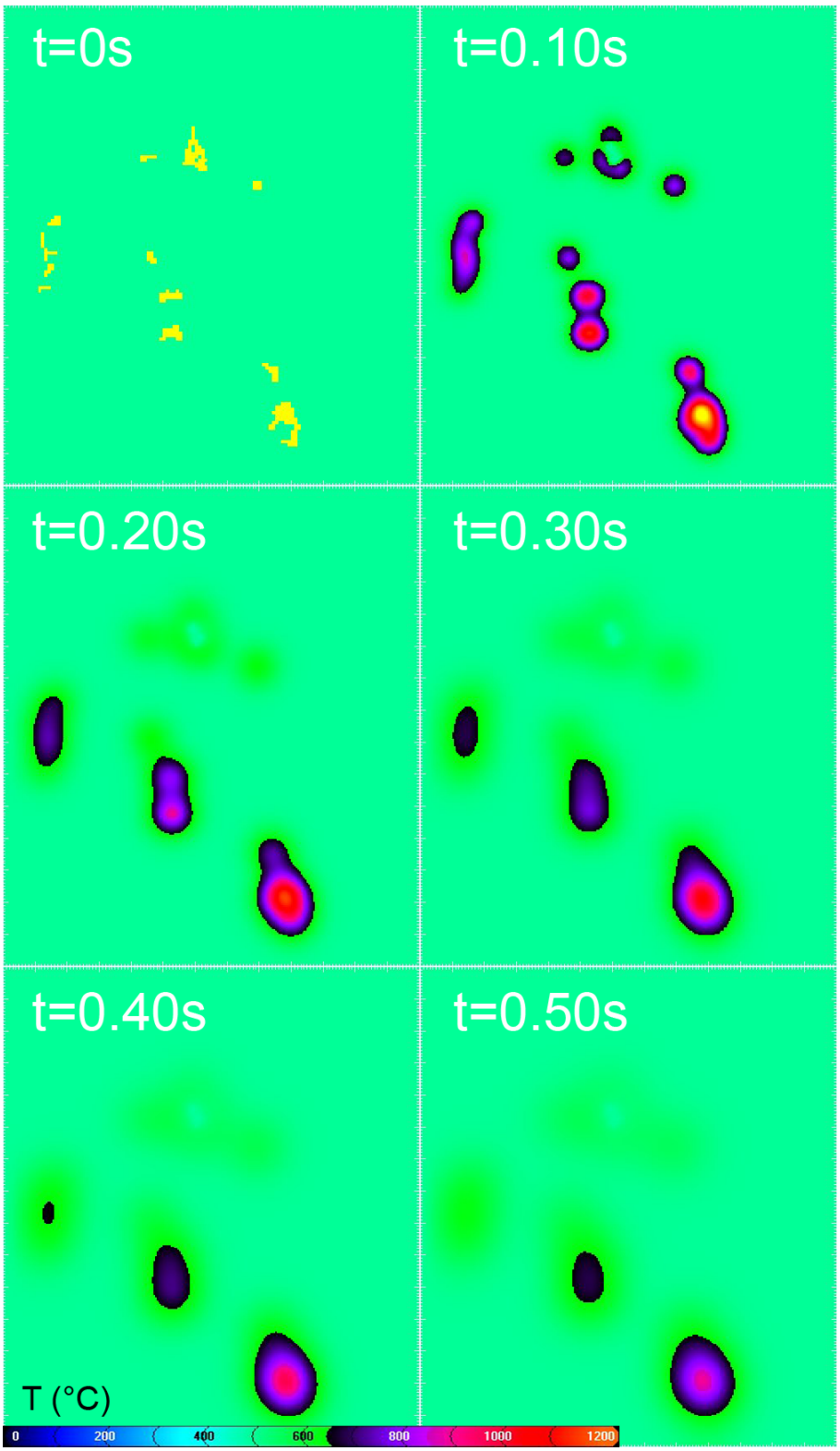

Figure A11: HEAT model results for MET11640/2-3-2/TEP. The vesiculated shock melt pocket in the top center of the grid cools much more quickly than the comparably-sized, vesicle-free shock melt pocket in the bottom right. All shock melt cooled to the solidus within 0.50 s.

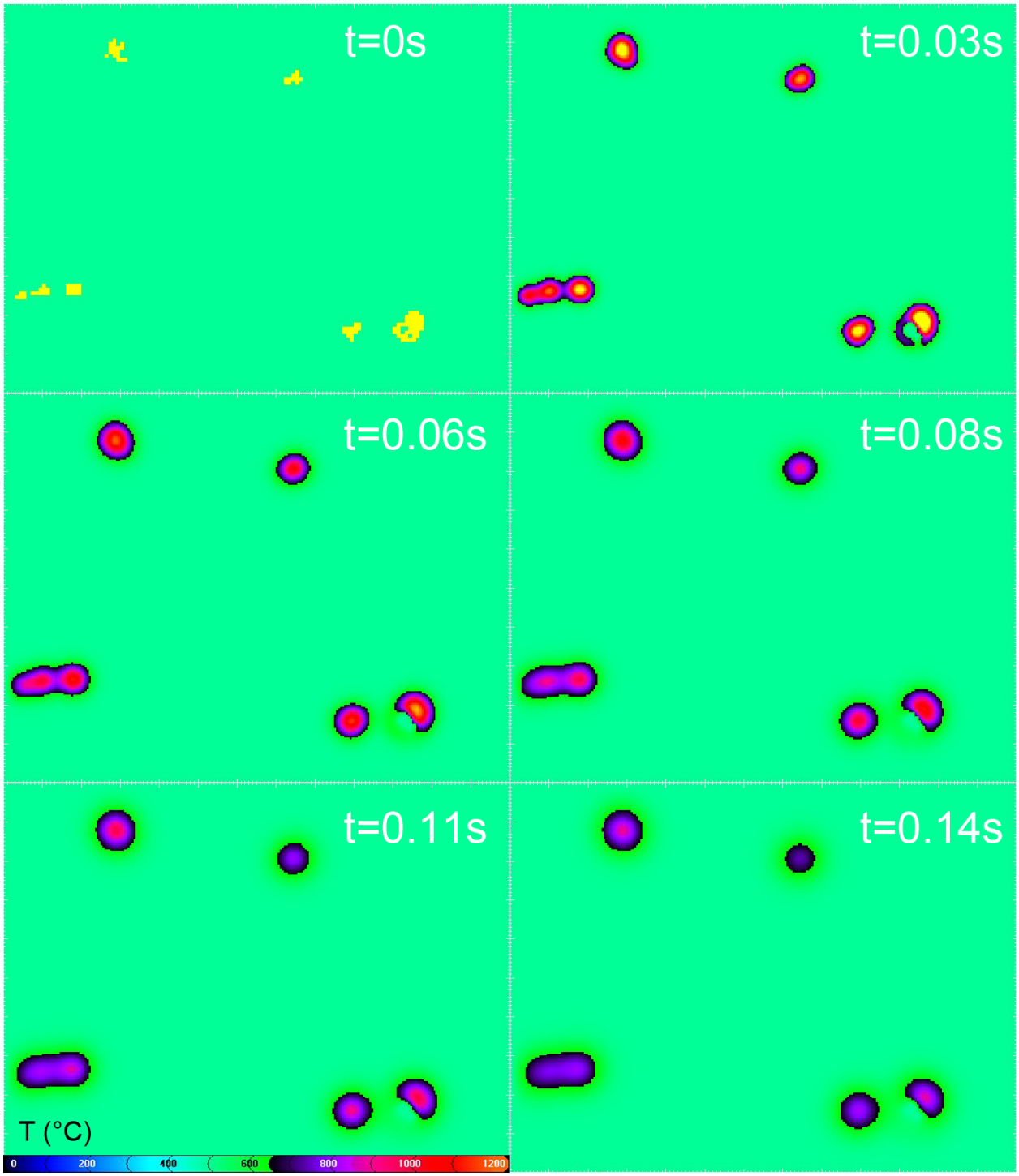

Figure A12: HEAT model results for MET11640/2-3-4/TEP. Small, isolated shock melt pockets cooled quickly, cooling to the solidus within 0.14 s. The shock melt pocket in the bottom right corner of the grid is vesiculated; shock melt adjacent to the vesicle cooled more rapidly than melt distal to the vesicle.